Universitat de Girona

PRODUCTION AND CHARACTERIZATION OF MAGNETIC IRON-BASED MATERIALS BY MECHANICAL ALLOYING, ARC MELTING, AND SPARK PLASMA SINTERING

Kaouther Zaara

Universitat de Girona

DOCTORAL THESIS

PRODUCTION AND CHARACTERIZATION OF MAGNETIC IRON-BASED MATERIALS BY MECHANICAL ALLOYING, ARC MELTING, AND SPARK PLASMA SINTERING

Kaouther Zaara

2023

Universitat de Girona

PRODUCTION AND CHARACTERIZATION OF MAGNETIC IRON-BASED MATERIALS BY MECHANICAL ALLOYING, ARC MELTING, AND SPARK PLASMA SINTERING

DOCTORAL THESIS

Kaouther Zaara

2023

DOCTORAL PROGRAMME IN TECHNOLOGY

Supervised by:

Juan José Suñol Martínez

Mahmoud Chemingui

Presented to obtain the degree of PhD at the University of Girona

Universitat de Girona

Dr Juan-José Suñol Martínezof [Univesitat de Girona]

Dr. Mahmoud Chemingui [Université de Sfax]

WE DECLARE:

That the thesis titles Production and characterization of magnetic iron-based materials by mechanical alloying, arc melting, and spark plasma sintering, presented by Kaouther Zaara to obtain a doctoral degree, has been completed.

This Dissertation is dedicated to

My father, Mohamed

My mother, Zina

My husband, Bader

and

My son, Adam

Acknowledgments

I would first like to thank my supervisor Prof. Joan-Josep Suñol for providing me with the opportunity to carry out this research. Thank you for your advices, recommendations, and continuous encouragement to complete this investigation.

My sincere thanks go to Dr. Mahmoud Chemingui, my co-supervisor at University of Science of Sfax. My dissertation would not have been feasible without your abilities and expertise.

I would like to give a special appreciation to Prof. Virgil Optasanu at ICB, University of Bourgogne, for his help in running experiments, his time and effort is greatly appreciated.

I would also like to thank Prof. Mohamed Khitouni at University of Science of Sfax for his valuable guidance, support and advices.

I am grateful to all of the co-authors of the articles I have previously published or submitted.

Last but not least, I would like to thank my family: my wonderful parents, my brothers and sisters. Thank you for your understanding and encouragement throughout the years. I will never be able to repay all of your sacrifices for me, but I appreciate you from the bottom of my heart. I would not be who I am now without your love and support. Thank you.

List of Publications

The following publications are a result of the work done in this thesis:

- Zaara, K., Chemingui, M., Le Gallet, S., Gaillard, Y., Escoda, L., Saurina, J., ... & Optasanu, V. (2020). High-Entropy FeCoNiB0.5Si0.5 alloy synthesized by mechanical alloying and spark plasma sintering. Crystals, 10(10), 929.

- Zaara, K., Khitouni, M., Escoda, L., Saurina, J., Suñol, J. J., Llorca-Isern, N., & Chemingui, M. (2021). Microstructural and Magnetic Behavior of Nanocrystalline Fe-12Ni-16B-2Si Alloy Synthesis and Characterization. Metals, 11(11), 1679.

- Zaara, K., Daza, J., Ben Mbarek, W., & Suñol, J. J. (2023). Structural, Thermal and Magnetic Analysis of Two Fe-XB (X= Nb NiZr, Nb) Nanocrystalline Alloys. Materials, 16(1), 155.

List of Abbreviations

a	Crystal parameter.
AM	Arc melting.
β	Burger's vector.
B	Magnetic induction
BCC	Body centered cubic.
BPR	Ball to powder ratio.
DSC	Differential scanning calorimetry.
DWs	Domain walls.
EDS	Energy dispersive X-ray spectroscopy.
μ_0	Permeability of free space.
FCC	Face centered cubic.
G	Gibbs free energy.
GOF	Goodness of fit.
H	Enthalpy.
H	Magnetic field strength.
H_c	Coercivity.
HCP	Hexagonal close packed.
HEAs	High entropy alloys.
HV	Vickers hardness.
L	Crystallite size.
M	Magnetization.
m	Mass.
MA	Mechanical Alloying.
M_r	Remanent magnetization.
M_s	Saturation magnetization.
P	Porosity percentage.
PPMS	Physical property measurement system.
R	Gas constant.

R_{exp}	Expected error
ρ	Dislocation densities.
$\rho_{theoretical}$	Theoretical density of the sample.
ρ_{sample}	Density of the sample.
ρ_{water}	Water density.
R_{wp}	Weighted residual error
S	Entropy.
σ	Microstrains.
SEM	Scanning electron microscopy.
SMAs	Shape memory alloys.
SS	Solid solution.
SPS	Spark plasma sintering.
SQUID	Superconducting quantum interference device.
V	Volume.
VSM	Vibrating sample magnetometer.
WSS	Weighted Sum of Square.
XRD	X-ray diffraction.

Table of contents

List of Figures

List of Tables

Abstract

This thesis dissertation discusses the microstructure, thermal behavior, magnetic and mechanical properties of some Fe-based alloys and a high entropy alloy (HEA) in the form of mechanically alloyed powders or bulk solids, taking into account processing conditions. The Fe-based alloys are utilized extensively in sectors such as aircraft production, military, industrial, medical, and manufacturing, while the HEA materials are ideal materials for compressors, combustion chambers, exhaust nozzles, and gas turbine case applications in gas turbine engines. Five alloys were synthesized and their structural, thermal, and magnetic properties were investigated. Mechanical characteristics of bulk alloys have also been examined. Firstly, $Fe_{70}Ni_{12}B_{16}Si_2$, $Fe_{80}(NiZr)_8B_{12}$ and $Fe_{80}Nb_8B_{12}$ were mechanically milled in a planetary ball mill. Microstructural characteristics (cell parameter, crystalline size, and micro deformation index) are obtained from X-ray diffraction patterns at different milling times using the Rietveld method. After milling, thermal and magnetic characterizations are performed to determine crystalline growth, activation energy, saturation magnetization, and coercivity. The annealed at 650°C of the $Fe_{70}Ni_{12}B_{16}Si_2$ final powder improves the magnetic properties by reducing the coercivity to 70 Oe. In terms of magnetic behavior during milling of the two alloys $Fe_{80}(NiZr)_8B_{12}$ and $Fe_{80}Nb_8B_{12}$, all powdered-agglomerated had coercivity values about 10 Oe. Its final milled at 80h products were compacted and thermal and magnetic characterizations were performed.

Second, a high entropy alloy, the $FeCoNiB_{0.5}Si_{0.5}$ was mechanically milled for 150 hours and a single FCC phase was formed. Similar to the preceding alloys, structural, microstructural, thermal, and magnetic studies were carried out. On the one hand, the heat treatment of the resultant powder improves the magnetic properties of milled powders by

increasing saturation magnetization from 94.31 to 127.30 emu/g and lowering coercivity from 49.07 to 29.57 Oe. On the other hand, the resultant powder was consolidated by the spark plasma sintering (SPS) process at two different temperatures in order to produce bulk HEA. The SPS at 750°C improved the coercivity to 25 Oe and had the best mechanical properties (compressive strength of 1062 MPa and Vickers hardness of ~518 HV)

Third, three processes were used to produce $Fe_{65}Ni_{28}Mn_7$ and equiatomic FeCoMn alloy. Initially, the powders were mechanically milled for 130 hours before being studied in the same ways as the preceding alloys. Then, the final powders were compressed by spark plasma sintering to generate bulk samples for mechanical and magnetic studies. Meanwhile, the alloys were manufactured by Arc melting in order to get bulk samples, and their structural, magnetic, and mechanical characteristics were compared to those obtained by SPS. The best magnetic properties were discovered in bulk samples produced following SPS at 1000°C/50MPa for both $Fe_{65}Ni_{28}Mn_7$ and FeCoMn, with coercivity equal to 0.07 Oe and 39 Oe, respectively. The Vickers Hardness was measured in bulk samples of the two alloys at 750°C/50MPa, with values of 425Hv and 647Hv, respectively.

Finally, based on the manufacturing procedure of the powders or bulk samples, all alloys were compared: structurally, magnetically, and mechanically.

Resumen

Esta tesis doctoral analiza la microestructura, el comportamiento térmico y las propiedades magnéticas y mecánicas de algunas aleaciones de base Fe y de una aleación de alta entropía (HEA) en forma de polvo (aleado mecánico) o de sólido, teniendo en cuenta las condiciones de procesado. Las aleaciones a base de Fe se utilizan ampliamente en sectores como la producción aeronáutica, militar, industrial, médica y de fabricación; mientras que los materiales HEA son materiales ideales para compresores, cámaras de combustión, toberas de escape y aplicaciones de cajas de turbinas de gas en motores de turbinas de gas.

Se han producido cinco aleaciones y se han investigado sus propiedades estructurales, térmicas y magnéticas. También se han examinado las propiedades mecánicas de las aleaciones en forma masiva. En primer lugar, $Fe_{70}Ni_{12}B_{16}Si_2$, $Fe_{80}(NiZr)_8B_{12}$ y $Fe_{80}Nb_8B_{12}$ se molieron mecánicamente en un molino de bolas planetario. Las características microestructurales (parámetro de celda, tamaño cristalino e índice de microdeformación) se obtienen analizando difractogramas de rayos X a diferentes tiempos de molienda utilizando el método de Rietveld. Después de la molienda, se ha procedido a la caracterización térmica y magnética para analizar el crecimiento cristalino, la energía de activación, la magnetización de saturación y la coercitividad.

El recocido a 650°C de la aleación (en forma de polvo) $Fe_{70}Ni_{12}B_{16}Si_2$ muestra una mejora de las propiedades magnéticas al reducir la coercitividad a 70 Oe. En cuanto al comportamiento magnético durante la molienda de las dos aleaciones, $Fe_{80}(NiZr)_8B_{12}$ y $Fe_{80}Nb_8B_{12}$, todos los aglomerados presentaron valores de coercitividad del orden de 10 Oe. Sus productos finales molidos durante 80h fueron compactados y se realizó su caracterización térmica y magnética.

En segundo lugar, se molturó mecánicamente una aleación de alta entropía, $FeCoNiB_{0.5}Si_{0.5}$, durante 150 horas, formándose una única fase FCC.

Al igual que en las aleaciones anteriores, se realizaron estudios estructurales, microestructurales, térmicos y magnéticos. Por un lado, el tratamiento térmico (de las aleaciones resultantes en forma de polvo) mejora las propiedades magnéticas aumentando la magnetización de saturación de 94,31 a 127,30 emu/g bajando la coercitividad de 49,07 a 29,57 Oe. Por otro lado, el material resultante se consolidó mediante el proceso de sinterización por chispa de plasma (SPS) a dos temperaturas diferentes para producir HEA masivo. El SPS a 750°C mejoró la coercitividad a 25 Oe y tuvo las mejores propiedades mecánicas (resistencia a la compresión de 1062 MPa y dureza Vickers de ~518 HV).

En tercer lugar, se utilizaron tres procesos para producir $Fe_{65}Ni_{28}Mn_7$ y aleación equiatómica de FeCoMn. Inicialmente, los precursores fueron molidos mecánicamente durante 130 horas antes de ser analizados de la misma manera que las aleaciones anteriores. Luego, los polvos finales se comprimieron mediante sinterización activada mediante plasma para generar muestras masivas para estudios mecánicos y magnéticos. Por otra parte, las aleaciones se fabricaron por fusión en horno arco para obtener muestras masivas y se compararon sus estructuras y sus propiedades magnéticas y mecánicas con las obtenidas mediante SPS. Las mejores propiedades magnéticas se han obtenido en muestras masivas producidas empleando SPS a 1000 °C/50 MPa tanto para $Fe_{65}Ni_{28}Mn_7$ como para FeCoMn, con coercitividades de 0,07 Oe y 39 Oe, respectivamente. La mayor dureza Vickers se midió en muestras masivas de las dos aleaciones a 750°C/50MPa, con valores de 425Hv y 647Hv, respectivamente.

Finalmente, con respecto al procedimiento de fabricación de los polvos o muestras masivas, se ha procedido a la comparación de todas las aleaciones: estructural, magnética y mecánica.

Resum

Aquesta tesi doctoral analitza la microestructura, el comportament tèrmic i les propietats magnètiques i mecàniques d'alguns aliatges de base Fe i d'un aliatge d'alta entropia (HEA) en forma de pols (aliat mecànic) o en forma de sòlid, tenint en compte les condicions de processat. Els aliatges a base de Fe s'utilitzen àmpliament en sectors com la producció aeronàutica, militar, industrial, mèdica i de fabricació; mentre que els materials HEA són materials ideals per a compressors, càmeres de combustió, toveres d'escapament i aplicacions de en motors de turbines de gas.

S'han produït cinc aliatges i se n'han investigat les propietats estructurals, tèrmiques i magnètiques.

També s'han examinat les propietats mecàniques dels aliatges de forma massiva. En primer lloc, els aliatges $Fe_{70}Ni_{12}B_{16}Si_2$, $Fe_{80}(NiZr)_8B_{12}$ i $Fe_{80}Nb_8B_{12}$ es van produir mecànicament en un molí de boles planetari. Les característiques microestructurals (paràmetre de cel·la, mida cristal·lina i índex de microdeformació) s'obtenen analitzant difractogrames de raigs X a diferents temps de mòlta emprant el mètode de Rietveld. Després de la mòlta, s'ha procedit a la caracterització tèrmica i magnètica per analitzar el creixement cristal·lí, l'energia d'activació, la magnetització de saturació i la coercitivitat. El recuit a 650°C de l'aliatge (en forma de pols) $Fe_{70}Ni_{12}B_{16}Si_2$ mostra una millora de les propietats magnètiques en reduir la coercitivitat a 70 Oe. Pel que fa al comportament magnètic durant la mòlta dels dos aliatges, $Fe_{80}(NiZr)_8B_{12}$ i $Fe_{80}Nb_8B_{12}$, tots els aglomerats van presentar valors de coercitivitat de l'ordre de 10 Oe. Els productes finals mòlts durant 80h van ser compactats i se'n va realitzar la caracterització tèrmica i magnètica.

En segon lloc, es va moldre mecànicament un aliatge d'alta entropia, $FeCoNiB_{0.5}Si_{0.5}$, durant 150 hores, formant-se una única fase FCC. Igual que en els aliatges anteriors, es

van realitzar estudis estructurals, microestructurals, tèrmics i magnètics. D'una banda, el tractament tèrmic (dels aliatges resultants en forma de pols) millora la resposta magnètica augmentant la magnetització de saturació de 94,31 a 127,30 emu/g, i baixant la coercitivitat de 49,07 a 29,57 Oe. D'altra banda, el material resultant es va consolidar mitjançant el procés de sinterització per espurna de plasma (SPS) a dues temperatures diferents per produir HEA massiu. L'SPS a 750°C va millorar la coercitivitat a 25 Oe i va tenir les millors propietats mecàniques (resistència a la compressió de 1062 MPa i duresa Vickers de ~518 HV).

En tercer lloc, es van utilitzar tres processos per produir $Fe_{65}Ni_{28}Mn_7$ i l'aliatge equiatòmic FeCoMn. Inicialment, els precursors van ser mòlts mecànicament durant 130 hores abans de ser analitzats seguint el procediment emprat en els aliatges anteriors. Després, les pólvores finals es van consolidar mitjançant sinterització activada mitjançant plasma per generar mostres massives per a estudis mecànics i magnètics. D'altra banda, els aliatges es van fabricar per fusió en forn arc per obtenir mostres massives i se'n van comparar les estructures i les propietats magnètiques i mecàniques amb les obtingudes mitjançant SPS. Les millors propietats magnètiques s'han obtingut en mostres massives produïdes emprant SPS a 1000 °C/50 MPa tant per a $Fe_{65}Ni_{28}Mn_7$ com per a FeCoMn, amb coercitivitats de 0,07 Oe i 39 Oe, respectivament. La major duresa Vickers es va mesurar en mostres massives dels dos aliatges a 750°C/50MPa, amb valors de 425Hv i 647Hv, respectivament.

Finalment, pel que fa al procediment de fabricació de les pólvores o mostres massives, s'ha procedit a la comparació de tots els aliatges: estructural, magnètica i mecànica.

GENERAL INTRODUCTION

CHAPTER 1

1 Introduction and objectives

Iron, with the symbol Fe, is one of the most frequent chemical elements on Earth, accounting for around 5% of the Earth's crust. Iron has an atomic weight of 55.847 and an atomic number of 26. Iron is a transition metal in Periodic Table Group 8 of the periodic table. Iron is one of the most valuable metals due to its availability, working characteristics, and tenacity. Pure iron has a silvery white, glossy surface. Because of its malleability and ductility, it can be readily molded into various shapes without breaking or fracturing. Iron is also an excellent conductor of heat and electricity, which has a direct impact on the quality of our lives. Iron ore was one of the earliest ores that people used to make tools, and it has played an important part in human history. Iron melts at 1538 °C and boils at 3070 °C [1]. Iron has a density of 7.874 g/cm^3 with Young's and shear moduli at room temperature of 200 GPa and 78 GPa, respectively. While pure Fe is somewhat soft, alloying it with a certain percentage of other elements may greatly harden and strengthen it. Steels and iron-based alloys account for about 95% of all metal alloys produced. Such a large manufacturing and widespread use is made possible not only by the availability and ease of extraction of iron-bearing rocks, but also by low-cost processing and the wide variety of useful qualities that it may provide. In engineering, Fe-based materials are commonly employed. Steel is, in reality, the most significant engineering material in the world. Fe-based superalloy materials, such as Fe-Ni, were developed to provide materials with higher tensile ductility, shorter creep extension, greater crack propagation resistance, and high-temperature uses [2]. Shape memory alloys (SMAs) based on Fe are attractive candidates for use as prestressing tendons in civil engineering projects [3]. The major source of permanent magnets is barium and strontium ferrite magnets with high coercivity, which are frequently utilized in magnetic recording medium [4]. Aside from these traditional uses, Fe has begun to be used in several unique ones, such as superconductors, biodegradable materials, bulk amorphous soft magnetic materials, and catalysts. It is the goal of this thesis to investigate novel Fe-based materials produced through various processes. And to investigate the materials structure, microstructure, thermal, magnetic, and mechanical properties.

1.1 Magnetic Materials

A magnetic material is a substance that reacts to a magnetic field. The magnetic field causes the push and pull on other ferromagnetic materials. When subjected to an external magnetic field, materials react differently. The basic parameters from a classical approach are magnetic field strength (H), magnetization (M), and magnetic induction (or magnetic flux density, B), where magnetization is a measure of material reaction to applied field and magnetic induction is net magnetic flux density inside the material. The following equations describe the relationships between these parameters:

$$M = \chi H \tag{1.1}$$

$$B = \mu_0 M + H \text{ ; or } B = M + 4\pi H \tag{1.2}$$

Where χ is the susceptibility and μ_0 is the permeability of free space.

Magnetic Materials are classed as diamagnetic, paramagnetic, ferromagnetic, antiferromagnetic, or ferrimagnetic based on their response (susceptibility: χ) to an applied magnetic field. Our specific interest here is in ferromagnetic materials, such as iron, nickel, cobalt, and their alloys. Even without any applied field, the magnetic moments in ferromagnetic materials spontaneously align in a regular manner, resulting in significant net magnetization. Hysteresis is a property of ferromagnetic materials, which can be scientifically represented by a hysteresis loop plotting magnetization M (or magnetic induction B) against applied field H. Figure 1.1 represents a typical ferromagnetic hysteresis loop. The ferromagnet is initially not magnetized, but when the field H is applied, magnetic induction increases in the field direction. If H is increased continuously, the magnetization will reach saturation at a value known as M_s. When the external field is decreased to zero, the remaining magnetic induction is known as remanent magnetization M_r. Magnetic induction can be decreased to zero by applying a reversing magnetic field of strength H_c, which is defined as coercivity. Magnetic domains and domain walls (DWs) are two additional important concepts for understanding the behavior of magnetic materials. A magnetic domain is an area of homogeneous magnetism within a material. DWs are zones that separate magnetic domains in which the direction of magnetization rotates, generally coherently, from one domain to the neighboring domain [5]

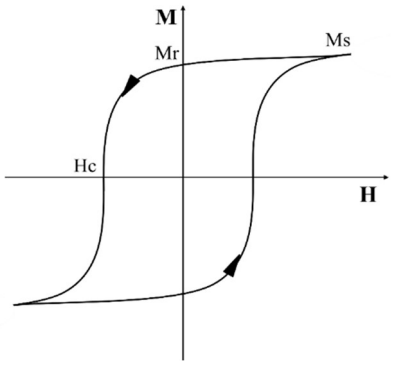

Figure 1.1: Typical hysteresis loop of a ferromagnetic material.

The shape of a hysteresis loop reflects the characteristics of a ferromagnet. The area inside the hysteresis is proportional to the energy required to spin the magnetic moments. Ferromagnets can be classified as soft, hard, or semi-hard magnetic materials based on the strength of the coercive field (Figure 1.2). Soft magnetic materials can be magnetized by a low external magnetic field, and when the field is removed, the material reverts to its low residual magnetism state. The coercivity of soft magnetic materials is less than 1000 A/m (12.56 Oe) [6]. They are typically utilized in alternating current applications, such as transformer magnetic cores, motors, and inductors, where minimal hysteresis loss is favored and necessary to limit energy dissipation. Hard-magnetic materials, on the other hand, maintain a large amount of residual magnetization and coercivity ranging from 10 kA/m (125 Oe) to 1000 kA/m (12 kOe) [6]. Semi-hard magnetic materials, which fall in between the first and second materials, have a relatively strong coercive field and residual magnetization [6]. As a result, they are most commonly used in magnetic recording (Figure 1.2). Depending on its physical condition, the same material/alloy can be magnetically soft or hard [7].

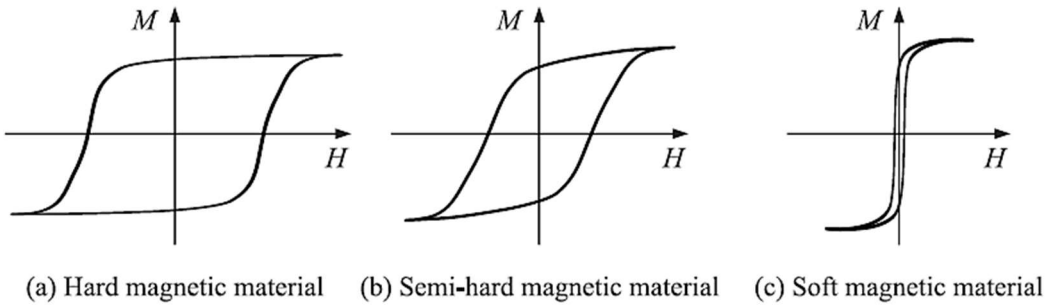

Figure 1.2: Major hysteresis loops of Soft, semi-hard and hard magnetic materials.

1.1.1 Soft Magnetic Materials

Soft magnetic materials have high permeability, low coercivity, low hysteresis loss and have been applied to amplify the flux density created by a magnetic field. The characteristics improve over time, i.e., coercivity decreases, permeability increases, and hysteresis losses decrease. All of this is done by lowering anisotropy and domain in wall pinning. Soft magnetic materials include FeSi alloys, NiFe alloys, and ferrites. Soft magnetic materials are mostly useful in transformers, inductors, and magnetic sensors.

1.1.2 Hard Magnetic Materials

These materials are exceptionally resistant to demagnetizing fields. This category includes materials with coercivity more than 10 kA/m (125 Oe). Because of its great magneto-crystalline anisotropy, the material retains its magnetic characteristics when exposed to an external magnetic field. To make hard magnetic materials, ferromagnetic metals such as Fe and Co are alloyed with high anisotropic materials to enhance coercivity [8]. Current research efforts are aimed at increasing the magnetic characteristics of materials such as cobalt rare earth alloys ($SmCo_5$ and/or Sm_2Co_{17}) and neodymium-iron-boron ($Nd_2Fe_{14}B$), iron platinum, and hard ferrites ($SrO\text{-}Fe_2O_3$ or $BaO\text{-}_6Fe_2O_3$). Hard magnetic materials are commonly used in electric motors, generators, loudspeakers, frictionless bearings, magnetic levitation devices, and other holding magnets such as door locks.

1.1.3 Semi Hard Materials

Semi-hard materials have a coercive field between 1000 A/m (12.56 Oe) and 10000 A/m (125 Oe). Their primary advantage is that they can be easily magnetized and demagnetized while retaining high remanence. They were previously used in hysteresis motors and are now mostly used in magnetic recording. They are usually iron and cobalt alloys [6].

1.2 High Entropy Alloys

1.2.1 History of High Entropy Alloys

Material alloying has been an important concept for practical applications since the Stone Age. Bronze, steel, and copper alloys were among the first metallic alloys produced. Many of these early alloys followed the conventional alloying process of employing a single principal component and then adding minor amounts of different additional components to improve the alloy. Materials research had typically been centered on

enhancing the properties of conventional alloys until a novel approach arose in 2004. In this year, two papers on multicomponent were released for the first time. The $CuCoNiCrAl_xFe$ system was investigated by the Yeh et al. group, who discovered that the alloys showed a simple structure rather than the complex one that was predicted, containing intermediate and intermetallic phases [9]. An equiatomic FeCrMnNiCo alloy that produced a single FCC solid solution was also investigated by the Cantor et al. group [10]. It was thought that the high entropy gained from the equiatomic quantities of each element contributed to the formation of such simple solid solution structures. Due to this, high entropy alloys (HEAs), as they are now popularly known, were born. The Yeh group and the Cantor group started study on this subject several years before, despite the fact that many in the HEA community consider 2004 to be the start of this alloy research [11]. Yeh started working with multicomponent alloys in the 1990s because he thought the components' high mixing entropy would result in reduced phases. Yeh and Cantor are both considered as pioneers of high entropy alloys and were the impetus for over two decades of materials research.

1.2.2 Concepts of High Entropy Alloys

As research has progressed, a formal, agreed-upon definition of high entropy alloys has been explored and challenged on a regular basis. Some researchers believe that high entropy alloys are characterized by composition, whilst others believe that entropy is the most important feature. Despite of definition, the primary goal of high entropy alloys is to create single-phase solution alloys instead of intermetallic or intermediate phases. This type of alloy is credited with superior properties over conventional alloys.

There are different basic definitions of high entropy alloys that have been accepted and three of them are going to be discussed below.

- The work developed by Yeh et al. allowed the possibility of expanding the category of alloys for the composition-based definition by recognizing that these alloys may contain principal elements with compositions ranging from 5 to 35% atomic percent [9]. The definition based simply on composition excludes entropy and places no restrictions on the creation of solid solutions. As a result, this composition-based definition opens up a wide range of alloy compositions.
- The degree of an alloy's entropy can be used to classify high entropy alloys. Entropy is based on a thermodynamic system that seeks equilibrium by decreasing the system's Gibbs free energy value [12] following the equation:

$$G = H - TS \quad (1.3)$$

The prediction of an alloy's lowest energy state may be compared with the free energy of mixing (ΔG_{mix}) of several states to determine which has the lowest ΔG_{mix}. The variations in free energy of mixing can be determined by

$$\Delta G_{mix} = \Delta H_{mix} - T\Delta S_{mix} \quad (1.4)$$

where ΔH_{mix} is the mixing enthalpy and ΔS_{mix} is the mixing entropy [12]. The configurational entropy of mixing for an n-element equimolar alloy is determined using the Boltzmann hypothesis as follows:

$$\Delta S_{mix} = R\ln(n) \quad (1.5)$$

Where R is the gas constant (8.314 J/mol K) [9]. Figure 1.3 shows the entropy of mixing determined using Equation 1.5 based on the number of equimolar components in an alloy. The graphic shows that increasing the number of elements raises the entropy of mixing for a system, which is expected to lead to the creation of the solid solution phase. A number of five elements is chosen as the lower boundaries because it is thought to be the point at which the entropy of mixing would counterbalance the enthalpy of mixing, hence decreasing the value of the free energy of mixing [12].

Alloys can be grouped based on the magnitude of entropy from the number of elements used for equimolar alloys using the principle of measuring the entropy of mixing. Following the criteria, multiprincipal element alloys may be classed as bellow:

Low Entropy Alloys: $\Delta S_{conf} \leq 0.69R$

Medium Entropy Alloys: $0.69R \leq \Delta S_{conf} \leq 1.61R$

High Entropy Alloys: $\Delta S_{conf} \geq 1.61R$

The configurational entropy per mole (ΔS_{conf}) during the formation of a solid solution from n elements with equimolar fractions may be estimated using Boltzmann's hypothesis on the relationship between entropy and system complexity [13.].

$$\Delta S_{conf} = -k \ln w = -R\left(\frac{1}{n}\ln\frac{1}{n} + \frac{1}{n}\ln\frac{1}{n} + \cdots + \frac{1}{n}\ln\frac{1}{n}\right) = -R\ln\frac{1}{n} = R\ln n \quad (1.6)$$

Where k is Boltzmann's constant, w is the number of ways of mixing and R is the gas constant: 8.314 J/mol.K

Alloys, whether equiatomic or not, are commonly classified as "high entropy" if they consist of five or more principal elements, "medium entropy" when they contain three or four principal elements, and "low entropy" when they contain just one or two principal elements. The majority of commercial alloys have a low entropy, with some ranging into the medium range and none above 1.5R. This suggests that HEAs may have a better ability to induce solid solution formation, resulting in improved material properties [14].

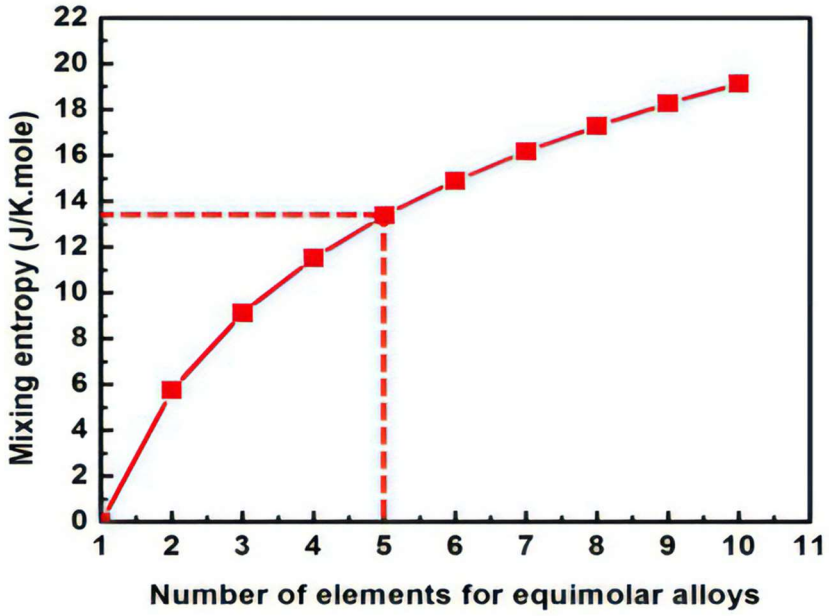

Figure 1.3: The entropy of mixing in an equimolar alloy depends on the number of elements.

- Because there are various alloy combinations that can exist according to both the composition and entropy-based concepts, some researchers have merged the two definitions to reduce the scope of alloys that can be categorized as high entropy alloys. There have also been interpretations that a HEA must be a single-phase solid solution, which has been a primary motivation for HEAs since they are favorable over the formation of intermetallic phases.

1.2.3 Properties

The large number of composites to be characterized is further increased by the wide range of compositions. Establishing links between compositions, microstructure, and characteristics presents new challenges. Even within the same family, a little change in one element might result in a significant change in microstructure and characteristics. The microstructure of the alloy is influenced by the manufacturing procedure and post-process

thermos-mechanical treatment. Even defects like cast segregation, dendritic microstructures, and residual stresses might have an impact on the results [15].

Thermal properties

An example of the thermal analysis was done in the characterization of the $Al_xCoCrFeNi$ ($0<x<2$) [16] system. The alloys were annealed at 1273 K and subsequently water quenched. Temperature has an opposite effect on pure metals, yet it is similar to stainless steel and superalloys. Thermal conductivity falls inside the single-phase area as Al concentration increases. This is explained by the fact that single phase BCC alloys (with a high Al concentration) have nearly double the heat conductivity of single-phase FCC alloys (low Al content). These phenomena are investigated utilizing lattice distortions and an enhanced phonon mean free path caused by lattice thermal expansion at high temperatures.

Magnetic properties

The majority of the alloys examined for magnetic properties comprise Fe, Co, and Ni. FeCoNi is a ferromagnetic solid solution (SS) alloy with an FCC crystal structure and 151 Am^2/kg saturation magnetization [17]. The M_S for pure Fe is 218 Am^2/kg, while the M_S for Ni is 55 Am^2/kg. The FCC structure is transformed to FCC + BCC/B2 by the introduction of Al in $Al_xFeCoNi$. With the addition of Al, the alloy remains ferromagnetic, but the Ms reduces to 102 Am^2/kg. The addition of Al and Si to $(AlSi)_XFeCoNi$ ($0<x<0.8$) [18.] provides great M_S, coercivity, electrical resistivity, strain, and yield strength without fracture at x=0.2. All this making the alloy an interesting soft magnetic material. HEAs have recently been revealed to have excellent magnetic properties. They are an excellent choice for soft magnetic materials that require high saturation magnetization, electrical resistivity, malleability, and low coercivity. A variety of ferromagnetic materials are used to make HEAs, and topological disorientation and chemical variability can enhance electrical resistance. Moreover, these HEAs have a simple crystalline structure, which aids in malleability. Nevertheless, only few HEAs can fulfill all of the above criteria. Consider $FeCoNi(AlSi)_X$ ($0<x<0.8$): when the value of x increases, the magnetization reduces, the resistivity rises, and the coercivity increases and eventually declines, as illustrated in Figure 1.4. As a result, we must determine an optimum value of x for which the three features are satisfactory [18].

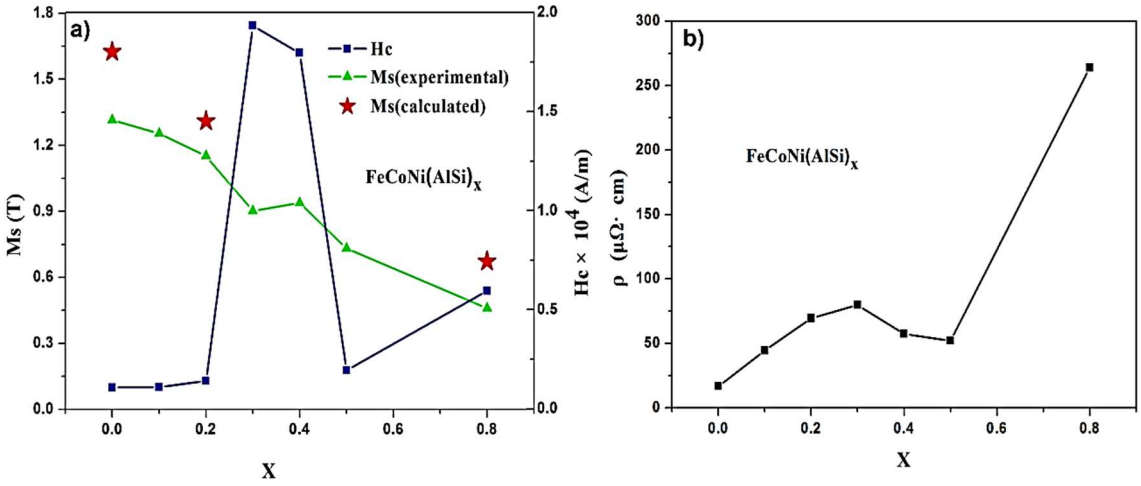

Figure 1.4: Magnetic properties of $FeCoNi(AlSi)_x$ ($0<x<0.8$) alloys (H_c and M_s represent the coercivity and saturation) (b) The electrical resistivity (r) of $FeCoNi(AlSi)_x$ alloys obtained at room temperature [18].

Mechanical properties

-HEAs have a stable microstructure and unusual mechanical properties due to the compositional characteristics of multi-principal elements, including high strength and hardness [19-21], high wear resistance [20-23], exceptional low-temperature ductility [24], good corrosion [19, 25], and high-temperature oxidation resistance [26,27]. This shows that HEAs might be used as advanced engineering materials. Tensile yield strength and elongation are the most typical mechanical characteristics for engineering materials.The majority of HEAs with high yield strength have low ductility and vice versa. For example, an ultrahigh yield strength of over 1.8 GPa associated to a low ductility of less than 10% for the $Al_{0.6}Cr_{0.9}FeNi_{2.6}V_{0.2}$ alloy [28], whereas ductile HEAs (such as CoCrFeMnNi, FeCoNiCr, and $Al_{0.3}Cu_{0.5}FeCrNi_2$) have a very low strength of less than 300 MPa [29-31]. Other HEAs display balanced strength and ductility, such as $(FeCoNi)_{86}Ti_7Al_7$, $(FeCoNi)_{86}Ti_6Al_8$, and $(TiZrHfNb)_{98}O_2$ [32,33]. These alloys have a high strength of 1 GPa and a ductility of 25% to 50%. However, they are still lower than other classic alloys with ultra-high strength, such as maraging steels, deforming & partitioning (DP) steels, or quenching & partitioning (QP) steels [34-36]. For example, the cost-effective DP steel ($FeMn_{9.95}C_{0.44}Al_{1.87}V_{0.67}$) developed by M.X. Huang and coworkers demonstrated a superior combination of strength and ductility, with yield strength, ultimate tensile strength, and total elongation of 1978 MPa, 2144 MPa, and 22.0%, respectively [35].

-The AlCoCrCuFeNi system is one of the most extensively researched HEAs. Early investigations demonstrated the influence of modifying aluminum concentration on strength for the arc-melted and cast system [16], and changing the aluminum concentration modified the crystal structure of the alloy [37], as well as the strength. An FCC phase is often considered softer and more resistant to change at high temperatures, whereas a BCC phase is harder and more susceptible to high temperatures. Lower Al concentration results in a ductile FCC phase, whereas higher Al content results in an ordered bcc phase. significant additional Al addition enhanced the alloy's strength while decreasing its ductility. The hardness varies between 100 and 600 HV (Check the caption of Figure 1.5).

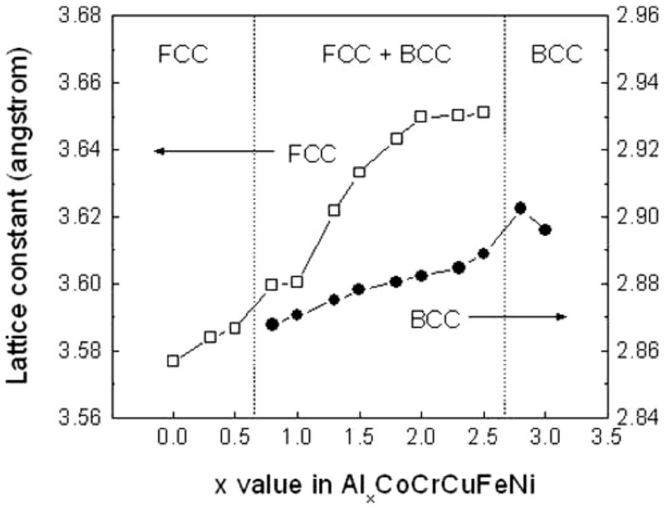

Figure 1.5: Vickers hardness and total crack lengths of the AlxCoCrCuFeNi alloy system with different aluminum contents (x values in molar ratio) [16].

Since HEAs have greater mechanical characteristics at higher temperatures, compressive properties are often examined at both low and high temperatures. According to J.W. Yeh [16], the $Al_{0.5}$CoCrCuFeNi high entropy alloy exhibits distinct behavior at different temperatures and strain rates, as shown in Figure 1.6. A deeper examination reveals specific ups and downs in the plastic deformation areas at 873K, 973K, 1073K, and 1173K. It suggests that several deformation processes occur during compression testing in a high entropy system.

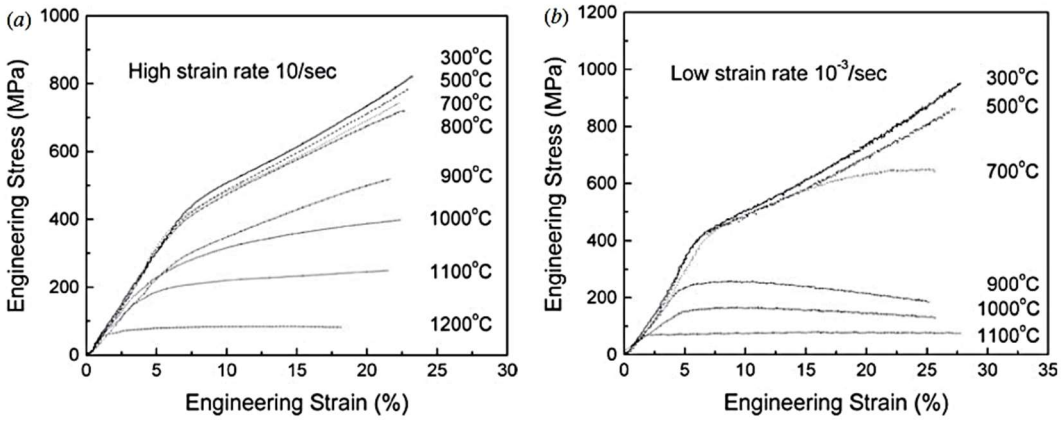

Figure 1.6: Compressive stress-strain curves for $Al_{0.5}CoCrCuFeNi$ at various temperatures and strain rates of (a) 10^{s-1} and (b) 10^{-3} s^{-1} [16].

1.3 Mechanical alloying

1.3.1 Introduction to Mechanical alloying

C. Suryanarayana [38] defined MA as a solid-state powder processing technology that includes repetitive welding, fracturing, and rewelding of powder particles in a high-energy ball mill and material transfer to produce a homogenous alloy. S. Scudino et al. [39] also define MA as the ball milling of powders with various compositions (combination of elemental powders and also intermetallic compounds) in which material transfer and solid state inter diffusion reactions occur. Another definition given by D.L. Zhang [40] is that MA is a technique used for mixing powders or smashing rocks in powder metallurgy and mineral processing. Subsequently, A Calka and A.P Radlinski [41] defined MA as a complicated process of deformation, fragmentation, cold welding, and micro-diffusion that occurs inside a thin layer of powder between two colliding surfaces. The first technological application of mechanical alloying was performed by Benjamin and coworkers of the International Nickel Company, they developed the process to make oxide-dispersion strengthened (ODS) nickel and iron-based superalloys for aerospace applications [42]. Nowadays, the process's popularity has extended across many industries, and the approach has been used commercially and scientifically to generate a wide range of innovative materials. The mechanical alloying procedure is gaining popularity due to the several benefits it provides. These are some examples: Extending the limits of solid solubility; refining grain sizes down to the nanoscale range; disordering of ordered intermetallics; possibility of alloying of difficult-to-alloy

elements; inducing chemical reactions at low temperatures. As a result, MA is a successful processing technology that is now utilized to produce ceramics, polymers, and composite systems in addition to metal alloys. It has received a lot of attention as a potent tool to create a variety of advanced materials (Figure 1.7), such as equilibrium, non-equilibrium, and composite materials.

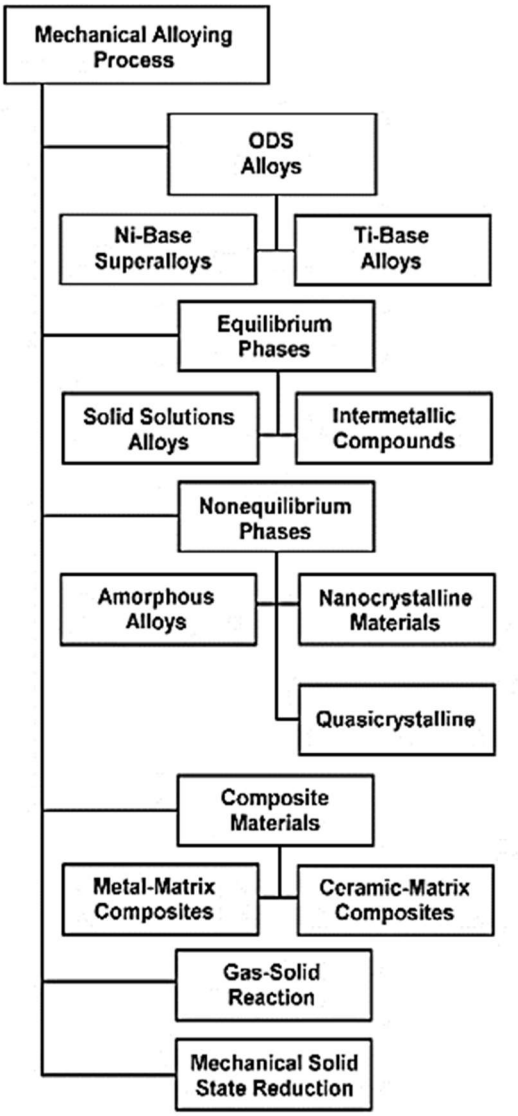

Figure 1.7: Synthesizing capabilities of the Mechanical Alloying process [43].

1.3.2 Process of Mechanical Alloying

Mechanical alloying is dependent on a variety of elements/conditions that require process variable optimization for improved microstructure or to get the desired results. The following process factors mostly influence the quality of powder or end product:

-Type of mill: There are several types of mills available on the market, such as mixer mills, planetary mills, attritors, Uni-ball mills, and so on. These mills differ in capacity, ability to control the process and temperature within jars, etc.,

-Milling container: The material used for the milling container/jars is important due to the impact of the grinding medium on the container's inner walls. If the vessel's nature differs from the powder utilized, some material may be displaced and integrated into the powder. It might contaminate the powder.

-Milling speed/intensity: a high milling speed means a high milling energy, and vice versa. However, milling speed is determined by the mill's design. Balls may be trapped to the inside walls of the vials if they exceed a specific speed (Critical Speed). Higher speed causes a lot of heat inside the jar. It may be advantageous in some situations, such as when diffusion is necessary to induce homogeneity or alloying in powders. However, in other situations, higher temperatures drastically accelerate the process and modify the stages.

-Milling time: It is the most important factor. The time is primarily determined to establish a constant condition between the fracturing and cold welding of the powder particles. It is determined by the mill type, milling intensity, ball to powder ratio (BPR), milling temperature and brittle-ductile behavior of the precursors.

-Grinding medium type, size, and size distribution: The most common abrasive medium materials are hardened steel, hardened Chromium steel, tool steel, WC-Co, and bearing steel. It is important to notice that the balls and containers are made from the same material. The density of the abrasive medium should be high enough so that the impact force of the balls on the powder is sufficient. The size of the grinding medium is also important for milling efficiency. In general, grinding balls with a high density are more beneficial since they can transfer more impact energy to the powder particles.

-BPR (ball-to-powder) weight ratio: It is an important factor in the milling process. Depending on the investigations, it might range from 1:1 to 220:1. Small mills typically utilize a BPR of 10:1, whereas big mills should use a BPR of 50:1 to 100:1. The higher the BPR, the shorter the milling time.

- Energy transfer: It have a significant effect on the constitution of the powder. Since phase transformations in mechanically alloyed powders are caused by energy transferred

from the milling medium to the powder, calculating the energy transferred would be valuable. This, of course, is dependent on the mill type and operating settings. It was discovered that the energy dissipated per hit during milling rises as the rotation speed and the size of the grinding ball increase.

-The extent of filling the vial: Since alloying among powder particles is mostly caused by impact forces, there must be adequate space in the container for the balls and powder particles to move freely. Most milling methods leave 50-60 % of the Vial space unfilled.

-Milling environment: The milling atmosphere has the primary impact of contaminating the powder. As a result, the powders milled in containers that have either been evacuated or filled with an inert gas such as Argon (Ar) or Helium (He). Jars filled with Argon were used in the current investigation to avoid contamination.

All of the above factors are not independent, such as milling speed and milling time, which are determined by the type of mill.

1.3.3 Mechanism of alloying

MA requires filling a vial with the necessary proportions of the blended elemental powders mixing with the grinding medium (generally steel or tungsten carbide balls) and subjecting the powder to severe plastic deformation in a high-energy ball mill. Milling is usually performed in one of four different mill types [38,44,45]. A vibratory mill such as the SPEX shaker mill (Figure 1.8), the vial is shaken several hundred times per minute in a complicated motion that mixes back-and-forth swings with small lateral movements. This machine can make small amounts of powder (approximately 10-20 g) at a time in a short period of time. A vertical ball mill, such as an attritor mill, may be used to produce large amounts of powder (from approximately 0.5 to 40 kg) at a time in a reasonable milling time. The sealed cylindrical tank, as illustrated in Figure 1.8 includes several grinding balls that are activated by a vertical shaft with a set of horizontal impellers attached to it. The impellers energize the ball charge, resulting in a reduction in powder size due to interactions between the balls and the container wall, the agitator shaft, the impellers, and the balls themselves. Another class of mill is the planetary ball mill, which is able to mill a few hundred grams of powder at a time (Figure 1.9). Both the centrifugal force generated by the containers spinning about their axes and the centrifugal force produced by the rotating support disk operate on the milled powder and the grinding balls.

Figure 1.8 shows a traditional horizontal ball mill, which is a reasonably big machine that can be loaded with large volumes of powder and milled over extended periods of time.

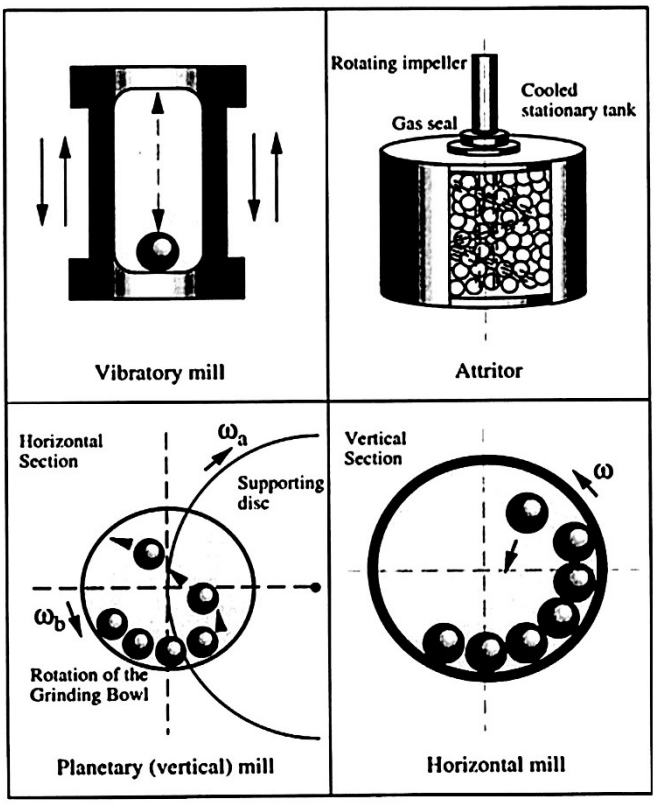

Figure 1.8: Schematic representations of the four different types of milling machines [44].

Figure 1.9 depicts the impact of a single collision on each type of constituent powder particle. The brittle intermetallic and oxide particles are fragmented into smaller particles, while the ductile metal powders are flattened [38].

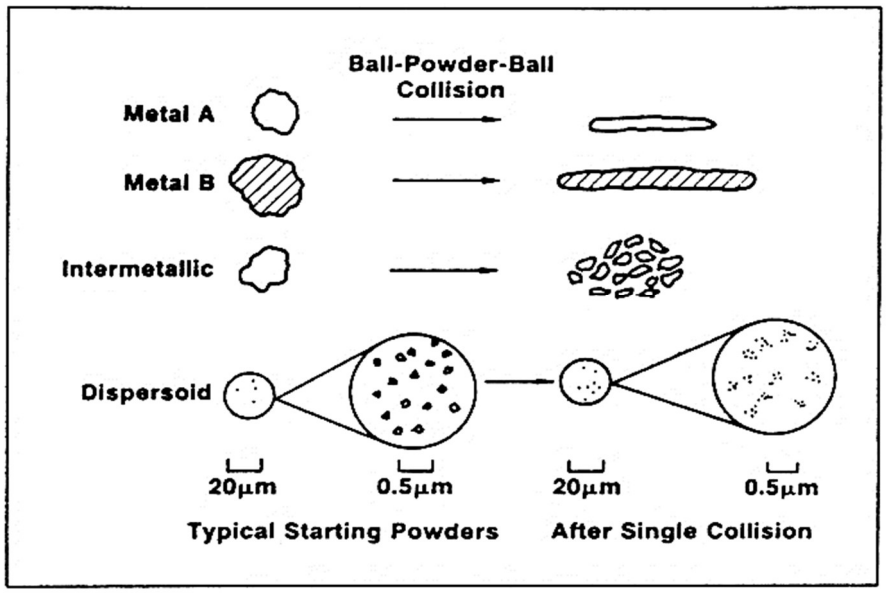

Figure 1.9: Deformation characteristics of representative constituents of starting powders used in mechanical alloying [38].

Alloying is performed by repeatedly welding, fracturing, and re-welding a powder particle mixture in a dry, highly intense ball charge [45]. Regardless of the mill utilized, the process is defined by collisions between the tools and the powders, which result in fragmentation and coalescence. When the grinding balls collide, some powder becomes trapped between them. The force of such a collision causes the powder particles to plastically deform and mix together (Figure 1.10).

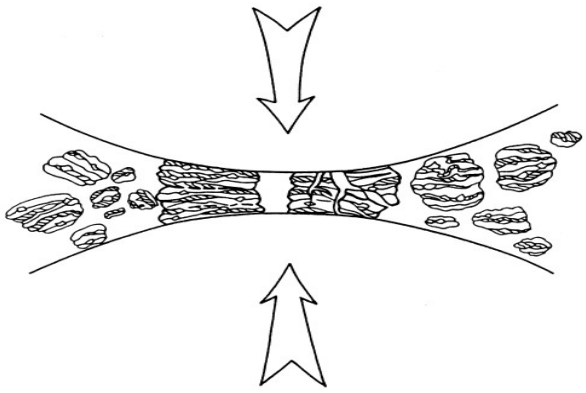

Figure 1.10: Ball-powder-ball collision of powder mixture during mechanical alloying [38]

The impact force deforms the powder particles plastically, causing work hardening and fracture. With continuous deformation, the particles become work hardened and fracture by a fatigue failure mechanism and/or powders/flakes fragmentation. In the absence of strong agglomerating forces, fragments formed by this process may continue to reduce in size. In this case, fracture takes priority over cold welding. The particle structure is constantly modified while the particle size remains constant.

1.4 Spark Plasma Sintering Consolidation

1.4.1 History of SPS

The history of the technology associated with the spark plasma sintering procedure began in late 1930s, when an electrically stimulating sintering method was launched in the United States [46]. The name "spark sintering" originally appeared in a Lenel article in the 1950s [47]. In Japan, a technique known as spark sintering was developed and patented in the 1960s based on the pulse current applied sintering method [48]. However, it was not widely used due to a lack of applications at the time, as well as unresolved issues with industrial production, equipment cost, and sintering efficiency. Sumitomo Coal Mining Co. Ltd. developed the first commercialized SPS (DR. SINTER) in Japan in 1990 [49]. Then, in 2003, FCT (Fine Ceramics Technologies) GmbH & Co in Germany manufactured the first SPS unit in Europe [50]. SPS equipment has recently been produced in the United States [51] and China [52].

1.4.2 Process of the SPS

A schematic representation of the SPS equipment is shown in Figure 1.11. SPS is similar to hot pressing in that powders are inserted into a die (usually graphite) and uniaxial pressure is applied during sintering [53]. Instead of employing an external heating source through normal AC alternating current, a pulsed DC current was transmitted via the sample and the electrically conductive pressure die. As a result, the die works as a heating source, and the sample can be heated from both the inside and the outside. Once activated in this process, diffusion-oriented processes advance very quickly due to effective heat transfer, mechanical stress, and maybe accelerated diffusion rates due to the presence of a DC electric field [54].

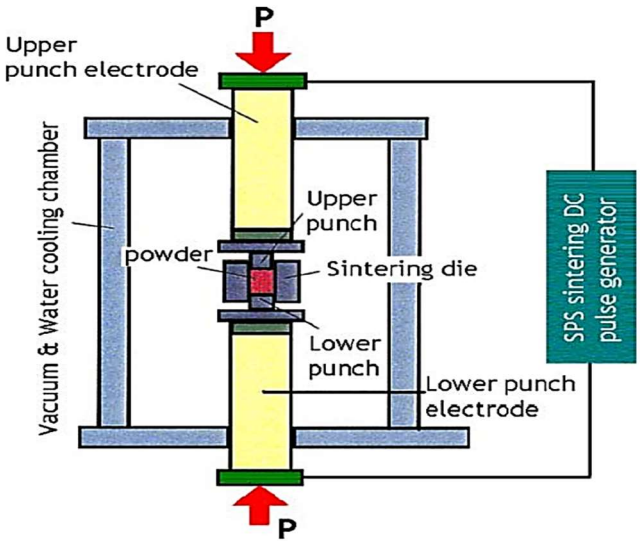

Figure 1.11: Schematic drawing of the applied SPS apparatus [55].

1.4.3 Mechanism of SPS

Many mechanisms have been proposed to account for the improved sintering qualities of the SPS process, including:

(a) Joule heating [56, 57],

(b) Local melting and evaporation, particularly in metallic systems [58],

(c) Particle surface activation [59],

(d) Mechanical activation and plastic deformation,

(E) Field assisted diffusion, [60,61].

(f) Spark impact pressure, [56, 58].

(g) Plasma cleaning of particle surfaces, [57,58]

(h) Plasma sintering,

(i) Electron wind force [62].

(a): As previously noted, the die works as a heating source during SPS processing, and the sample can be heated by DC currents from both the outside and the inside. During the SPS, the Joule heating due to impacts from both external and internal sources can be considerably enhanced. The Joule heating mechanism is a type of resistive heating in which heat is released by passing an electric current through a conductor.

(b+c): At the first stage of sintering, the use of low pressure and high frequency impulsive current was particularly efficient. Due to the high initial contact resistance, it stimulated sparks and rapid local heating at particle contact surfaces. Particularly in metallic systems, it can cause local melting and evaporation as well as particle surface activation.

(d+e): The heated material softens under the uniaxial strain and produces plastic deformation during the SPS. Electric field assisted sintering can improve particle surface, grain boundary, and volume diffusion. The powder compact is densified to over 99% of its theoretical density as a result of plastic deformation and improved diffusion.

(f+g+h): Spark plasma sintered bodies were fully densified during the experiments utilizing a two stages pressure cycle [63]: low pressure to induce interparticle heating (<10MPa) and quite high pressure to improve powder densification.

(i): The mechanism i is far more theoretical in origin. The existence of momentary plasma is the one that causes the greatest debate among these processes. Some scientists [62] provided experimental findings claiming that plasma is not present in SPS processing. Further research into the existence or absence of plasmas during SPS is required.

1.5 Objectives

The main objective is to develop various Fe-based alloys ($Fe_{70}Ni_{12}B_{16}Si_{2,}$ $Fe_{80}X_8B_{12}$(X=Nb,NiZr), $FeCoNiB_{0.5}Si_{0.5}$ (HEA), $Fe_{65}Ni_{28}Mn_7$ and FeCoMn) with superior magnetic and mechanical properties . To achieve this objective, the research work can be divided into two categories. The first, which constitutes the majority of the study, focuses on the production and characterization of Fe-based nanocrystalline magnetic alloys using thermal and magnetic measurements. This first section is concerned with:

1. Influence of milling time on the morphology, phase evolution, microstructural, thermal stability and magnetic properties of Fe-based alloys. To achieve this objective, the five alloys listed above were producing by mechanical alloying (MA) and were analyzed using different characterization techniques.

2. Advanced structural analysis: Rietveld refinements for powder x-ray diffraction data of all alloys produced by MA at various milling times, using MAUD commercial software.

The second goal is to produce solid Fe-based alloys for deep magnetic and mechanical studies. To accomplish the goal of this second section, research is divided into two parts:

1. Investigate the phase transformation, the mechanical properties and magnetic behaviors after consolidation the $FeCoNiB_{0.5}Si_{0.5}$ (HEA) powders using the spark plasma sintering (SPS).
2. Investigate the phase transformation, mechanical characteristics, and magnetic behaviors of $Fe_{65}Ni_{28}Mn_7$ and FeCoMn powders after consolidation by spark plasma sintering. Simultaneously, produce the same alloys using the arc melting (AM) process and compare them to the sintered bulks.

METHODOLOGY

CHAPTER 2

2. Experimental Procedure

This chapter describes the experimental procedures used to synthesize and characterize the $Fe_{70}Ni_{12}B_{16}Si_2$, $Fe_{80}X_8B_{12}$ (X=Nb,NiZr), $Fe_{65}Ni_{28}Mn_7$, $FeNiCoB_{0,5}Si_{0,5}$ and FeCoMn alloys by MA , AM and SPS. A full description of the starting materials, processing of the powders, the as-cast samples and the compacted alloys. The individual powders and massifs samples characterization techniques are also detailed in the sections to follow.

2.1 Production for Synthesis

Table 2.1 provides detailed information on the purity and size of the elemental powders used by Mechanical alloying MA for the different alloy systems. Table 2.2 shows the purity of the massifs, the individual elements of the alloys systems generated by Arc Melting AM. Table 2.3 details the nominal composition of the alloys and their production procedures (MA : Mechanical Alloying, AM: Arc Melting, SPS: Spark Plasma Sintering).

Elements	Powder Purity (%)	Powder Size (µm)
Fe	99.7	30
Ni	99.7	< 30
Co	99.9	< 2-5
B	99.6	10
Si	99.9	< 45
Mn	99.95	<45
Nb	99.85	< 74
NiZr	99.9	> 150

Table 2.1: Elemental powders used in MA (weight %).

Elements	Fe	Ni	Mn	Co
Purity (%)	99.98	99.98	99.98	99.98

Table 2.2: Elemental Materials used in AM (weight %).

Alloys	MA	AM	SPS	compaction
$Fe_{70}Ni_{12}B_{16}Si_2$	X			
$Fe_{80}X_8B_{12}$ (X=Nb,NiZr)	X			X
$FeCoNiB_{0.5}Si_{0.5}$	X		X	
$Fe_{65}Ni_{28}Mn_7$	X	X	X	
FeCoMn	X	X	X	

Table 2.3 Nominal compositions of the alloys and their production procedures.

2.1.1 Mechanical alloying MA

The MA was performed in a high-energy planetary ball mill (Pulverisette P7, Fritsh, Idar-Oberstein, Germany) (Figure 2.1). The experiments were carried out in jars sealed in an Ar-filled glove box to prevent oxidation. The weight ratio of the ball to the powder was 15:1 for $Fe_{70}Ni_{12}B_{16}Si_2$ and $Fe_{80}X_8B_{12}$ (X=Nb,NiZr) and 5:1 for $FeCoNiB_{0.5}Si_{0.5}$, $Fe_{65}Ni_{28}Mn_7$ and FeCoMn. Around 50% of the vial area was left vacant to allow the balls and powder particles to move freely in the milling container. The rotating speed was 600 revolutions per minute. The MA process was monitored by pausing the ball mill at certain stages and collecting a little quantity of powder from each vial inside the glove box for various analysis. The milling technique included 10 minutes of milling followed by 5 minutes of rest. The $Fe_{70}Ni_{12}B_{16}Si_2$ and $FeCoNiB_{0.5}Si_{0.5}$ were milled for 150 h, the $Fe_{80}X_8B_{12}$ (X=Nb,NiZr) for 80 h and the $Fe_{65}Ni_{28}Mn_7$ and the FeCoMn were milled for 130h. It was observed that the powder tended to stick to the container walls, particularly in the early stages of milling, preventing the predicted phases forming. To minimize this impact, the container was opened at regular intervals within the glove box, the powder was scraped from the container's walls, and milling was restarted.

Figure 2.1: Ball milling machine P7.

2.1.2 Arc Melting AM

Arc melting is the most often used process for alloy preparation; it is a simple but effective procedure. The following is a description of the arc-melting technique for synthesizing the $Fe_{65}Ni_{28}Mn_7$ and FeCoMn samples using Buhler MAM-1 compact arc melter (Figure 2.2). The process includes melting the pure elements of the alloys in the required stochiometry by discharging an electrical arc caused by the application of a high tension between two electrodes. The anode, which sits on a steel platform, is a Cu crusible made to hold pure element samples. To avoid heating and melting of the Cu, it is cooled by a water flow. The platform is protected by a stainless-steel hermetic cylinder that contains the cathode in its inner top. The cathode is a sharp rod of W -with 2% Th-, a refractory material that can tolerate high temperature without melting. The cover allows the furnace chamber's environment to be controlled by providing high-purity Ar, which evacuates oxygen and acts as an ionizing gas. The procedure for synthesizing a sample is as follows: after applying tension, the cathode is approached to the pure elements placed on the Cu crusible by twisting a millimetric screw. At a pressure of 1-1.5 bar, argon gas must flow through the furnace chamber. By ionizing the gas when the cathode is close enough, an arc that melts the elements is discharged. After a few seconds of melting, the pure elements are mixed and the tension is removed. The casting is done in such a way that the melt cools quickly, preventing oxidation as much as possible. The ingot was melted five times, to verify that the elements in the alloy remain homogeneous, before being cast into a cold copper mold to produce a master rod with a 20mm diameter.

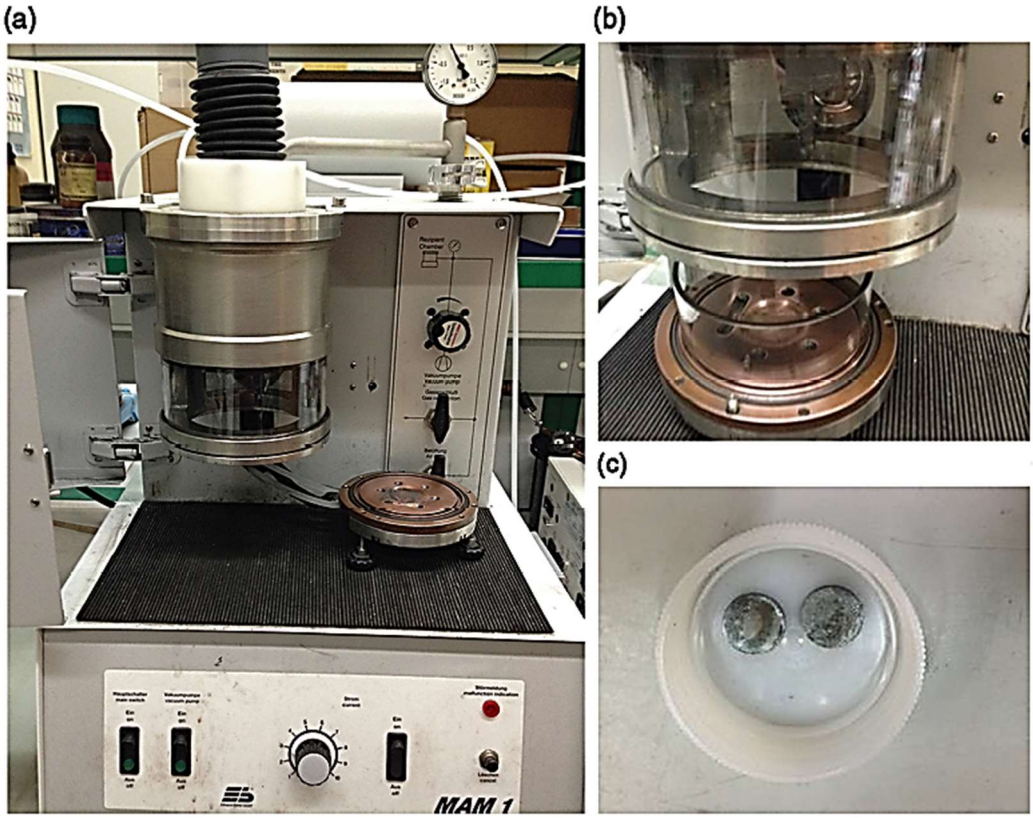

Figure 2.2: Compact arc-melting furnace utilized for synthesis of nanostructured materials (a). Water-cooled copper crucible, where sample can be quenched after melting process (b). Typical aspect of as-grown ingots (c) [64]

2.1.3 Spark Plasma Sintering

All measurements have been carried out by the SPS Thermal Technology HPD10, FCT Systeme (GmbH, Frankenblick, Germany) in the Laboratory ICB (A stay was attended) at the University of Bourgogne- France (as seen in the Figure 2.3).

Figure 2.3: SPS HPD10, FCT System

The powders were compacted into bulk form using the Spark Plasma Sintering (SPS) consolidation process. SPS is often referred to as Field Assisted Sintering Technique or Pulsed Electric Current Sintering Technique. The pulsed DC current quickly passes through the graphite die (10 mm diameter) and the conductive powder compact, which is the key feature of SPS. This leads in a very high heating or cooling rate, resulting in the samples sintering rapidly. SPS has the ability to densify nano-sized powders without causing grain growth or glassy materials to crystallize. It has been demonstrated experimentally that using pulsed DC current improves densification.

The thermocouple is found 4 mm from the edge of the powder (Figure 2.4.f). It is important to have a good electrical and thermal contact between different components of the die and the powder inside. This was accomplished using graphite paper (Papyex-Mersen) which covers inside of the die (Figure 2.4.a and Figure 2.4.c). After positioning Papyex inside the die (Figure 2.4.d), the first punch was introduced. The papyex disk had a circular form, and it was placed inside the die on the punch's surface (Figure 2.4.b). On the paper-covered surface of the punch, 10 g of powder was added and evenly distributed (Figure 2.4.e). Above the powder, the second circular papyex was placed, and the second punch was put inside the die.

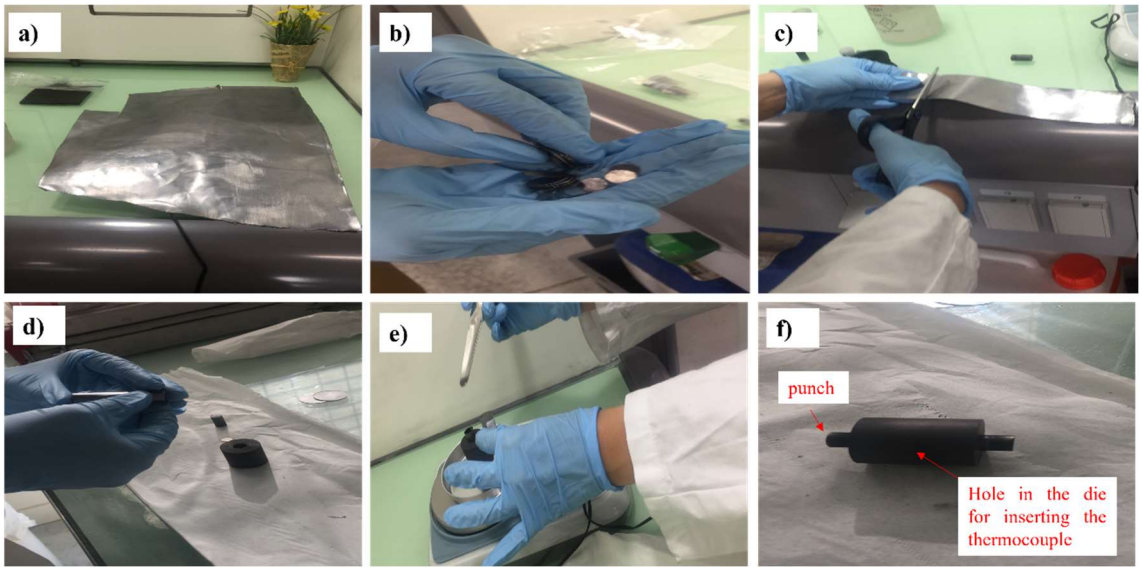

Figure 2.4: SPS protocol for the experiments.

Afterwards, the die was placed in the SPS machine (Figure 2.3). Samples were sintered at 750 °C and 1000 °C (measured using a thermocouple placed into a blind hole in the die wall) using a heating rate of 50 °C/min and two different pressures of 50 MPa and 75 MPa, and then free cooled to room temperature for 10 minutes. Finally, samples of 10mm external diameter and 3mm height were produced. The voltage, current, upper punch displacement, and temperature were all measured during the SPS sintering cycle. The top punch displacement was utilized to measure the densification process.

2.1.4 Uniaxial hydraulic press

The process of compacting powder into a rigid die by exerting pressure in a single axial direction using a rigid punch, plunger, or piston is known as uniaxial pressing. This approach was only employed for the $Fe_{80}X_8B_{12}$ (X=Nb,NiZr) system (Chapter 4).

The three processes of compaction are: placing the powder in the die, pressing the powder, and ejecting the powder compact from the die.

The uniaxial hydraulic press used for compacted the final powders is the Weber PWV30.

The final powders of the $Fe_{80}X_8B_{12}$ (X=Nb,NiZr) alloys were pressed and cylindrical pastilles were created by compacting powder samples weighing between 1.05 and 1.25 g in a vacuum for 30 minutes at a pressure of 600 MPa. The pills measure 10 mm in diameter and 3 mm in thickness.

2.1.5 Density measurements by Archimedes method

This is a precise method for determining the apparent density of as-sintered and as- cast samples. For measurements, a specific kit is utilized (figure 2.5).

Figure 2.5: Density measurement kit.

The sample's weight is measured three times. First, mass is measured in air to determine mass m_1. A second measurement is made for the sample that has been immersed in pure water, and the second mass value, m_2, is calculated. The submerged sample is then retrieved from the water and cleaned. The mass in air is then measured again, giving the third mass value, m_3. We can determine the density of the materials using these three masses:

$$\rho_{sample} = \frac{m_{total}}{v_{total}} = \frac{m_1}{m_3 - m_2} * \rho_{water} \quad (2.1)$$

where ρ_{water} is the water density (ρ_{water} = 1000 kg/cm^3). To determine if the densification process has been finished (Porosity percentage), the sample density must be compared to the theoretical density.

$$D(\%) = \frac{\rho_{sample}}{\rho_{theoretical}} \quad (2.2)$$

2.1.6 Preparation of sample for characterization

After SPS the samples must be polished to eliminate the papyex and show the original sample. A SiC-based polishing material was employed to polish the SPS and AM produced pellets. When a shining surface is generated, the samples were cut using a cutting machine as shown in figure 2.6. SEM imaging and VSM was done with leftover material.

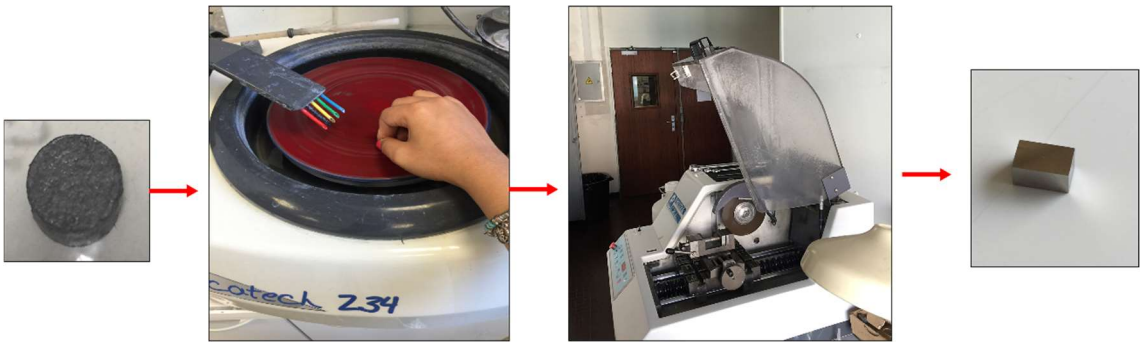

Figure 2.6: Polishing and cut processes.

2.2 Experimental Methods

To analyze the material's characteristics, the powders, as-cast samples, and sintered samples were examined using various techniques such as XRD (X-Ray diffraction), SEM (Scanning electron microscopy), EDS (Energy dispersive x-ray spectroscopy), heat treatments, VSM (vibrating sample magnetometry) and mechanical tests. It should be noted that the ingots obtained after AM and the samples produced after SPS were cut and polished before any characterize technique.

2.2.1 X-Ray diffraction (XRD)

The crystal structures of the phases (obtained after MA, AM, and SPS) and the crystallography parameter in the milled powder were determined using X-ray diffraction. X-ray diffraction (XRD) for structural characterization was performed in a Siemens D500 S diffractometer employing Cu K radiation (λ = 0.154056 nm) at 40 kV and 40 mA settings (Figure 2.7). Diffraction patterns were recorded in the 2θ range from 20° to 120° with a step size of 0.05° and a dwell length of 3 s. The phases present were identified and their structural characteristics estimated using the Rietveld refinement of the XRD patterns with the Maud program [65]. The phases were identified by comparing the

diffraction angles and intensities of the various diffraction peaks with the Xpert High Score Plus tool, which is based on the ICDD PDF2 database.

An effective characterization tool for crystalline materials is X-ray diffraction. A sample X-ray powder diffraction experiment requires placing the sample on the sample holder inside the XRD machine and focusing a collimated monochromatic beam of X-ray radiation on the sample. When conditions satisfy Bragg's Law (eq 2.3), interactions between the incident X-ray beam and the sample's atoms create intense reflected X-rays via constructive interference.

$$n\lambda = 2d\sin\theta \tag{2.3}$$

This law demonstrates the relationship between the wavelength of X-rays (λ), the incidence angle of X-rays (θ), and the distance between the atoms' crystal lattice planes (d) [66]. Constructive interference happens when the difference in the incident X-rays' travel paths is an integer (n) multiple of the wavelength. As the sample is scanned through a range of 2 angles [67], diffracted X-rays are detected, processed, and recorded. This approach produces diffracted beam in all available diffraction directions (for X-rays of a given wavelength) to create the diffraction pattern.

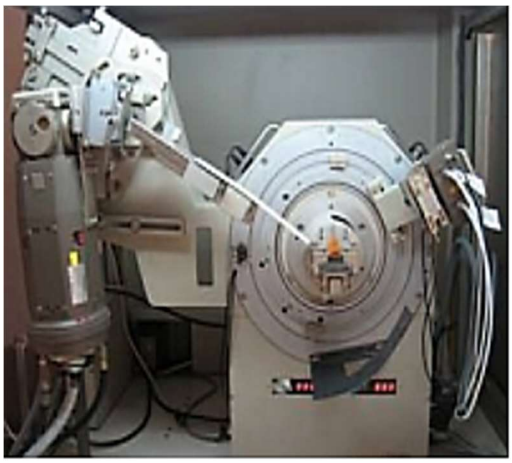

Figure 2.7: Siemens D500 S diffractometer.

2.2.1.1 Rietveld Method

While it was generally understood that powder data might give more information than just cell type and size, obtaining precise structural information was a major challenge owing to diffraction maxima overlap or coincidence. Diffraction from a single crystal

produces well defined intensity points from each crystal plane, which are easily measured. A powder, on the other hand, is made up of randomly aligned crystallites that result in diffraction intensity rings, with the pattern formed being a one-dimensional slice across the rings. As a result, early work was limited to trial-and-error structural characterization or basic phase identification by comparison with other diffraction patterns. Rietveld significantly improved the situation in the mid-1960s by developing a refining procedure that allowed the identification of comprehensive structural information from powdered materials. Powder X-ray diffraction has grown into an incredibly strong technique for structure solving in materials chemistry with the advent of modern computers [68]. The method is based on fitting the obtained diffraction spectra using nonlinear least squares. The Rietveld method's purpose is to minimize the residual function WSS (Weighted Sum of Square):

$$WSS = \sum_i \left(w_i I_i^{exp} - I_i^{calc}\right)^2 \tag{2.4}$$

$$\text{where } w_i = \frac{1}{I_i^{exp}}$$

and refine the compound's crystal structure, such as cell parameters, atomic positions, and Debye Waller factors. The following formula calculates the I_i^{calc} intensity at point i in a power diffractometer for a spectrum collected at a sample orientation (χ,Φ):

$$I_i^{calc}(\chi,\Phi) = bkg_i + I_0 \sum_{n=0}^{N_{phases}} \frac{f_n}{v_n^2} \sum_{k=1}^{N_{hkl}} m_{k;n}\, L_{k;p}\,(2\theta)\, \left|F_{k;n}\right|^2 S_{k;n}\,(2\theta_i - 2\theta_{k;n})\, P_{k;n}\,(\chi,\Phi)\, A_i\,(\chi,\Phi) \tag{2.5}$$

The spectrum is affected by the following factors:

1. Phases: crystal structure, microstructure, quantity, cell volume, texture, stress, chemical composition;

2. Instrument: beam intensity, Lorentz polarization, background, resolution, aberrations, radiation;

3. Sample: position, form, size, orientation, and layers.

Each of these quantities is expressed in terms of parameters that can be refined. The first term in equation (2.5) is the background value, while the second term reflects the diffraction peaks based on the terms:

- diffraction intensity, which defines peak height

- line broadening ($S_{k;n}\ (2\theta_i - 2\theta_{k;n})$) that defines peak shape

- The number of peaks (N_{hkl}) and their positions ($2\theta_{k;n}$)

The background function is represented as a polynomial function:

$$bkg\ (2\theta_i) = \sum_{n=0}^{N_b} a_n (2\theta_i)^n \tag{2.6}$$

The polynomial degree is denoted by N_b. In the case of a complicated background, Maud allows us to choose the N_b value. The interpolation method is used for more complicated backgrounds as well.

The term Sn is a scaling factor for each phase in the intensity expression in equation (2.7):

$$S_n = I_0 \sum_{n=0}^{N_{phases}} \frac{f_n}{v_n^2} \tag{2.7}$$

where I_0 is the measured beam intensity, f_n is the phase volume fraction, and V_n is the phase volume cell.

The Lorentz polarization factor $L_{k;p}\ (2\theta)$ is dependent on the geometry, detector, beam size/sample volume, and has a particular formula for the configuration employed, such as the Bragg Brentano instrument:

$$L_p = \frac{1 + P_h \cos^2 2\theta}{2(1+P_h)\sin^2\theta\cos\theta} \tag{2.8}$$

The structural factor $F_{k;n}$ is written as follows:

$$\left|F_{k;n}\right|^2 = m_k \left|\sum_{n=1}^{N} f_n e^{-B_n \frac{\sin^2\theta}{\lambda^2}}\ (e^{2\pi i(hx_n + ky_n + lz_n)}\right|^2 \tag{2.9}$$

m_k is the multiplicity of the k reflection, which is sometimes given independently in the intensity expression (as in equation (2.9)), f_n is the atomic scattering factor, B_n is the temperature factor (or DebyeWaller), N is the number of atoms, and (x_n, y_n, z_n) are the coordinates of the n^{th} atom.

$P_{k;n}$ is a correction factor for preferential direction, whereas A_i, is the absorption factor. For the Bragg Brentano geometry, $A_i = \frac{1}{2\mu}$, where μ is the sample's linear absorption coefficient.

The following is the profile shape function:

$$S_{k;n}(2\theta_i - 2\theta_{k;n}) \tag{2.10}$$

It may be expressed using several analytical functions such as Gaussian, Cauchy (also known as Lorentzian), Voigt or Pseudo Voigt (PV) function, Pearson VII. Despite the many line profile functions available for profile broadening analysis, there are now indications that the Voigt function, derived from the convolution of a Lorentzian and a Gaussian contribution, must be used. One reason for this is that the convolution of two Voigt functions is a Voigt function, allowing for an easier separation of instrumental and sample effects from the experiment. A PV function is implemented in the Maud program, and the explicit expression is presented in the following formula:

$$PV(2\theta_i - 2\theta_{k;n}) = I_j \left[\eta_k \left(\frac{1}{1+S_{i,k}^2}\right) + (1-\eta_k) e^{-S_{i,k}^2 \ln 2}\right] \tag{2.11}$$

Where: $$S_{i,k} = \frac{2\theta_i - 2\theta_k}{\omega_k}$$

The shape parameters ω and η are represented using the Caglioti and Gaussianity formula in the PV function:

$$\omega^2 = W + V \tan\theta + U \tan^2\theta \text{ (Caglioti)} \tag{2.12}$$

$$\eta = \sum_{n=o}^{N_g} C_n (2\theta)^n \quad \text{(Gaussianity)} \tag{2.13}$$

It is possible to add or delete terms from each of these functions using the Maud software. Next, we must describe the quality refinement factors, also known as refinement estimators, which indicate how well the recalculated spectra from fitting matches the experimental spectra. The Weighted Sum of Squares has already been reported (eq. 2.4):

The two key factors that provide information on the quality of the fitting are the R-indices R_{wp} and R_{exp}, which are defined as:

$$R_{wp} = \sqrt{\frac{(N-P)}{\sum_{i=1}^{N} [W_i I^{exp}{}_i]^2}} \tag{2.14}$$

$$\text{where } w_i = \frac{1}{\sqrt{I_i^{exp}}} \tag{2.15}$$

$$R_{exp} = \sqrt{\frac{\sum_{i=1}^{N} [W_i (I_i^{exp} - I_i^{calc})]^2}{\sum_{i=1}^{N} [W_i I_i^{exp}]^2}} \tag{2.16}$$

where $w_i = \frac{1}{\sqrt{I_i^{exp}}}$

where N represents the number of points and P represents the number of parameters.

R_{exp} is the lowest R_{wp} value that can be obtained with a certain number of refineable parameters. It requires a good weighting mechanism to be efficient. The R_{wp} factor is more dependable in evaluating our analysis. The absolute value of R_{wp} is determined by the background, not the absolute value of the intensities. With a high background, it is easier to get very low values, although increasing the number of peaks (sharp peaks) makes it more difficult to obtain a good result. In general, we can demonstrate that $R_{wp} < 0.1$ corresponds to a satisfactory refinement with a medium complex phase. The goodness of fit is defined as the following:

$$GoF = \frac{R_{wp}}{R_{exp}} \tag{2.17}$$

2.2.2 Scanning Electron Microscopy (SEM)

SEM (scanning electron microscopy) has been employed in every field of nanoscale research. Because of its resemblance to light microscopy, it is an intuitive method of visualizing macromolecular objects. SEM generates a three-dimensional picture by analyzing electrons dispersed or emitted from the specimen's surface [69]. In an electron microscope, an electron beam is formed by thermionic emission of electrons from a metal filament and accelerated by a voltage. SEM can utilize low-energy secondary electrons generated from the specimen's surface following high-energy electron bombardment (SEM). Figure 2.8 shows a schematic diagram of a SEM as well as the SEM used in this work. A condenser lens condenses an electron beam, which is subsequently focused to a very fine point on a sample using an objective lens. The beam can be focused in a tiny probe (2 nm in diameter), which uses scanning coils to deflect over the specimen in a raster way. Secondary electrons may be detected above the material using an electron detector, and a picture depicting the intensity of secondary electrons released from various sections of the sample can be made [70].

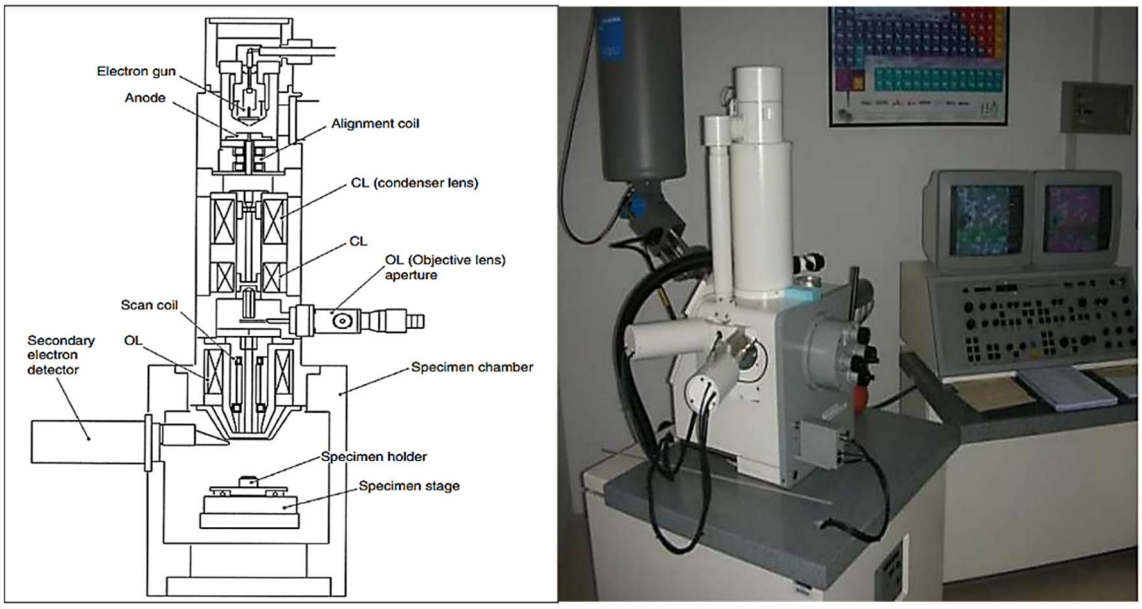

Figure 2.8: Schematic diagram explaining the basic principle of the SEM [71] and a picture of a real SEM.

2.2.3 Energy Dispersive X-Ray Spectroscopy (EDS)

When high energy electrons impact atoms in a sample, a variety of signals are created. Among the signals are secondary electrons, backscattered electrons, and X-rays, which give best information in the SEM [72]. Images formed by backscattered electrons resulting from differing atomic number elements and their distribution in the SEM can achieve compositional contrast. Energy Dispersive Spectroscopy (EDS) can determine what those specific elements are and their relative quantities. Typically, the first step in EDS analysis is to generate an X-ray spectrum from the whole scan region of the SEM. EDS software is often used to connect the energy level of X-rays with the elements and shell levels that created them.

2.2.4 Inductive Coupled Plasma (ICP)

An extremely strong and white plasma made by ions and electrons is generated within a torch composed of three concentric quartz tubes through which an argon gas flow streams to shape the plasma and cool the quartz. As the sample enters the plasma as an aerosol, its molecules are dissolved, atomized, and ionized.

Although certain elements can be ionized to higher charged states, the large proportion of the elements in the sample are ionized to singly charged positive ions with a near-perfect ionization efficiency (100%) [73].

When ionization occurs in the plasma, the ions travel via an interface consisting of two platinum cones (sample cone and skimmer cone) that separates the mass analyser, which operates in a very high vacuum, from the plasma, which performs at atmospheric conditions. A negative voltage separates positive ions from electrons and molecular species at this interface. They are then accelerated and directed into the mass analyzer's entrance using magnetic ion lenses [74].

2.2.5 Thermal Treatments

2.2.5.1 Heat treatment

The as-milled powder of the $Fe_{70}Ni_{12}B_{16}Si_2$ and $FeCoNiB_{0.5}Si_{0.5}$ systems were heat treated in sealed quartz tubes evacuated to 10^{-3} under argon atmosphere. The final powder of $Fe_{70}Ni_{12}B_{16}Si_2$ was first heat treated at 450 °C for 1 hour in an argon environment to avoid oxidation. Following heat treatment, the powder was cooled to room temperature. The second portion of the powder was heat treated at 650°C for 1 hour. For the final $FeCoNiB_{0.5}Si_{0.5}$ powder was heat treated once at 650°C for 1 hour. Annealing was done in an oven at a rate of 15C°/min. After heat treatment, the powders were carried out for XRD and VSM experiments to evaluate the phases formed and their magnetic behavior.

2.2.5.2 Differential Scanning Calorimetry (DSC)

Differential scanning calorimetry is a technique for determining the variation in heat flux emitted or absorbed by a sample when subjected to temperature programming in a controlled environment. Any transformation in a material that occurs during heating or cooling is accompanied by a heat exchange. DSC allows us to determine the temperature and heat of this transformation. Heat flow diagrams as a function of temperature of the $Fe_{80}X_8B_{12}$ (X=Nb,NiZr) alloys were measured for this study using a Mettler Toledo DSC 822 differential tracking calorimeter. After 40 and 80 hours, the $Fe_{80}X_8B_{12}$ (X=Nb, NiZr) powder, agglomerated powder, and compacted samples of the same alloys were heated to 300°C and 600°C. For the kinetic investigation of the main crystallization process the heating was done at four different rates: 5, 10, 20, and 40 K/min, and the entire experiment

was carried out in an argon atmosphere (argon flow rate equals 40 ml/min). In this work, the Kissinger linear fitting procedure was utilized to study the crystallization mechanism.

The Kissinger equation is frequently used to estimate the apparent activation energy for crystallization of the $Fe_{80}X_8B_{12}$ (X=Nb,NiZr) milled, aglomerated, and compacted alloys under continuous heating conditions [75].

$$\ln\left(\frac{\emptyset}{{T_p}^2}\right) = -\frac{E}{RT_p} + constant \tag{2.17}$$

Where $\emptyset$ is the heating rate; E is the process's apparent activation energy ($kJ \cdot mol^{-1}$), R is the gas constant (equal to 8.314 $JK^{-1} \cdot mol^{-1}$) and T_p is the crystallization peak temperature. Plotting $\ln\left(\frac{\emptyset}{{T_p}^2}\right)$ vs $\frac{1}{RT_p}$ yields a nearly straight line with a slope of E (the apparent activation energy of the whole process).

2.2.6 Magnetic Analysis (VSM)

A Vibrating Sample Magnetometer (VSM) comes as one of the measurement options of the PPMS to measure magnetic properties such as hysteresis loop, initial magnetization curve, demagnetization curve, IRM (Isothermal Remanent Magnetization) and DCD (DC demagnetization) curves. Modern vibrating sample magnetometer is considered to be invented in the year of 1955 by Simon Foner at Lincoln Laboratory, MIT, USA [76].
In this work, the hysteresis loops of all samples were investigated by a vibrating sample magnetometer (VSM, Lake Shore) and the Magnetic properties were measured by the Quantum Design (MPMS-VSM and MPMS-XL) the superconducting quantum interference device (SQUID) magnetometer in an applied field (20 kOe). To reduce magnetism from the holder, the sample was placed in a magnetically homogenous sample holder. The holder is attached to a sample rod, which is subsequently powered by a VSM linear motor, which is responsible for the vibrating action. During the measurement, a superconducting magnet is employed to surround the sample with uniform magnetic fields. Measurements are taken by moving a pickup coil in a sinusoidal oscillation. An induced voltage is created and measured using the Faraday Law of electromagnetic induction. Magnetic characteristics of the sample, such as magnetization and hysteresis curve, are therefore detected by transforming the sample dipole field into an AC-electrical signal. An oscillation amplitude with a peak of 1-3 mm and a frequency of 40 Hz is often used to obtain an accurate signal. At a data rate of 1 Hz, a sensitivity to magnetization

changes < 10^{-6} emu could be achieved. Figure 2.9 depicts a typical VSM set up. It is made up of three parts: a VSM linear motor to vibrate the sample, pick-up coils for detection, and electronics to drive the linear motor and detect the magnetic response through the pick-up coils.

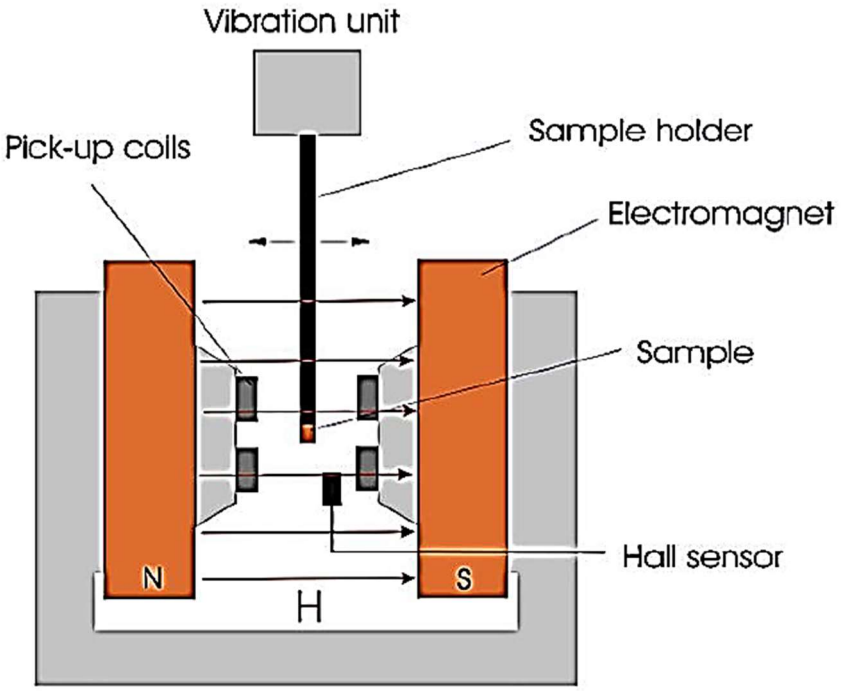

Figure 2.9: Schematic diagram of a vibrating sample magnetometer [77].

As noted previously, the basic idea of the VSM magnetometer is based on Faraday's laws: a voltage is produced in the pick-up coils by a change in magnetic flux caused by sample movement in the applied magnetic field. The mathematical link between magnetic flux, time, and voltage induced is shown in the following equation:

$$V_{coil} = \frac{d\emptyset}{dt} = \left(\frac{d\emptyset}{dz}\right)\left(\frac{dz}{dt}\right) \tag{2.17}$$

Were $\emptyset$ is the magnetic flux confined by the pickup coil and z is the sample vertical position.

SQUID has been used for all magnetic characterizations. The magnetometer Superconducting Quantum Interference Device (SQUID) is a device that detects extremely weak magnetic signals [78]. The SQUID is composed of two parallel Josephson junctions [79] and operates on the interference of currents from each junction. They are inductively linked through a flux transformer to a series of superconducting

detecting coils positioned outside the sample chamber. A closed superconductive circuit is formed by the detecting coils, connecting wires, and input coils. As a result, each variation in magnetic flux recorded by the coils causes a variation in the persistent current flowing through the detecting circuit. This causes changes in the SQUID output voltage that are proportional to the sample's magnetic moment. The SQUID detecting mechanism is seen schematically in Figure 2.10.

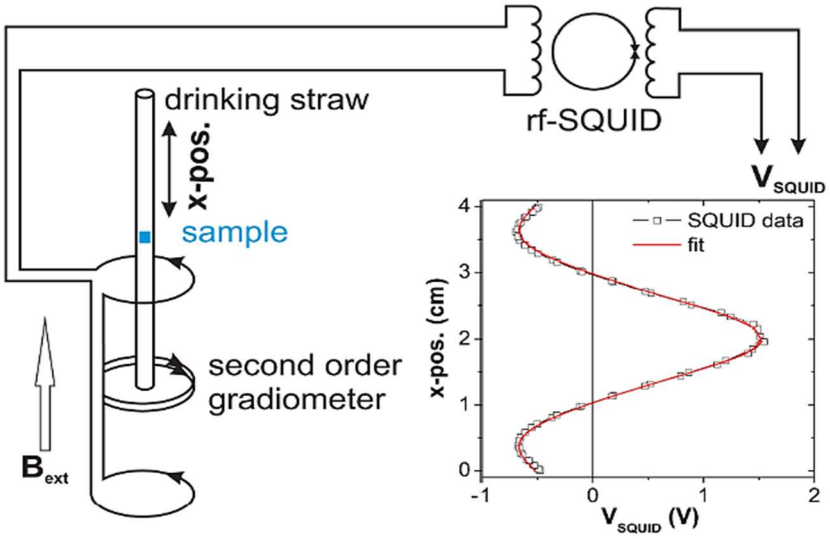

Figure 2.10. Schematic setup of a SQUID magnetometer with 2nd order gradiometer. The inset depicts the SQUID response V_{SQUID} vs sample location (x-pos.) [80]

2.2.7 Mechanical tests

All mechanical tests have been carried out in the stage in the Laboratory ICB at the university of Bourgogne- France.

The mechanical characteristics of all alloys' as-cast and SPS samples were investigated using Vickers hardness and compression tests. Vickers hardness measurement is an indentation technique in which a pyramid-shaped diamond indenter is pushed onto the surface of a mechanically cut and polished sample (Figure 2.11 (a)). The indent's diagonals are measured, and the Vickers hardness is calculated using Equation 2.18, where P is the load (N) and d (mm) is the mean length of the diagonals. In the current investigation, a load of 1.96 N (200g) is applied for 10 seconds to measure hardness.

$$HV = 0.01810 \frac{P}{d^2} \tag{2.18}$$

The hardness tests were carried out with the (Zwick/Roell) Universal Hardness Tester seen in Figure 2.11 (b). Each specimen had at least 9 indentation measurements taken

from different regions, and the average Vickers Hardness (HV) values with standard deviations were determined. For simplicity, the HV values were also converted to MPa by multiplying by 9.807.

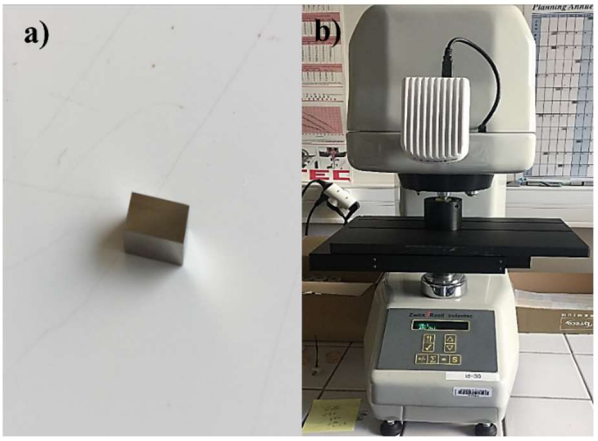

Figure 2.11: Cut and polished sample a), Zwick/Roell Micro Hardness Tester b).

Compression testing is an important sort of mechanical testing. It's employed to figure out mechanical properties like elastic limit, yield strength, and compressive strength. The SHIMADZU AGX-V Universal Testing machine (Figure 2.12) was used to perform a mechanical characterization compression test on the specimens at a speed of 0.1 mm/min, and the related fracture surface characteristics were studied using SEM.

Figure 2.12: Image of SHIMADZU AGX-V Compression machine.

RESULTS AND DISCUSSION

CHAPTER 3

Production and Analysis of $Fe_{70}Ni_{12}B_{16}Si_2$

3.1 Introduction

According to the literature review, iron-nickel alloys have received a lot of interest in both applied and basic science. Because of their soft magnetic characteristics, they are frequently employed in industrial applications. In this chapter, $Fe_{70}Ni_{12}B_{16}Si_2$ (at. %) alloy was prepared by mechanical alloying (MA) in the high-energy planetary ball mill P7. The milling was done at the department of Physics of the Polytechnic High School of Girona-Spain. The analysis of the alloy produced is fundamentally structural, supported by morphological, thermal, and magnetic measurements. The powder X-ray diffraction patterns at various milling times are presented. The diffractograms of the indexed precursors are also provided to identify all of the phases present before milling.

Following Rietveld's analysis, the calculated and experimental diffractograms of the samples for different periods are displayed together applying the MAUD software, which is based on the Rietveld method for the refining of the profiles of the diffraction peaks. It was possible to extract structural information from the samples using the calculated diffractograms, which provided values for the cell parameter, crystal size (L), and the microstrains ($< \sigma^2 >^{\frac{1}{2}}$) for each crystallographic direction hkl and for formed phases. Furthermore, the dislocation density (ρ) for each phase is determined using these three precedent factors.

Despite the relevance of the powders milled at different time and the final as-milled powder, morphological, thermal, and magnetic information are acquired in addition to microstructural information. Images of the morphology of the particles are taken using scanning electron microscopy. The thermal analysis is performed using a differential scanning calorimetry (DSC) to calculate the activation energy, followed by a heat treatment to evaluate the influence of heating on structural and magnetic characterizations of the as-milled sample. Finally, we analyze the hysteresis loops to obtain the coercivity (H_c), saturation magnetization (M_s), remanent magnetization (M_r), and remanence to

saturation squareness ratio (M_r/M_s). The process that has been followed for the synthesis of the alloy $Fe_{70}Ni_{12}B_{16}Si_2$ is summarized in Figure 3.1:

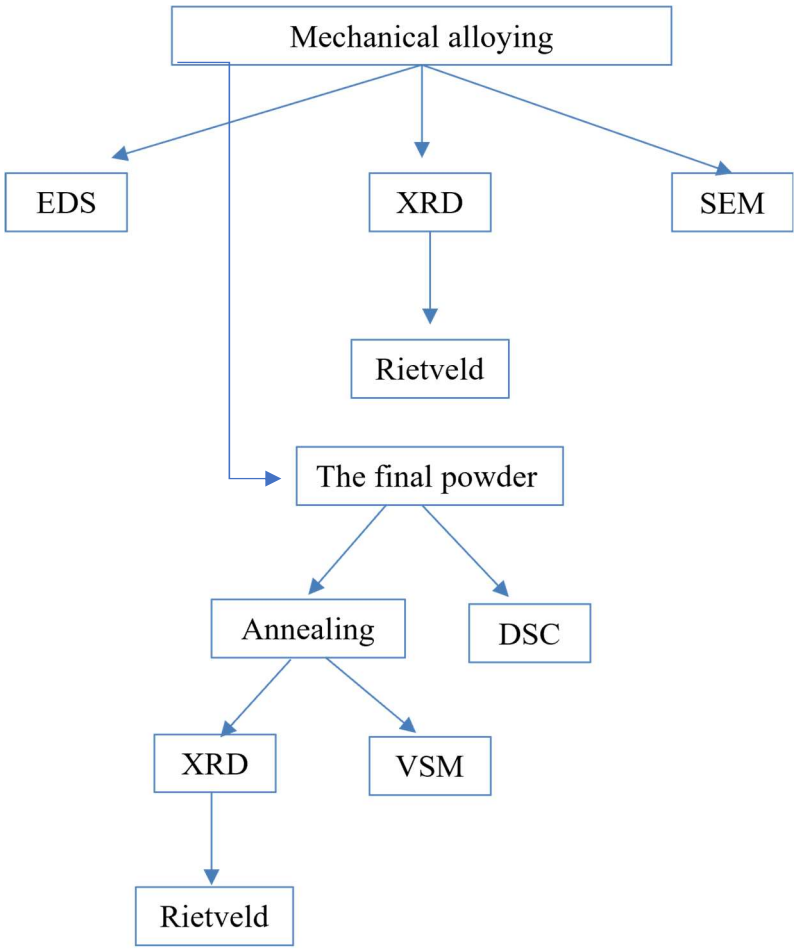

Figure 3.1: Process diagram for synthesis of $Fe_{70}Ni_{12}B_{16}Si_2$ alloy.

3.2 XRD Analysis

This section examines the sample produced from powdered iron (70% at.), nickel (12% at.), silicon (2% at.) in crystalline form, and boron (16% at.) in amorphous form. Energy Dispersive X-Ray Spectroscopy (EDS) has confirmed that the contamination from the vial materials is less than 1% atomic. Figure 3.2 depicts the diffraction peaks of precursors and show the presence of the characteristic peaks of the crystalline structures of three pure elements: BCC-Fe, FCC-Ni, and FCC-Si. Because of its amorphous condition and low atomic scattering factor, B phase diffraction cannot be seen [81,82]. The BCC-Fe, which is the majority phase, presents the reflection peaks (110), (200), (211), (220) and

(310) corresponding to a body centered cubic. The reflection peaks (111), (200), (220), (311) and 222) corresponding to a face-centered cubic (FCC) of Ni, which is the second phase with the greatest presence in the diffractogram. The initial peak of the Ni is seen overlapping with the reflection (110) of the Fe. On the other hand, we can only see the first reflection peak of the Si (111). This is owing to its low atomic number and lower proportion (2% at.) relative to Ni and Fe. Table 3.1 shows the reflections of each phase.

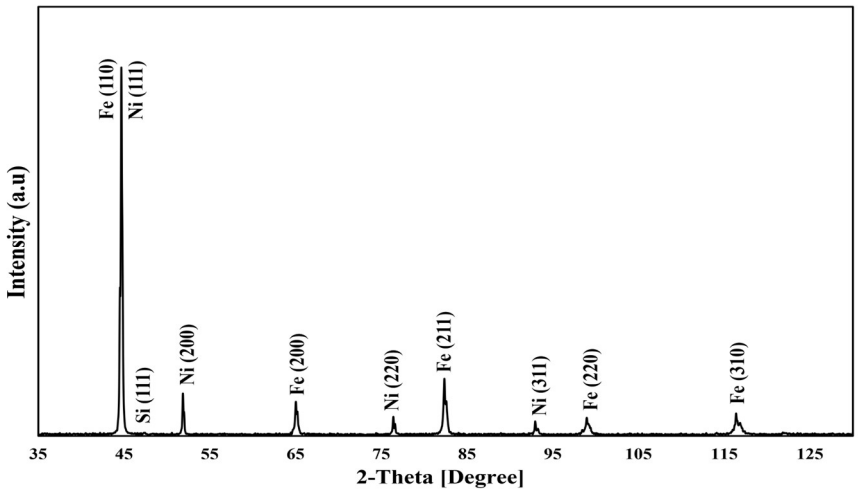

Figure 3.2: $Fe_{70}Ni_{12}B_{16}Si_2$ powder X-ray diffraction patterns before milling.

Phases	Reflections
BCC-Fe	(110) (200) (211) (220) (310)
FCC-Ni	(111) (200) (220) (311) (222)
FCC-Si	(111)

Table 3.1: Reflections present in the diffractogram of the sample $Fe_{70}Ni_{12}B_{16}Si_2$ and corresponding phases.

3.3 Rietveld Analysis

The diffraction peak profiles can be used to characterize the structural and microstructural imperfections produced by the grinding process. Indeed, there are two types of structural imperfections or effects that are likely to significantly change the diffraction peak profile: the size effect and the distortion effect. The lines broaden due to the limited size effect of the coherent diffraction domains (or crystallite size) inside the particles. The distortion effect is caused by a variety of factors, including the existence of crystalline defects (dislocations, vacancies, stacking faults, etc.), thermal expansions or contractions, etc. Thus, their existence, whatever its source, is represented by a distribution of reticular distances around the average distance <d>, leading to a broadening of the diffraction

peaks. In general, the effects of size and microstrain induce a symmetrical enlargement. Figure 3.3 presents the XRD pattern of $Fe_{70}Ni_{12}B_{16}Si_2$ powder before and after milling at different times. Using the Maud program (version 2.55) to stabilize the microstructure, good refinements must be done. The ratio of reliability parameters, GoF (goodness of fit = R_{wp}/R_{exp}), provides information on the quality of fit, where R_{wp} and R_{exp} are the weighted residual error and the expected error, respectively [68]. When GoF approaches 1.0, the best refining is achieved (Table 3.2).

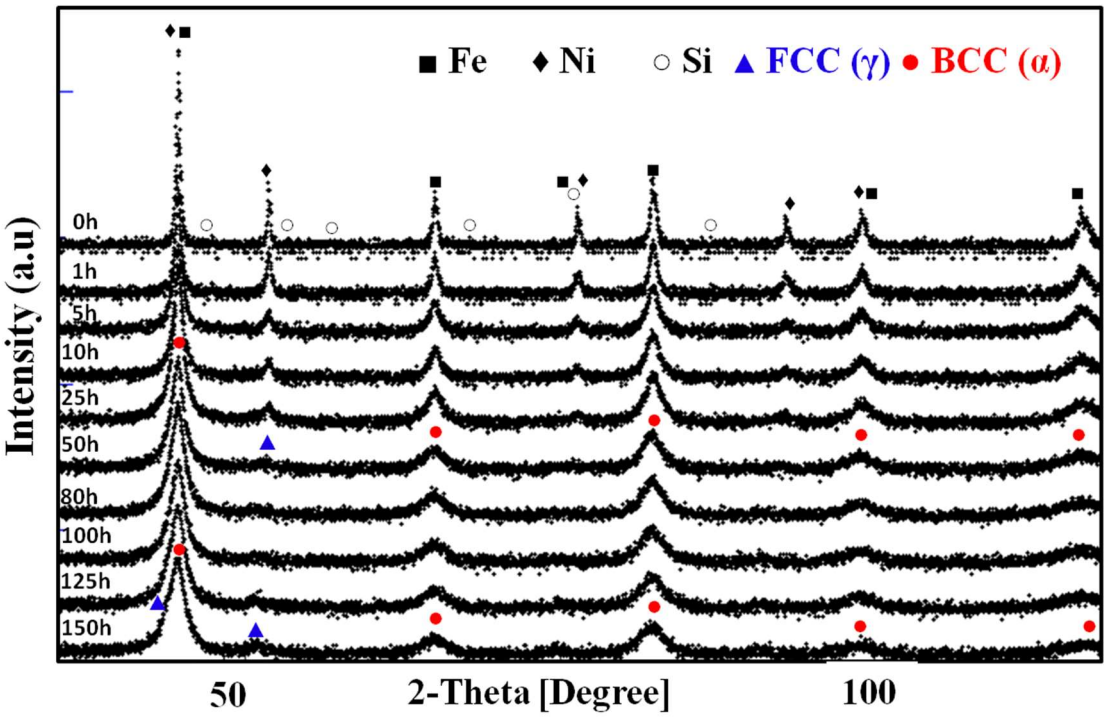

Figure 3.3: $Fe_{70}Ni_{12}B_{16}Si_2$ powder X-ray diffraction patterns as a function of milling time.

Milling time (h)	R_{wp} (%)	R_{exp}(%)	GoF(R_{wp}/R_{exp})
0	3.82	2.95	1.29
1	3.53	3.23	1.09
5	2.49	2.19	1.13
10	2.38	2.20	1.08
25	2.24	1.91	1.17
50	2.30	2.11	1.08
80	2.39	2.07	1.15
100	2.45	2.12	1.15
125	2.38	2.14	1.11
150	2.37	2.17	1.09

Table 3.2: The residual parameters and GoF values of the compounds identified using Rietveld analysis.

The Bragg diffraction peaks corresponding to the pure elements are shown in the X-ray diffraction diagram of the initial powder (figure 3.4): Fe with structure BCC and crystal parameter a = 2.866(6) Å; Ni with structure FCC and crystal parameter a = 3.525(1) Å ;Si with FCC structure and crystal parameter a = 5.430(9) Å. Boron's Bragg peaks do not appear due to its amorphous nature and low form factor.

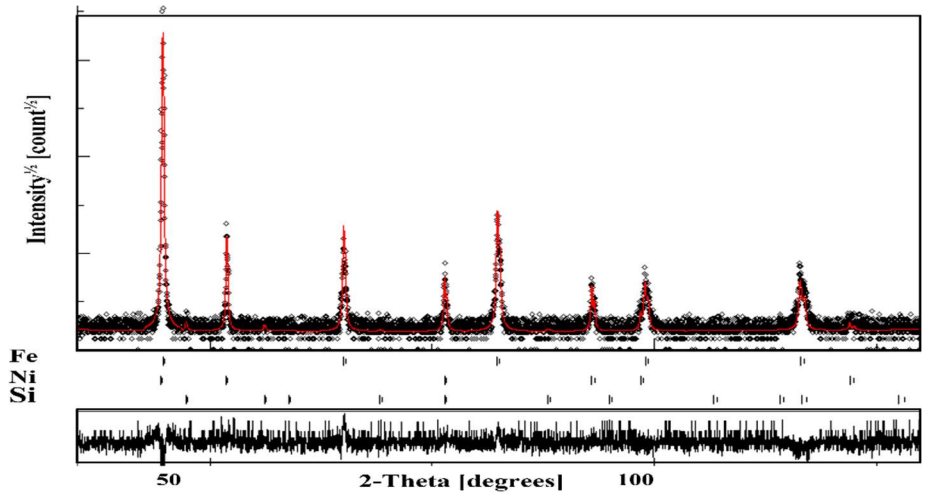

Figure 3.4: X-ray diffractogram of the mixture of $Fe_{70}Ni_{12}B_{16}Si_2$ powders before milling (black line: experimental diffractogram, red line: calculated diffractogram).

The best Rietveld refinement of the X-ray diffraction spectrum of the ground powder for 1 h (figure 3.5) was obtained by the shift of the diffraction peak of Fe towards small angles, this can be explained by the diffusion of B atoms in the Fe lattice and the formation

of the solid solution Fe(B) [83] with a BCC structure in addition to the pure elements: Ni and Si. The decrease in intensity and the broadening of the Bragg peaks of iron and nickel are linked to the reduction in the size of the crystallites and the introduction of different types of defects inside the diffraction domains.

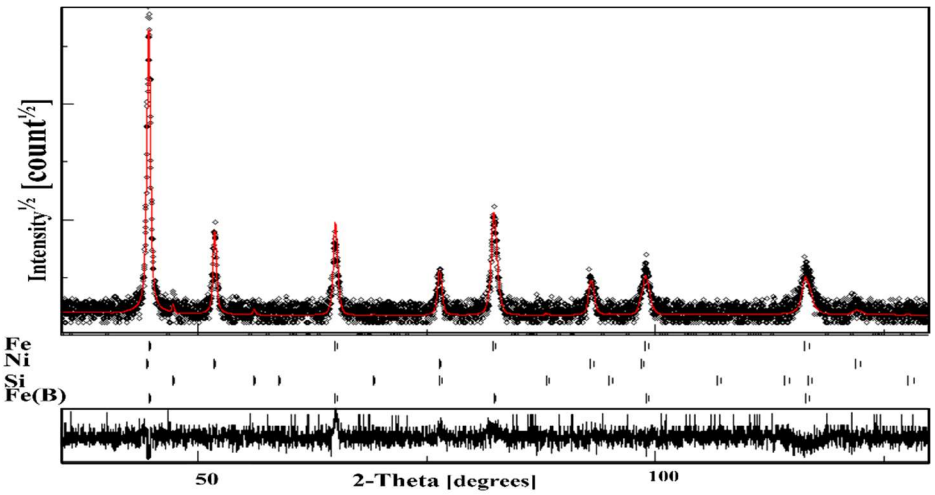

Figure 3.5: X-ray diffractogram of the mixture of $Fe_{70}Ni_{12}B_{16}Si_2$ powders after 1h of milling.

After 5 h, the best Rietveld refinement of the X-ray diffraction diagrams of the ground powders is obtained with the disappearance of the Si peaks and the more broadening and asymmetry of iron peaks, suggesting the production of a supersaturated BCC-Fe (B, Si) solid solution (Figure 3.6). The main phenomena seen in nickel peaks (after 5h) is that their width increases with milling time, indicating a reduction in crystallite size

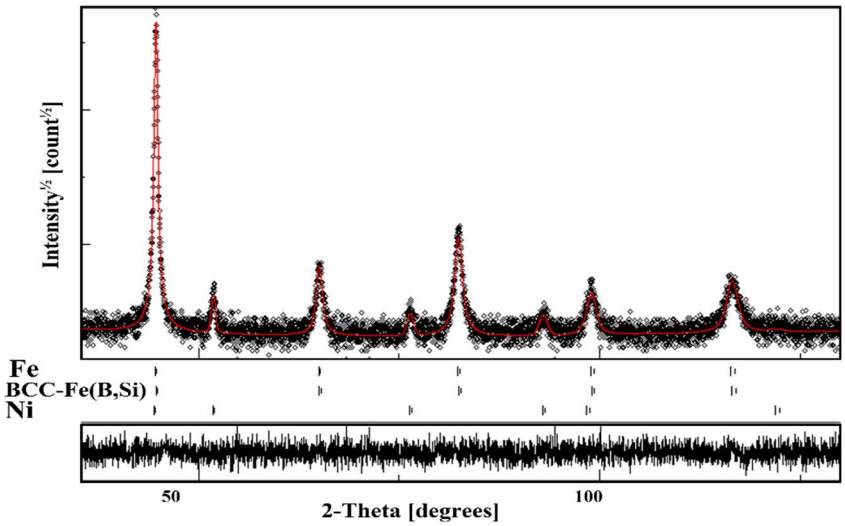

Figure 3.6: X-ray diffractogram of the mixture of $Fe_{70}Ni_{12}B_{16}Si_2$ powders after 5h of milling.

The Fe diffraction peak profiles become more asymmetric and broaden after 25 hours of milling (Figure 3.7). These observations show that Ni slowly interacts with BCC-Fe (B, Si) to give a disordered solid solution BCC-Fe (Ni, B, Si) (α phase, Fe rich). We rule out the diffusion of Fe, B, and Si atoms in the Ni lattice since there is no notable change or asymmetry in the Ni peak. As a result, Fe and Ni interdiffusion cannot occur (as a significant process) during the first 25 hours of milling [84,85].

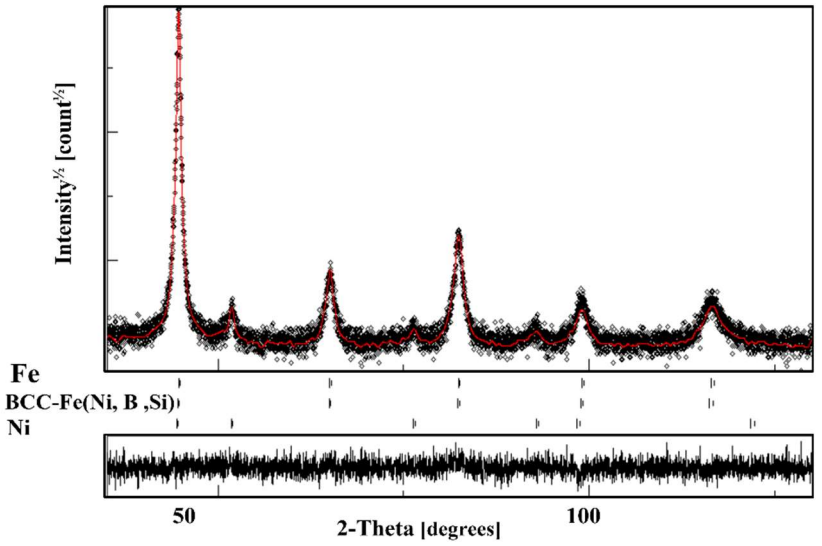

Figure 3.7: X-ray diffractogram of the mixture of $Fe_{70}Ni_{12}B_{16}Si_2$ powders after 25h of milling.

After 50 hours of milling, two disordered solid solutions, FCC and BCC lattice, are formed as a result of a considerable shift in the reflection positions of the FCC-Ni and BCC -Fe towards smaller 2θ angles. As a result, the dissolution of the alloy elements into the Ni lattice is determined at this stage of milling. Finally, because the $Fe_{70}Ni_{12}B_{16}Si_2$ alloy's FCC and BCC solid solutions have disordered structures, Fe, Ni, B, and Si atoms occupy the FCC and BCC lattice sites at random (Figure 3.8). Extending the milling time to 150 hours leads in continuous FCC- phase production as well as an increase in its peak intensity.

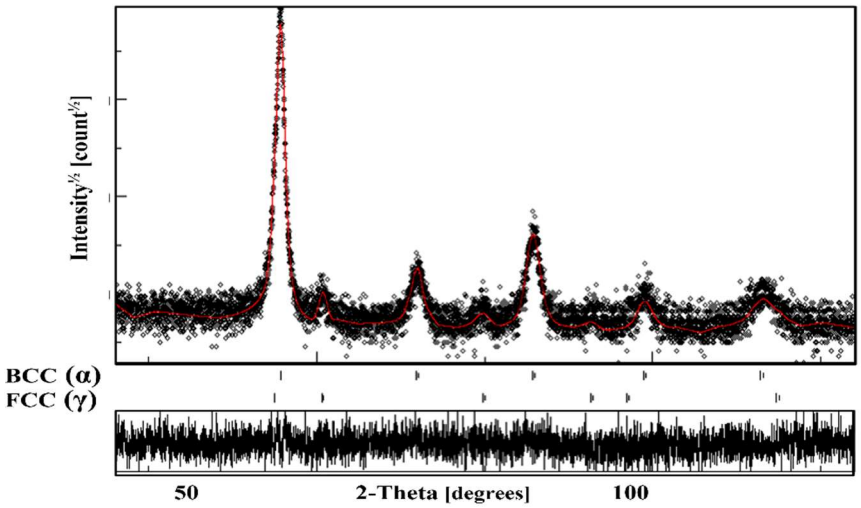

Figure 3.8: X-ray diffractogram of the mixture of $Fe_{70}Ni_{12}B_{16}Si_2$ powders after 50h of milling.

The Fe lattice parameter increases from 2.866 Å to 2.867 Å after 10 hours of milling as shown in figure 3.9. This rise is attributed, first, to crystal lattice distortion induced by considerable plastic deformation, as well as an increase in the density of vacancies and in the dissolution of B atoms (R_B = 0.79 Å) [86] into vacant Fe (R_{Fe} = 1.24 Å) sites. Second, the diffusion of Si atoms (R_{Si} =1.17 Å) [86] in the lattice of the Fe(B) solid solution is attributed. This results a 0.034 % increase so over pure Fe precursor. After 25 h of milling and because of the dissolution of Ni in the Fe (B, Si) matrix, the lattice parameter of the Fe increases with increasing milling time. The Ni atom, on the other hand, is quite similar to the iron atom (R_{Ni} = 1.26 Å) [86]. As a result, the lattice parameter of the BCC-Fe increases and reaches a value of a = 2.869 (5) Å by the end of milling, representing an increase of 0.10% with respect to the precursor of pure Fe. The nickel lattice parameter gradually increases with milling time, going from 3.525(1) Å to 3.532(8) Å at the first 25 hours. This 0.21 % increase is due to the introduction of defects caused by severe plastic deformations. Following the interdiffusion of Ni and Fe, as well as the diffusion of B and Si, the FCC-Ni lattice has suffered further expansion of its crystalline lattice, rising from 3.532(8) Å after 50h of milling to 3.588(1) Å after 80 h of milling. By the end of the milling process, an increase of about 1.78% is detected in the BCC-Fe lattice in comparison to the pure Fe precursor.

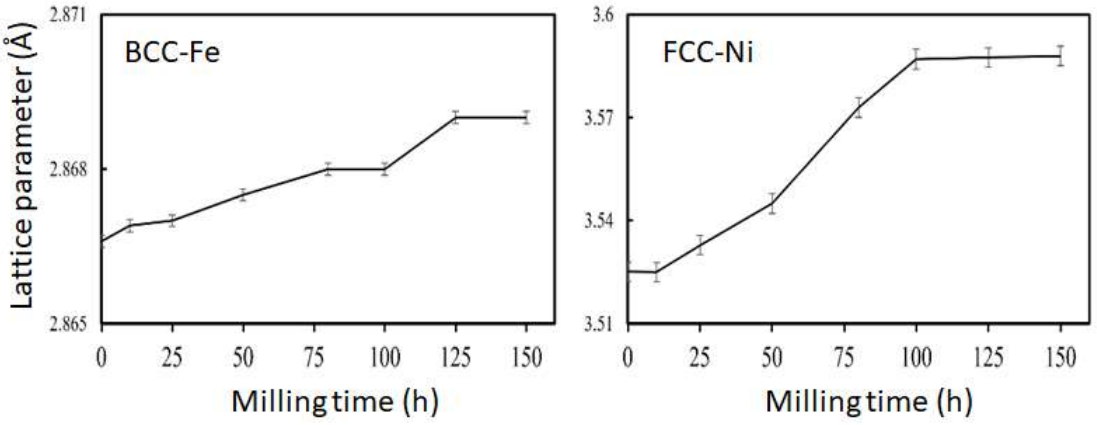

Figure 3.9: The evolution of the principal phases lattice parameters during MA of $Fe_{70}Ni_{12}B_{16}Si_2$.

The evolution of the average crystallite size, <L>, and the microstrain rate, $< \sigma^2 >^{\frac{1}{2}}$, of all phases present in the $Fe_{70}Ni_{12}B_{16}Si_2$ mixture during mechanical alloying is shown in Figure 3.10 and Figure 3.11. The average crystallite size of the Fe reduces fast at the beginning of milling from 155 nm then stabilizes to around 15 nm after 25 hours of milling. During the first milling times, the rate of microstrain rises and becomes practically constant for longer periods of milling reaching a value of about 0.9% at 50 h. Similar tendencies were found for various alloys made using mechanical alloying [87]. For Ni, FCC, and BCC phases, the average microstructural parameters, L and $< \sigma^2 >^{\frac{1}{2}}$, measured by Rietveld refinement of X-ray diffraction patterns, are determined as a function of milling time. The refinement of crystallite size is followed by an increase in the rate of microstrain of powder particles caused by internal stress distribution. These are caused by compositional variances, stacking faults, and other forms of atomic disorder. After 50 hours of grinding, the crystallite size and microstrain rates for Ni are on the order of 15 nm and 0.5 %, respectively. After 150 hours of milling, they are of the order of 10 nm and 0.73 % for the FCC phase, respectively, and 0.63 % and 13 nm for the BCC phase.

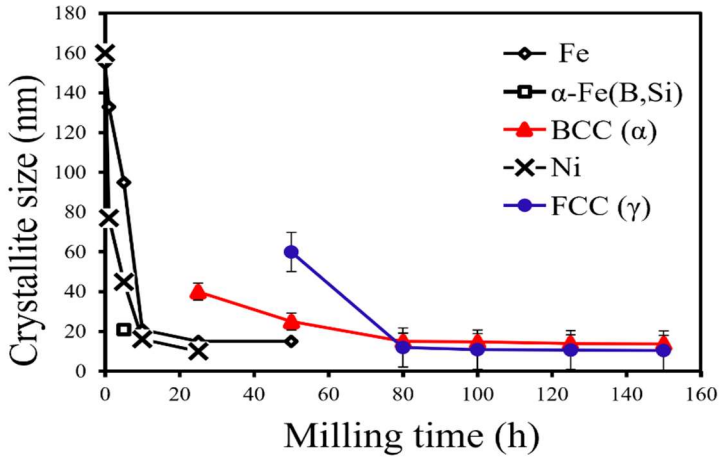

Figure 3.10: Crystallite size parameter as a function of milling time.

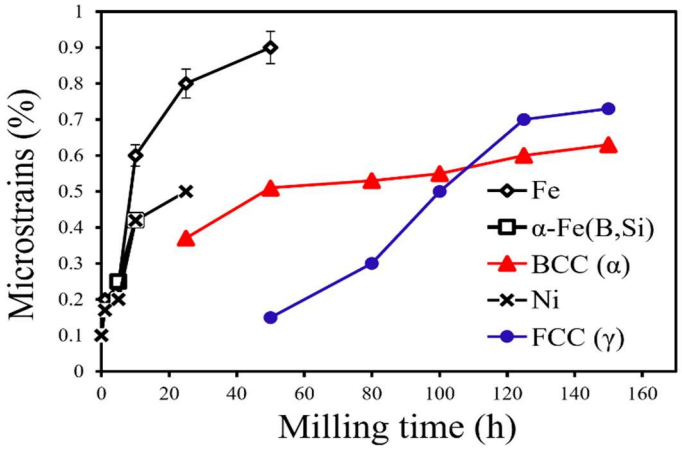

Figure 3.11: Microstrains parameters as a function of milling time.

The dislocation density (ρ) can be calculated using the three parameters obtained, which offers an indication of the amount of defects in the sample, using the following equation 3.1:

$$\rho = 2\sqrt{3}\frac{<\sigma^2>^{1/2}}{L\beta} \tag{3.1}$$

where σ is the microstrain, L is the crystallite size and β is the Burgers vector. The Burgers vector determined by the close-packed planes [hkl] and it is represented by $\frac{a}{n}[hkl]$. Because close-packed planes change for each crystal structure, vector β will also change (see table 3.3).

Crystal structure	close-packed planes	Burger's vector
hcp	$(11\bar{2}0)$	$\frac{a\sqrt{6}}{3}$
bcc	(111)	$\frac{a\sqrt{3}}{2}$
fcc	(110)	$\frac{a\sqrt{2}}{2}$

Table 3.3: Burger's vector depending on crystal structure.

Two crystal structures were provided in this study and during milling, taking into consideration the corresponding Burgers vector. Figure 3.12 displayed the calculated dislocation densities of both BCC and FCC phases in the Mechanical alloyed $Fe_{70}Ni_{12}B_{16}Si_2$. For BCC phase with increasing milling time from 1 to 80 h, we can see a significant rise in ρ from around $0.027 \times 10^{16}/m^2$ to $1.48 \times 10^{16}/m^2$. After 150 hours of milling, there is a slight rise in ρ to $1.755 \times 10^{16}/m^2$. The FCC phase shows a significant increase from about $0.030 \times 10^{16}/m^2$ at 50 h to $0.89 \times 10^{16}/m^2$ at 125 h. The ρ slowly increases till the end of the milling, reaching $0.95 \times 10^{16}/m^2$. Several researchers have discovered a high values of dislocation density in their investigations [88,89].

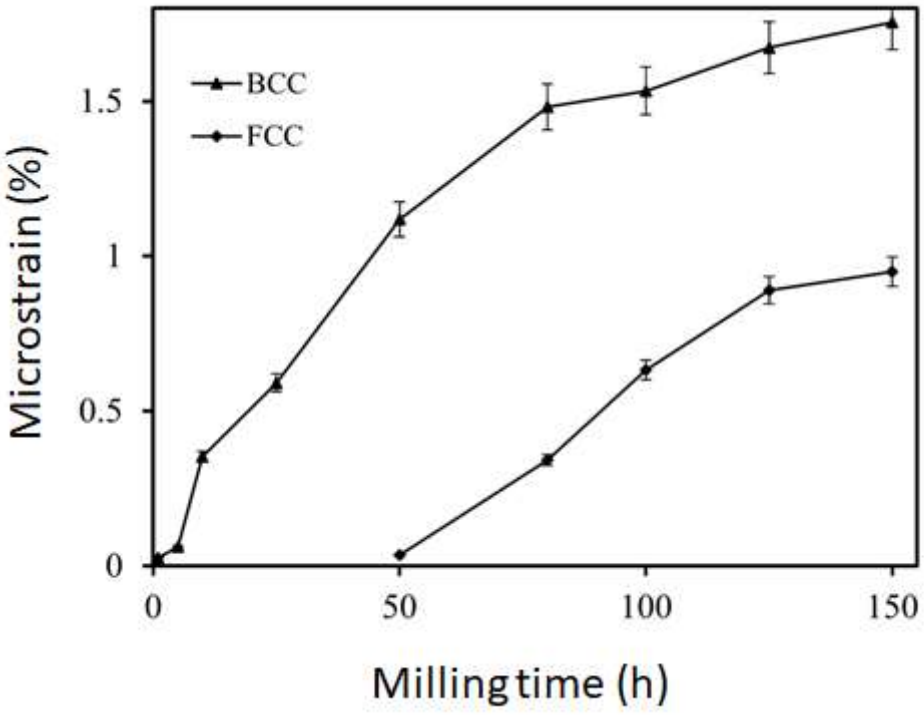

Figure 3.12: Evolution of the dislocation density of the sample's main phases $Fe_{70}Ni_{12}B_{16}Si_2$ during milling time.

The phase proportion of the BCC and FCC phases from 50h is shown in Table 3.4. At 50h (Where begun the coexistence of the two phases), the FCC phase appears to be a minor phase with a proportion of 24% against 76% for the BCC phase. Continuous milling reduces the proportion of the FCC phase. By the end of the milling, only 9% of the FCC and 91% of the main BCC phase were determined.

Milling time (%)	BCC-phase proportion (at. %)	FCC-phase proportion (at. %)
50	76	24
80	86	14
100	87	13
120	89	10
150	91	9

Table 3.4: The phase proportions of the BCC and FCC phases during milling.

3.4 Morphology

Powder particles receive intense mechanical deformation during mechanical alloying and are repeatedly deformed, cold welded, fractured, and rewelded [38]. Figure 3.13 depicts the morphological change of the milled powder during time. Before milling, the powder particles are of different size. Due to agglomeration and cold welding, the particles get larger after 25 hours of milling, with irregular form and size. Both processes are visible at this stage, in addition to the flattening of particle size caused by the injection of compressive forces into the particles caused by consecutive collisions. The mechanically alloyed powder surface (9μm) presents cold welding and fracture site characteristics. The majority of particles decreased after 50 hours. Large particles, on the other hand, can be observed. When the milling time is increased to 150 hours, the powder has a more uniform shape and size and very little agglomeration is noted, indicating a stable state is being reach.

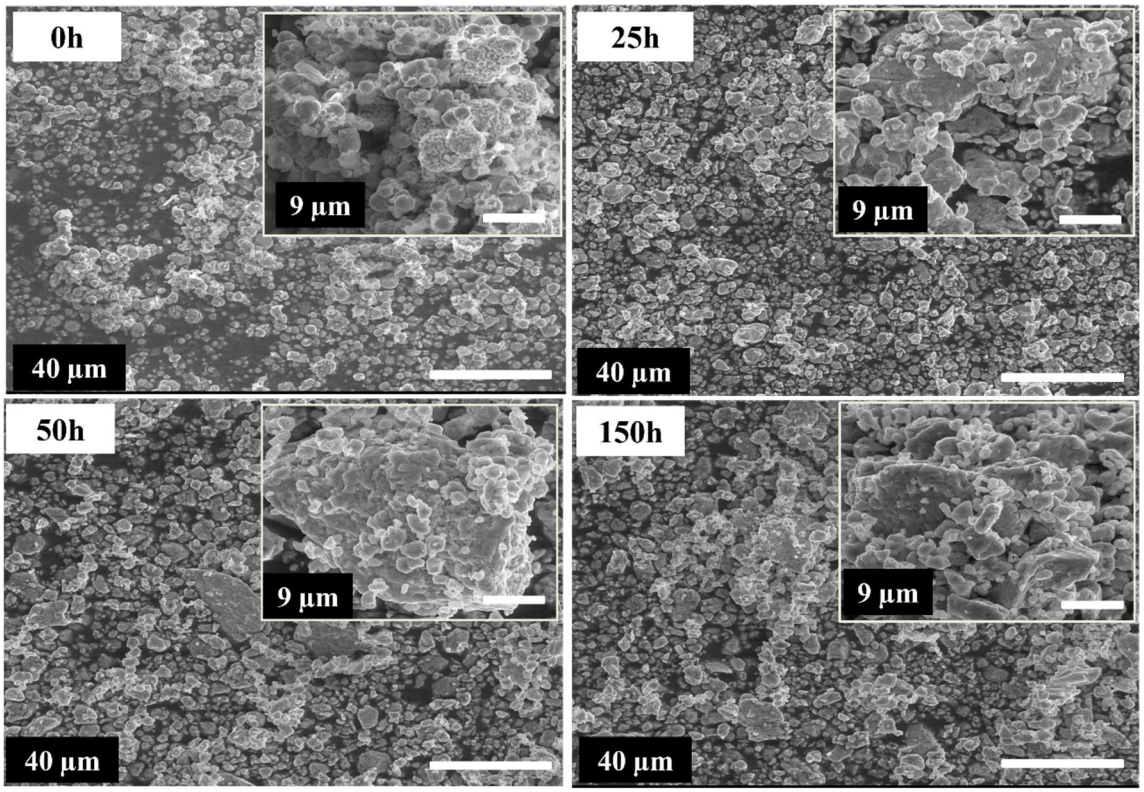

Figure 3.13: Scanning electron micrographs corresponding to mechanically milled powders at different milling time.

3.5 Thermal Analysis

Differential calorimetry studies on the milled sample after 150 hours were carried out in an argon environment at a heating rate of 20ºC/min (figure 3.14). The DSC results show that exothermic reactions occur in the low temperature range (below 400ºC), which is caused by mechanical stress or homogenous magnetization and compositional modification of the existing phase through diffusion. Exothermic processes at higher temperatures (about 565ºC) are associated with the structural change of a considerable quantity of FCC phase to BCC phase, as mentioned later in the XRD patterns. The total enthalpy during the transition is determined to be 196 J/g.

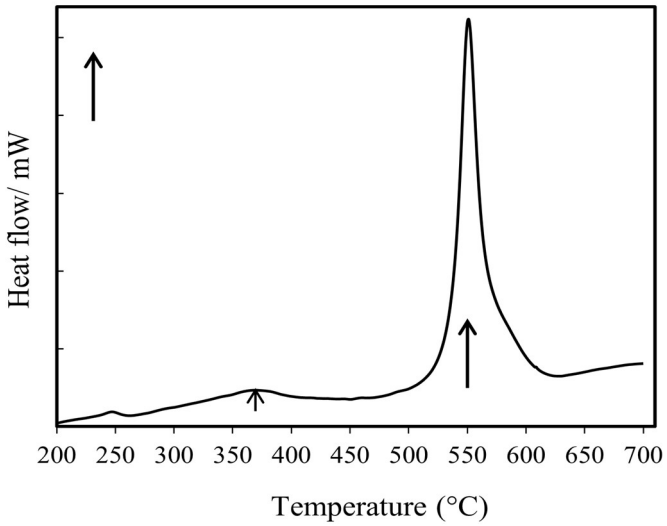

Figure 3.14: DSC thermogram of $Fe_{70}Ni_{12}B_{16}Si_2$ milled for 150 h up to 700ºC, recorded during heating at a rate of 20º C/min under flowing argon atmosphere.

To further understand the influence of heating on structural and magnetic characterizations, the as-milled sample was annealed at temperatures above the reaction temperature range (at 450 ºC and 650ºC for 1 hour in an argon environment) and XRD analyses were performed. The diffraction peaks of the FCC phase become more intense and sharper after the first annealing (as compared to those of the as-milled sample with the presence of the BCC phase). We can assume that the initial phase ratio was metastable and that the disordered solid solution BCC-Fe (Ni, B, Si) develops to (BCC + FCC) at temperatures less than 450ºC (Figure 3.15). After annealing at 650ºC, a significant amount of BCC phase is identified, with a smaller amount of FCC phase; this can explain the FCC to BCC structural transition. This demonstrates that after the second annealing, the weight percentage of the BCC phase increases. As a result, the BCC phase features prominently once more, and adequate annealing can promote a transition from the FCC to the BCC phase. It was anticipated that increasing the heat temperature would increase the amount of FCC phase; however, this was not the case in our study.

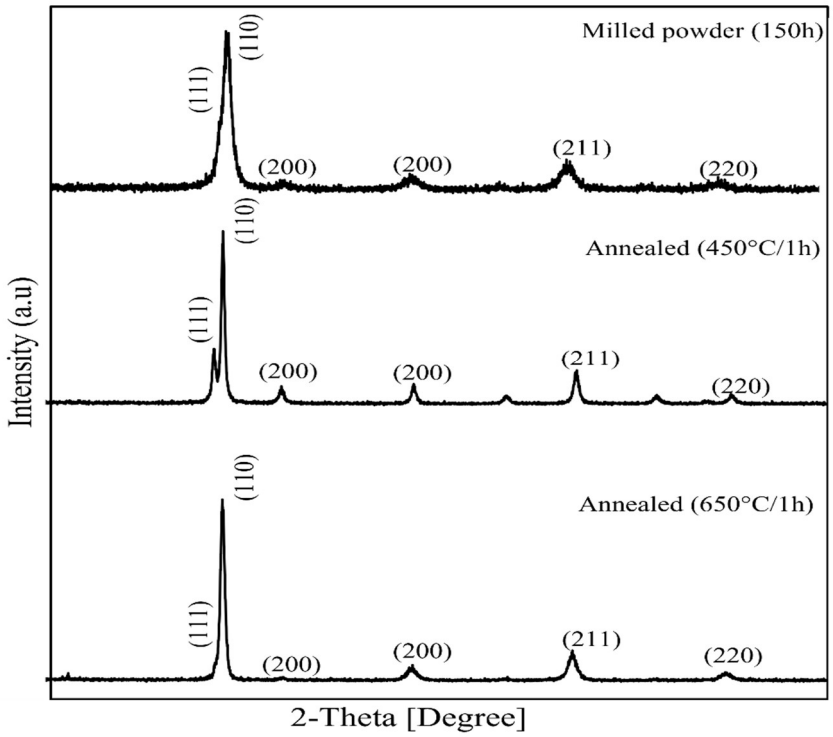

Figure 3.15: X-ray diffraction patterns of MA $Fe_{70}Ni_{12}B_{16}Si_2$ powders after annealing at 450º and 650º C after 150 hours of milling.

As shown in Table 3.5, the percentages, structural and microstructural properties of the BCC and FCC phases changes in annealed and as-milled powders. After 1 hour of annealing at 450 º C, the lattice parameters of the BCC and FCC phases are 2.87 (2) Å and 3.58 (8)Å, respectively. The BCC phase's lattice parameter value remains stable after annealing at 650 º C, but the FCC phase's lattice parameter decreases. This decrease corresponds to the peak's shift toward a higher angle, as seen in the previous Figure 3.15. Annealing, on the other hand, allows the crystallite size to increase while the lattice strain decreases. This is due to the structure getting reordered and the number/density of lattice faults decreasing. As a result, the thermal treatments cause a reduction in internal microstrain as well as nanocrystal growth.

	BCC- phase				FCC- phase			
Treatment	Phase proportion (%)	Lattice parameter (Å)	Crystallite size (nm)	Lattice strain ($<\sigma^2>^{\frac{1}{2}}$ in %)	Phase proportion (%)	Lattice parameter (Å)	Crystallite size (nm)	Lattice strain ($<\sigma^2>^{\frac{1}{2}}$ in %)
As-milled	91	2.86 (9)	13.76	0.63	9	3.58(8)	10.44	0.73
Annealing at 450°C	71	2.87 (0)	38	0.13	29	3.58(8)	28	0.11
Annealing at 650°C	96	2.87 (0)	57	0.04	4	3.57(8)	100	0.05

Table 3.5: The evolution of structural and microstructural properties in the studied alloy after 150 $Fe_{70}Ni_{12}B_{16}Si_2$ hours of mechanical alloying and annealing.

3.6 Magnetic Analysis

The magnetic characterization of the as milled and annealed powders was performed on Vibrating Sample Magnetometry. The magnetic field was applied and the associated moment was obtained to find out the saturation magnetization (Ms), the magnetic remanence (Mr) and coercivity (Hc). Table 3.6 is a summary of all the Ms, Mr and Hc of samples. For each sample, hysteresis loops were plotted (Figure 3.16). These loops are used to calculate the saturation magnetization and coercivity. The as-milled alloy, as well as the annealed sample at 650°C, are both semi-hard (1000 <Hc <10,000 A/m) [6]. while the sample annealed at 450°C is a hard magnetic sample. Magnetization is affected by a variety of parameters, including chemical composition, magnetic atom location, and electronic structures. The total saturation magnetization (Ms) in the current work is dependent on the saturation magnetization of both the BCC and FCC phases. As a result, the Ms of the samples may be determined as follows at room temperature [90]:

$$\Delta M_s = (M_{s,BCC} - M_{s,FCC})\, \Delta V_{BCC}$$

where ΔM_s is the change in saturation magnetization due to the annealing-induced phase transformation, ΔV_{BCC} is the change in the volume fraction of BCC phase and $M_{s,FCC}$ and $M_{s,BCC}$ are the saturation magnetization of the two phases. As a result, Ms has a close connection with V_{BCC}. This is consistent with the results of the XRD analytical analysis and the phase proportions obtained by the Rietveld refinement, in which the weight percentage of the BCC phase drops at 450°C and subsequently increases at 650°C. Table

3.6 demonstrates that the value of Ms drops at 450°C, reaching 109.61 (emu/g), and subsequently increases at 650°C, reaching 148.27 (emu/g).

Annealing at 450°C promotes alloy magnetic hardening by increasing coercivity (134.24(Oe)). Similarly, continual annealing at 650° C diminishes coercivity (70.11(Oe)) while softening semi-hard behavior. This variation might be explained by the following equation 3.2 [91]:

$$Hc \propto \frac{\delta_w K_1}{M_s \mu_0 \bar{r}} V_f^{2/3} \tag{3.2}$$

It can be shown that the coercivity is proportional to the volume of non-magnetic phase (V_f) which is the austenite FCC phase and inversely proportional to the saturation magnetization (Ms). Where δ_w, μ_0, K_1 and $\bar{r}$ are the domain wall thickness, the vacuum permeability, the magneto crystalline anisotropy constant and the average magnetic particle size, respectively. As previously indicated, after annealing at 450°C, the saturation magnetization decreases and the amount of the non-magnetic phase (Vf) increases. As a result of Equation 3.2, the coercivity Hc increases at 450°C. On the other hand, when the saturation magnetization increases after annealing at 650° C, the non-magnetic phase (FCC) decreases significantly. As a result, coercivity reduces at 650° C.

Another interpretation is that annealing at 650°C caused grain growth and then a decrease in coercivity. Figure 3.17 shows that coercivity decreases in function of crystallite size of both BCC and FCC phases.

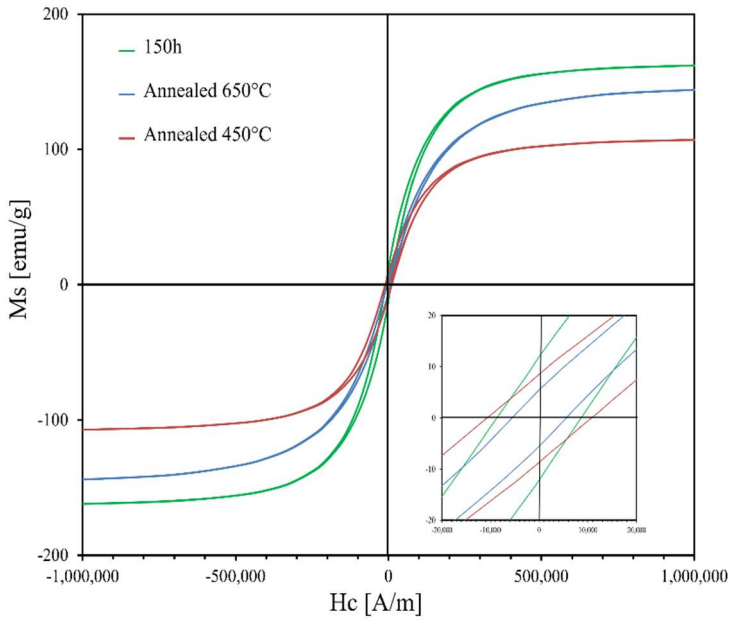

Figure 3.16: Magnetic hysteresis plots of $Fe_{70}Ni_{12}B_{16}Si_2$ powders milled for 150 h before and after heat treatment.

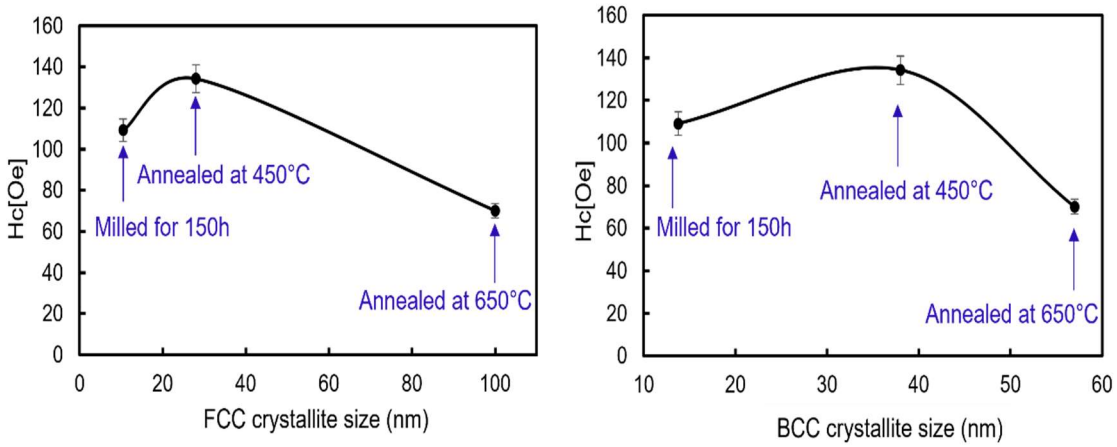

Figure 3.17: Coercivity in function of the crystallite size of FCC and BCC phases during annealing.

Sample	M_s (emu/g)	M_r (emu/g)	Hc (Oe)	M_r/M_s
As-milled	165	12	109.15	0.0724
Annealing at 450°C	109.61	8.51	134.24	0.0777
Annealing at 650°C	148.27	5.46	70.11	0.0368

Table 3.6: Powder saturation, magnetization, coercivity, and squareness ratio (Mr/Ms) before and after annealing.

The variations in squareness ratio (Mr/Ms) before and after annealing are shown in Table 3.5. After annealing at 450°C, the remanence to saturation ratio increases to 0.0777, then drops to 0.0368 after annealing at 650°C. Such behavior is quite similar to the previously reported coercivity changes. This remarkable drop is most likely due to the release of microstrains and the decrease in domain wall energy, as well as the phase transformation from a coexisting BCC+FCC phase at 450°C to a major BCC phase after annealing at 650°C.

CHAPTER 4

Production and Analysis of $Fe_{80}X_8B_{12}$ (X=Nb,NiZr)

4.1 Introduction

Nanocrystalline Fe-M-B alloys, also defined as Nanoperm alloys when M is an early transition metal, have attracted the interest of researchers due to their exceptional soft magnetic properties and are used as ultrasoft magnets in a variety of commercial applications such as telecommunications, microdevices, and power electronics [92]. In this chapter, two samples from the Nanoperm material family are characterized. Specifically, the alloys analyzed are Fe_{80}-Nb_8-B_{12} (at. %) and Fe_{80}-$NiZr_8$-B_{12} (at. %) . Like the samples studied in Chapter 3, the alloys were produced by mechanical alloying (MA) in the high-energy planetary ball mill P7. Because the existence of agglomerated particles was detected throughout the mechanical process in our investigation, a complete examination of the agglomerated particles is necessary. As a result, the current work seeks to explore the morphological, structural, microstructural, thermal, and magnetic properties of alloy powders and agglomerated particles generated by mechanical alloying at 40 and 80 h of milling. To investigate the agglomerated particles generated after 40 and 80 hours of each alloy, they were separated and crushed into powder using a mortar and pestle. At the end of the milling process (80h), the nanocrystalline powders were compacted. After compaction, the microstructure, thermal stability, and magnetic properties were studied. Lastly, annealing was used to enhance the soft magnetic characteristics of the compacted samples. Three samples of each alloy were prepared (one before annealing, one after 300°C annealing, and one after 600°C annealing). The process that has been followed for the synthesis of the alloys is summarized in Figure 4.1 and the chemical composition and labeling of all samples are summarized in Table 4.1.

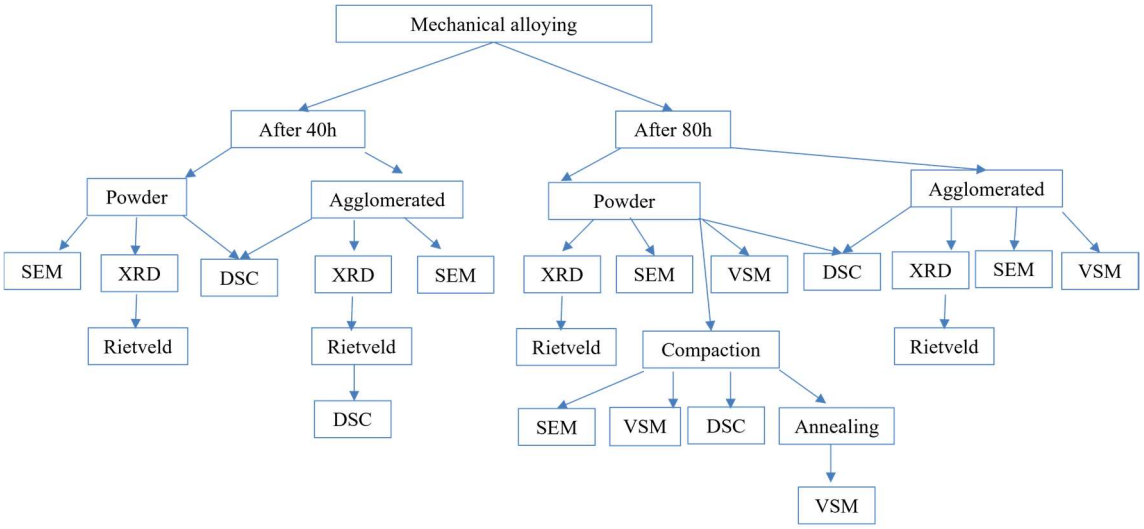

Figure 4.1: Process diagram for synthesis and characterization of Fe_{80}-Nb_8-B_{12} (at. %) and Fe_{80}-$NiZr_8$-B_{12} (at. %) alloys.

Samples	A= $Fe_{80}(NiZr)_8B_{12}$	B= $Fe_{80}Nb_8B_{12}$
MA for 40h (powder)	AP-40	BP-40
MA for 40h (agglomerate)	AA-40	BA-40
MA for 80h (powder)	AP-80	BP-80
MA for 80h (agglomerate)	AA-80	BA-80
MA for 80h (compacted)	AC-80	BC-80

Table 4.1: Samples analyzed in the research with the corresponding label. MA signifies mechanical alloying.

4.2 XRD Analysis

This section analyzes XRD diffraction patterns of the samples A and B, which are made of powdered iron (80% at.), prealloyed $Ni_{70}Zr_{30}$ or Niobium (08% at.), and boron (12% at.) in amorphous form. The only difference between A and B samples is that the $Ni_{70}Zr_{30}$ has been substituted with Nb in the same proportion. Energy Dispersive X-Ray Spectroscopy (EDS) has confirmed that the contamination from the vial materials is less than 1% atomic. Figure 4.2 shows the diffractograms of the powders (after 40h and 80h), agglomerated particles (after 40h and 80h) and the compacted powder after 80h of the sample A. According to the Rietveld analysis results, the predominant crystallographic structure of all of the samples studied is a body-centered cubic (BCC) nanocrystalline structure. The higher intensity peak was measured at an angle 2θ of about 44°. This peak is associated with the -Fe BCC structure and corresponds to the (110) Miller Index. The remaining observed peaks correspond to the Miller indices (200), (211), (220), and (221),

respectively (310). In alloy A milled after 40 and 80 hours, only the α-Fe BCC rich solid solution phase was discovered. However, a NiO minor phase of 5.51% was identified on the compacted specimen after milling the A alloy for 80 hours (AC-80). Similarly, the Rietveld analysis of the sample B milled after 40 and 80h reveals only α-Fe BCC structure matches with the same Miller index as the A sample (Figure 4.3). The exception is that a Nb(B) rich solid solution is found in all B samples. The reaction between B and Nb is due to a negative mixing enthalpy of approximately -39 kJ/mol.

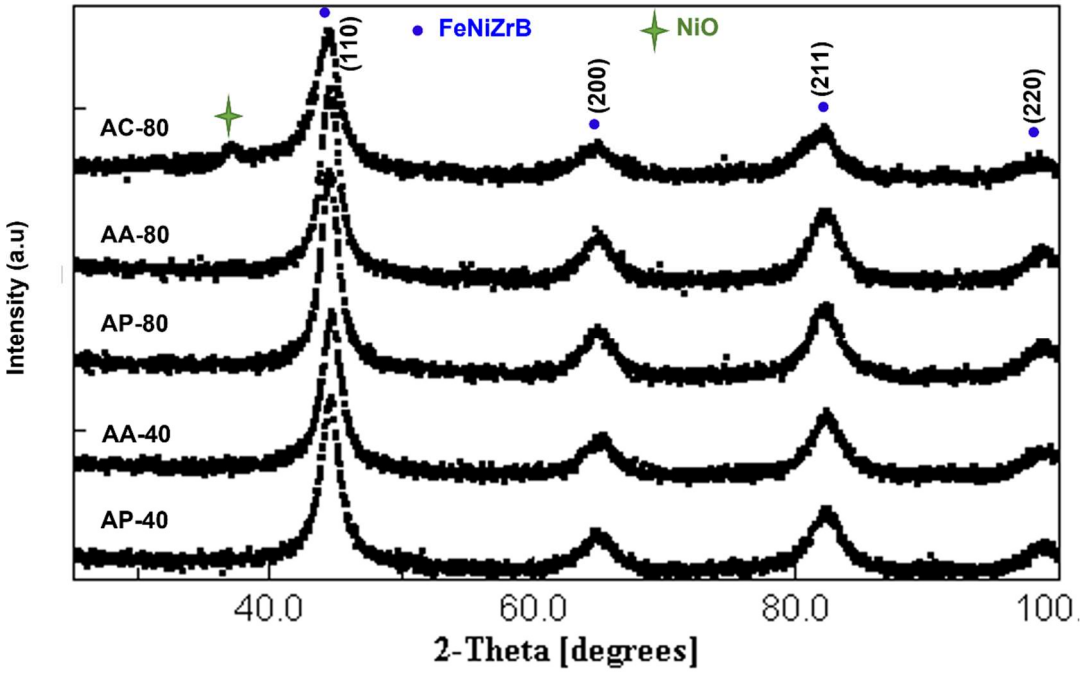

Figure 4.2: XRD diffractograms for samples of A alloy ($Fe_{80}(NiZr)_8B_{12}$).

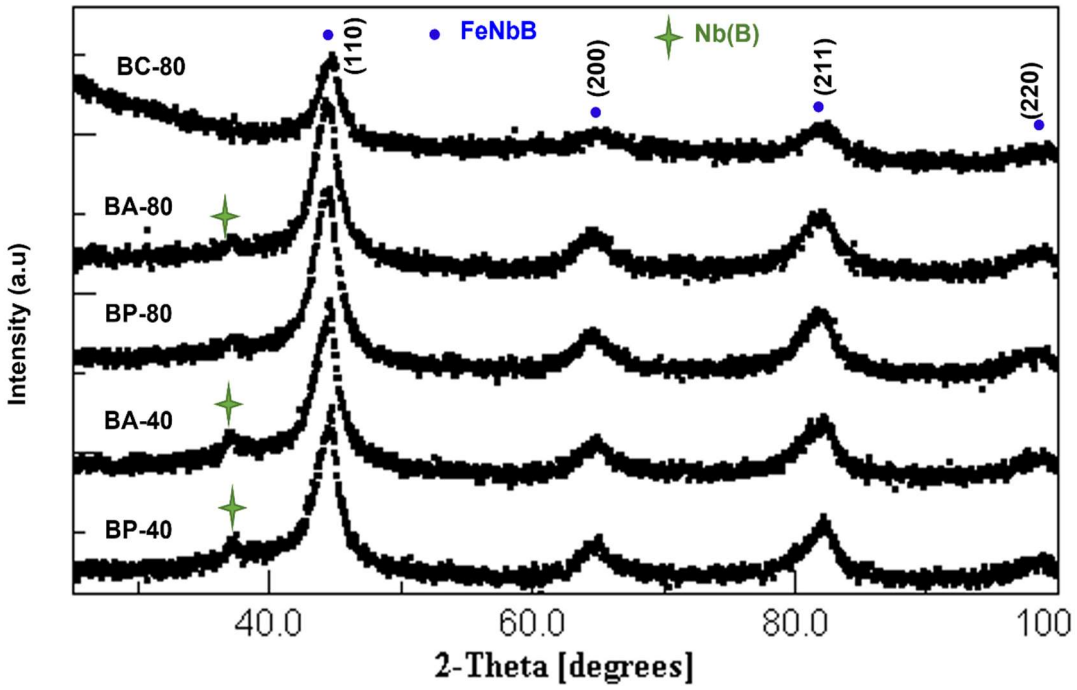

Figure 4.3: XRD diffractograms for samples of B alloy ($Fe_{80}Nb_8B_{12}$).

4.3 Rietveld Analysis

The table 4.2 reveals the ratio of reliability parameters, GoF (goodness of fit = R_{wp}/R_{exp}), that provides information on the quality of fit, where R_{wp} and R_{exp} are the weighted residual error and the expected error, respectively. The table 4.3 illustrates the cell parameter, crystal size, and microstrain index for the A ($Fe_{80}(NiZr)_8B_{12}$) samples. Relevant refining parameters are also supplied. After 40 hours of milling, the A ($Fe_{80}(NiZr)_8B_{12}$) alloy powder and agglomerated particles had approximately the same lattice parameter and crystallite size of 2.869 Å and 11 nm, respectively. The AA-40 agglomerated particles, on the other hand, had a larger microstrain of around 0.53% and a higher value of dislocation densities of approximately 0.79 10^{16} m^{-2}. The AP-40 measured 0.33% microstrain and 0.69 10^{16} m^{-2} dis-location density. The lattice parameters of the powder milled and agglomerated particles (AP-80 and AA-80) grew to nearly 2.870 Å and 2.869 Å after 80 hours of milling, respectively. However, both samples showed an increase in crystallite size of around 14 nm. Microstrain was measured to be 0.55% and 0.61%, with dislocation densities of 0.47 10^{16} m^{-2} and 0.50 10^{16} m^{-2}, respectively. Despite having almost, the same values of lattice parameter and crystallite

size, the agglomerated particles had greater microstrain and dislocation density than the powders milled after the same milling time, according to the microstructure study of the A ($Fe_{80}(NiZr)_8B_{12}$) alloy. The compact specimen milled after 80 hours has the lowest lattice parameter of around 2.869 Å and the greatest crystallite size of around 26 nm. Microstrain and dislocation density were dropped to 0.30% and 0.14 10^{16} m^{-2}, respectively.

Samples	R_{wp}(%)	R_{exp}(%)	GoF
AP-40	16.50	15.257	1.081
AA-40	17.456	16.27	1.072
AP-80	14.920	13.552	1.100
AA-80	16.153	14.396	1.121
AC-80	17.258	13.585	1.270

Table 4.2: The residual parameters and GoF values of the compounds identified using Rietveld analysis.

Samples	a (Å)	Crystallite size (nm)	$< \boldsymbol{\sigma^2} >^{\frac{1}{2}}$ (%)	$\boldsymbol{\rho}$ (10^{16} m^{-2})
AP-40	2.869(4)	11.98 (1)	0.33(6)	0.69(6)
AA-40	2.869(3)	11.19 (5)	0.53(1)	0.79(8)
AP-80	2.870(1)	14.47 (4)	0.55(1)	0.47(7)
AA-80	2.869(9)	14.05 (2)	0.61(3)	0.50(6)
AC-80	2.869(1)	26.11 (3)	0.30(1)	0.14(6)

Table 4.3: Crystallographic parameters and Rietveld refinement results obtained by Rietveld refinement of the A ($Fe_{80}(NiZr)_8B_{12}$) alloy.

The table 4.4 reveals the ratio of reliability parameters, GoF, the weighted residual error R_{wp} and the expected error R_{exp}. The table 4.5 shows the cell parameter, crystal size, microstrain index and refining parameters for the B ($Fe_{80}Nb_8B_{12}$) alloy samples. The microstructure findings for the B alloy samples milled for 40 h show that the agglomerated particles had a higher lattice parameter 2.877 Å and a higher crystallite size (12.15 nm) than the powders milled (2.876 Å, 8 nm, respectively). The SEM pictures (see the next paragraph), which indicated that the agglomerated particles formed after 40 hours seemed to have enormous diameters, confirms this outcome. As a result, although having approximately the same crystallite size, the agglomerated particles had a higher lattice parameter (2.880 Å) after 80 hours of milling than the milled powders (2.876 Å). As

detected in the A alloy, agglomerated samples of the B alloy produced after 40 and 80 h show higher microstrain and dislocation density than milled powders. The compact sample of the milled powders has a lattice parameter of nearly 2.879 Å and a crystallite size of around 15 nm after 80 hours. The dislocation density and microstrain were dropped to 0.41 10^{16} m^{-2} and 0.44%, respectively.

Samples	Rwp(%)	Rexp(%)	GoF
BP-40	18.657	14.924	1.250
BA-40	20.490	14.26	1.43
BP-80	16.36	13.17	1.241
BA-80	16.09	13.65	1.178
BC-80	14.89	13.49	1.06

Table 4.4: The residual parameters and GoF values of the compounds identified using Rietveld analysis.

Samples	a (Å)	Crystallite size (nm)	$< \boldsymbol{\sigma^2} >^{\frac{1}{2}}$ (%)	$\boldsymbol{\rho}$ (10^{16} m^{-2})
BP-40	2.876(1)	8.21 (1)	0.34(3)	1.48(3)
BA-40	2.876(9)	12.15 (3)	0.46(8)	0.67(7)
BP-80	2.876(4)	12.02 (6)	0.48(7)	0.69(2)
BA-80	2.880(9)	11.78 (1)	0.51(1)	0.72(1)
BC-80	2.879(7)	15.45(2)	0.44(1)	0.41(8)

Table 4.5: Crystallographic parameters and Rietveld refinement results obtained by Rietveld refinement of the B ($Fe_{80}Nb_8B_{12}$) alloy.

The XRD analysis confirms the microstructural differences between the powdered and the agglomerated specimens.

4.4 Morphology

Figure 4.4 depicts the morphology of samples AP-40, AA-40, and AC-80. There is a significant variation in the homogeneity of particle size (micrometric range) for powders and agglomerated particles of both alloys. In sample A, the comparison was feasible because the agglomerate particles deagglomerated quickly, allowing the particle size distribution to be assessed. Agglomerates arise as a result of particle deformation and welding during milling. The bulk of the AP-40 particles have sizes of up to 10 μm and are observed below 3μm. However, as expected, the particle diameter increases

significantly between the powder and agglomerate forms. The majority of AA-40 particles have sizes of up to 34 μm and are observed below 10 μm. The compacted sample shows visible pores.

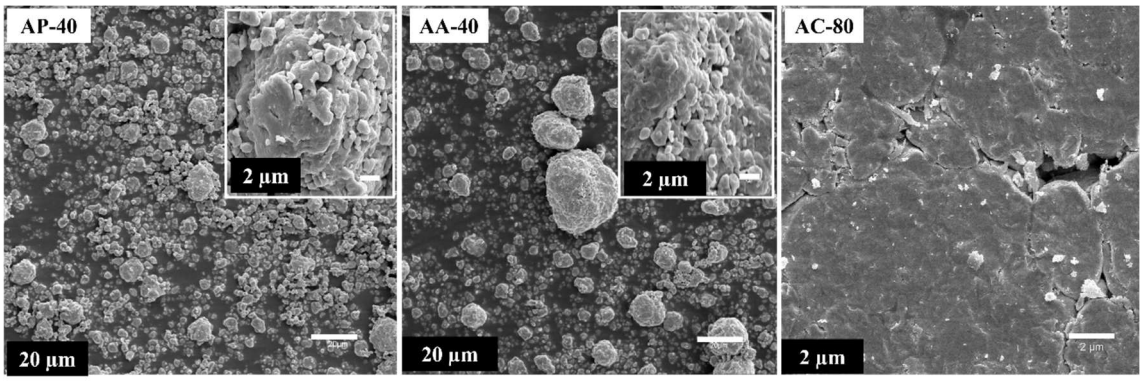

Figure 4.4: SEM images corresponding to samples AP-40, AA-40, and AC-80.

The morphology of samples BP-40, BA-40, and BC-80 is depicted in Figure 4.5. The maximum number of particles for BP-40 is less than 4 μm. However, because to the sample's agglomeration tendency, we discover diameters of up to 46 m in this example. As expected, and plainly evident on the SEM images, the majority of the particles in the agglomerated phase (BA-40) are found below 15 μm with sizes up to 55 μm. In compared to other elements, the Nb in this alloy has a low density, great ductility, and good formability, which explains the agglomeration propensity [93]. The consolidated BC-80 was more susceptible to compacting than the AC-80. (Figure 4.4)

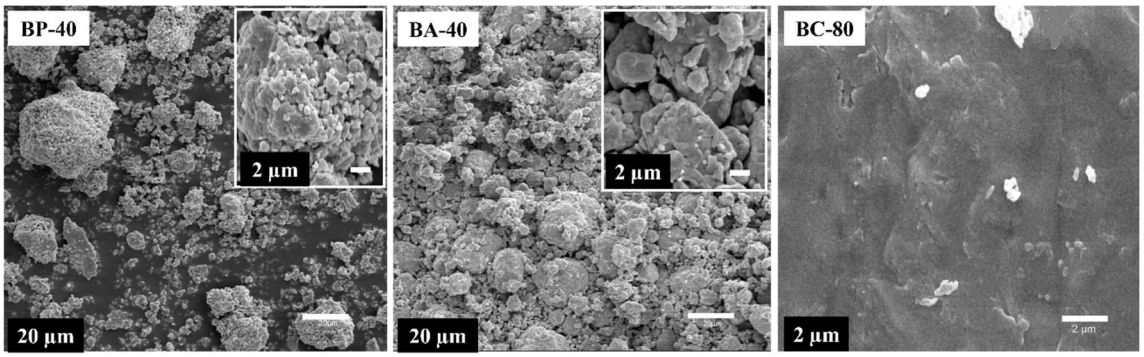

Figure 4.5: SEM images corresponding to samples BP-40, BA-40, and BC-80.

4.5 Thermal Analysis

In this section, the powders and agglomerated particles containing Nb, as well as those containing the combination NiZr, have been subjected to a series of differential calorimetry tests in an argon atmosphere (Figure 4.6 and 4.7). Exothermic processes were

seen at low temperatures (below 400°C) in alloy A (AP-40, AA-40, AP-80, and AA-80) when mechanically induced tensions were released at the micro and nanoscale. Furthermore, heat treatment enhances atomic diffusion, which lowers local inhomogeneity and crystallographic defects. The peak temperature of the powders AP milled after 40h is lower (Tp 484° C) than that of the agglomerated particles AA milled after the same period (Tp 495° C). The highest temperatures of the powders and agglomerated particules after 80 hours were substantially equal at 483° C and 482° C, respectively. At low temperatures (between 300 and 400°C), the alloy B (BP-40, BA-40, BP-80, and BA-80) displayed the similar relaxation characteristic as the A alloy's samples. Crystallization (crystalline growth and/or nucleation) was related to higher temperature exothermic processes seen in both alloys. Mechanically alloyed nanocrystalline alloys exhibit this complex behavior [94]. A wide exothermic process commencing at 400 ° C for all samples of the B alloy might be produced by early surface crystallization (particle surface) associated with stress [95]. For the compacted samples (AC-80 and BC-80), exotermic processes corresponding to relaxation phenomena were found below 200° C. The exotermic peak associated with the crystallisation process was detected at 400° C for AC-80 and 500° C for BC-80.

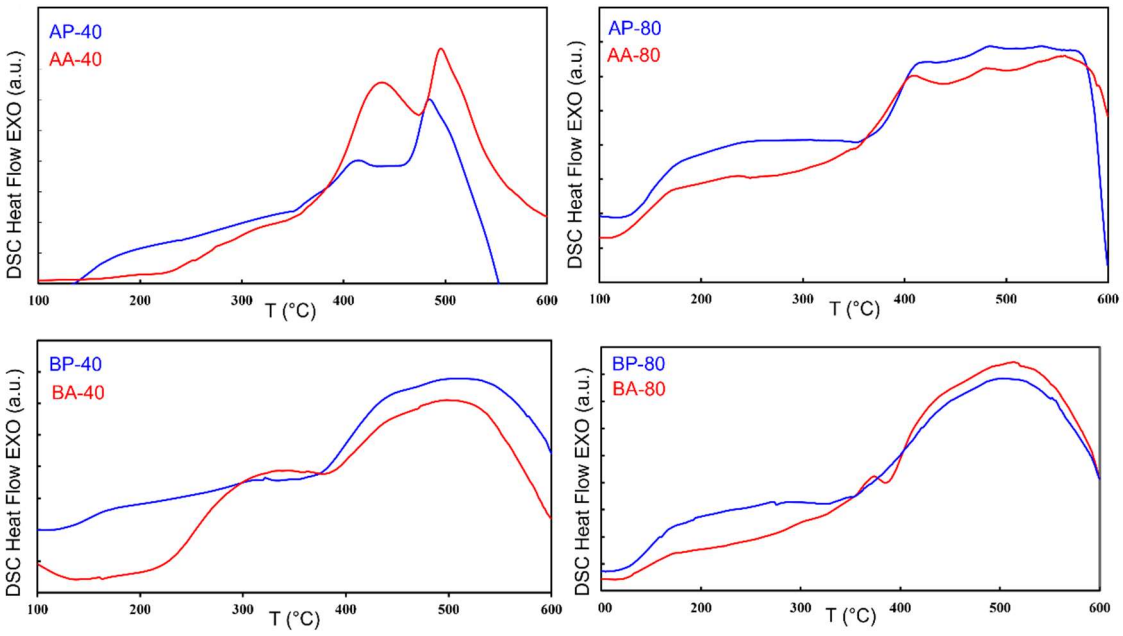

Figure 4.6: DSC curves collected in pairs for samples (AP-40 and AA-40), (AP-80 and AA-80), (BP-40 and BA-40) and (BP-80 and BA-80) to observe the behavior of powders and agglomerated particles after the same milling duration.

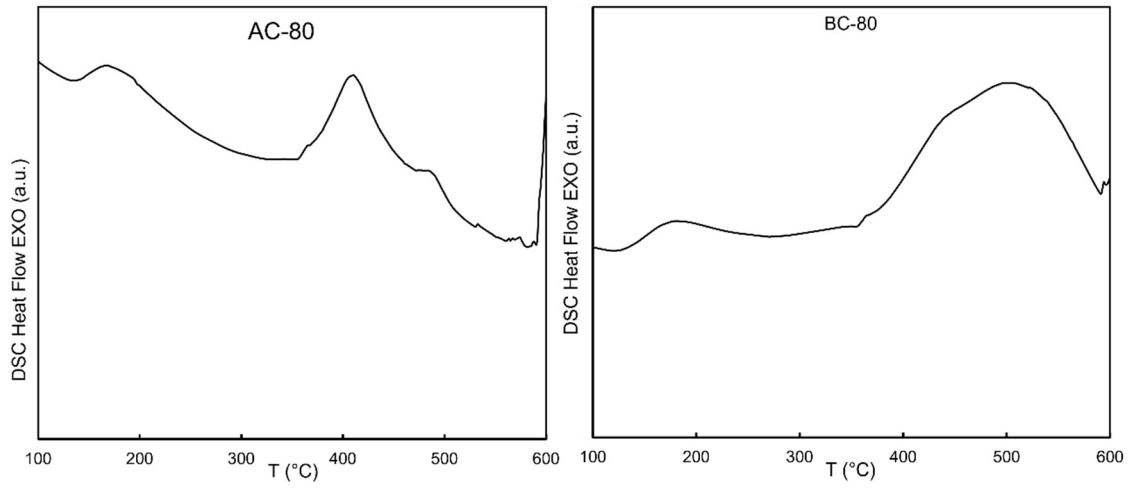

Figure 4.7: DSC curves of the compacted samples AC-80 and BC-80.

Figures 4.8 and 4.9 show the linear fitting, while table 4.6 shows the apparent activation energy. The apparent activation energy is calculated from the slope of the linear fit of the $\ln(\beta/T_p^2)$ versus $1/T_p$ (where β is the heating scan rate and T_p is the peak temperature) using the following formula, where R is the universal gas constant:

$$E = -(slope \cdot R)$$

The activation energies of alloys A and B are higher in agglomerated particles than in powdered particles (at 40 hours of milling). One probable explanation is that diffusion and homogeneity inside the agglomerated particle help to prevent crystalline growth, resulting in a higher activation energy. Alloy A milled for 80 hours exhibits the same effect, but the alloy B displayed the opposite behavior after being milled for 80 hours; the agglomerated particles BA-80 have a lower activation energy than the powders BP-80. One probable reason is the high amount of Nb(B) phase ~ 5% in the BA-80 (according to the Rietveld refinement), which might have affected nucleation and/or crystal formation. The BP-80 presented approximately 1.9 % of the Nb(B) phase. The Nb(B) content of the BA-40 and BP-40 powders was nearly similar, 3.8% and 3.0%, respectively. Lastly, those findings also show that the B alloy samples had higher thermal stability than the A alloy samples. This phenomenon can be explained by the fact that Nb has a higher heat of solution in Fe matrix than Ni and Zr. The activation energy of the compacted specimens is close to that of the original powders produced by mechanical alloying.

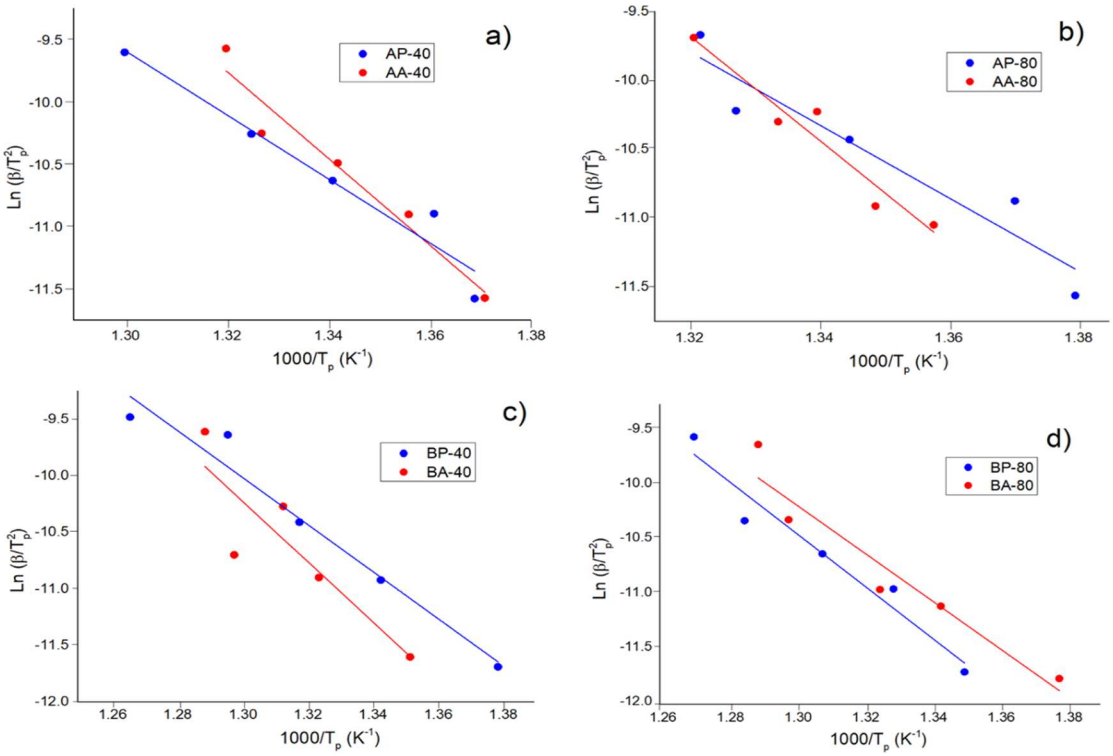

Figure 4.8: Kissinger linear fitting to determine the activation energy of the crystallization process of the powders and agglomerates (each experimental point correspond to peak temperatures measured at 5, 10, 20, and 40 K/min). a) Sample A-40h, b) Sample A-80h, c) Sample B-40h and d) sample B-80h.

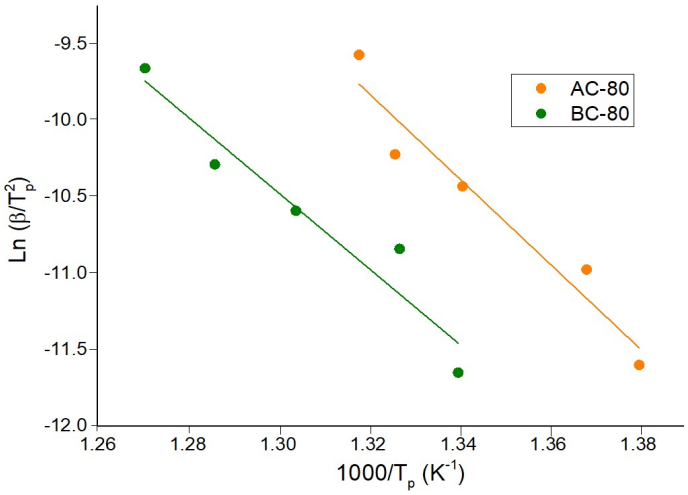

Figure 4.9: Kissinger linear fitting to determine the activation energy of the crystallization process of the compacted specimens (each experimental point correspond to peak temperatures measured at 5, 10, 20, and 40 K/min).

Samples	Activation energy /kJ mol^{-1}	Samples	Activation energy /kJ mol^{-1}
AP-40	214 (6)	BP-40	173 (13)
AA-40	290 (4)	BA-40	222 (6)
AP-80	221 (18)	BP-80	199 (5)
AA-80	314 (9)	BA-80	182 (3)
AC-80	231 (20)	BC-80	205 (10)

Table 4.6: The activation energy of the main crystallization process in samples A and B.

Thus, the thermal analysis also confirms the differences between powders and agglomerated specimens.

4.6 Magnetic Analysis

The magnetic hysteresis cycles for alloys A and B at room temperature are shown in figure 4.10 of this section. This sort of curve hysteresis cycle is generally observed in nanostructured materials with small magnetic domains. This is due to the presence of structural defects among grains, as well as a high density of nanocrystals, which prevent domain wall movement.

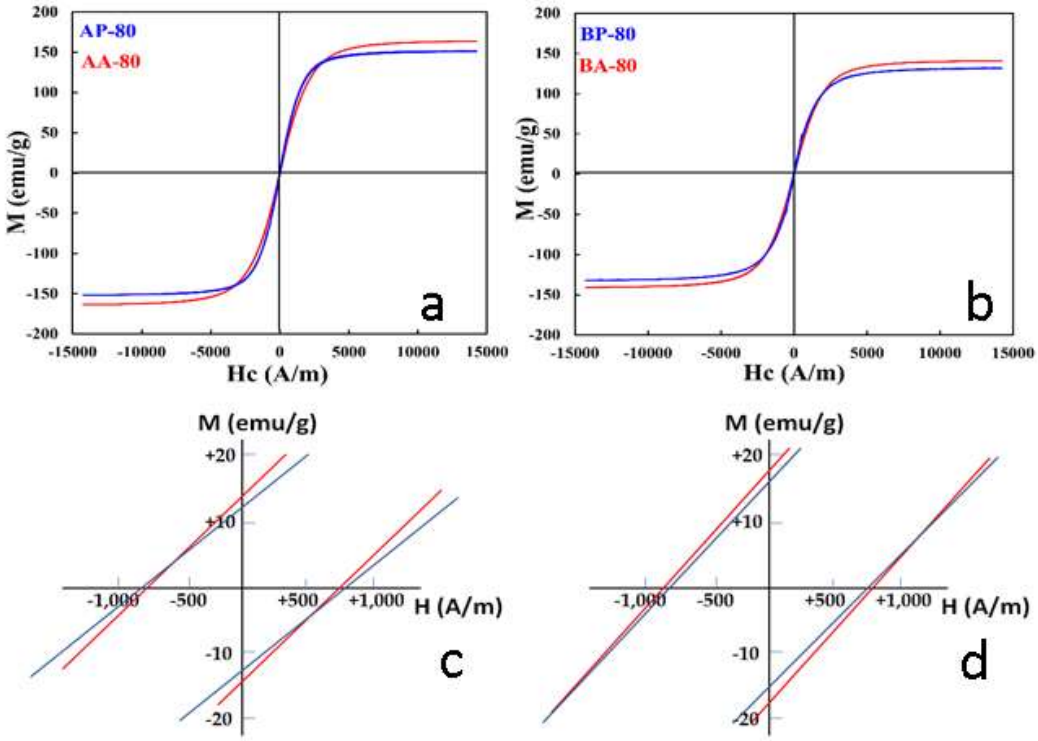

Figure 4.10: Magnetic hysteresis loops of samples: a) AP-80, AA-80, b) BP-80 and BA-80 and insets of the (0,0 region), c). AP-80, AA-80, d) BP-80 and BA-80.

The findings of the most important magnetic characteristics are shown in Table 4.7: coercivity, remanent magnetization (Mr), and saturation magnetization (Ms). Sample microstructure characteristics such as crystallite size, particle shape, structural defects, and so on influence magnetic properties. At room temperature, all of the examined materials exhibit ferromagnetism in the nanocrystalline state and have low coercivity (Hc) values close to 9.67-10.46 Oe equivalent to 770-833 A/m, which is one of the most important criteria for a soft magnetic material; coercivity values less than 1000 A/m are associated with soft magnetic materials [96].

Samples	M_s (emu/g)	M_r (emu/g)	H_c (Oe)	M_r/M_s
AP-80	151.0	13.8	9.67	0.091
AA-80	163.6	11.5	9.86	0.007
BP-80	131.3	18.1	10.20	0.138
BA-80	140.8	17.3	10.46	0.123

Table 4.7: Relevant parameters determined from the magnetic hysteresis loops of samples AP-80, AA-80, BP-80 and BA-80.

The coercivity of bulk compacted specimens (after 80 hours of milling) was measured. The procedure consisted of 30 minutes of vacuum pressing at 600 MPa. The dies have a diameter of 10mm and a thickness of about 3mm. According to the DSC scan analysis, the optimal annealing temperature to promote structural relaxation of the samples without generating crystalline growth is about 300°C. The annealing was performed at two temperatures at 300 and 600°C. Higher temperatures are not recommended because they promote the development of magnetically undesirable intermetallic compounds such as Fe_3B [97]. Table 4.8 displays the corresponding average coercivity values (5 measurements in two samples of the same composition).

Sample	H_c (RT) /Oe	H_c (300°C) / Oe	H_c (600°C) / Oe
$Fe_{80}(NiZr)_8B_{12}$	10.39	9.85	23.53
$Fe_{80}Nb_8B_{12}$	10.61	10.14	25.28

Table 4.8: Coercivity, H_c, of compacted specimens at room temperature (RT) and after annealing (30 minutes) at 300 or 600°C.

Compacted powder milled for 80 hours (AC-80 and BC-80) had slightly higher coercivity values than both alloys produced following milling. We discovered that annealing for 1

hour at 300°C improved coercivity soft behavior (by dropping values by around 5%). It was an expected outcome since DSC scans indicate widespread exothermic processes connected to structural relaxation at low temperatures. Thus, annealing promotes the decrease of dislocation, vacancies, and other mechanically alloyed induced specimen defects [98]. Similarly, annealing at 600°C enhances coercivity and gives the compacted material a soft-hard characteristic. This phenomenon is caused by crystallization at temperatures above 350 °C (detected as exothermic peaks in DSC scans). This effect is explained by crystallization at temperatures above 350 °C (detected as exothermic peaks in DSC scans). The trend of the results as a function of annealing temperature is the same as that obtained in prior studies with specimens of comparable composition [99].

CHAPTER 5

Production and Analysis of $FeCoNi(B_{0,5}Si_{0,5})$

5.1 Introduction

High-entropy alloys (HEAs) are a new type of metal alloy [13]. It was characterized as alloys made of five or more metallic elements, with each elemental concentration ranging from 5 to 35 at.%. HEAs with Fe, Co, and Ni typically form a single body-centered cubic (BCC) solid solution, a single face-centered cubic (FCC) solid solution, or a duplex (FCC + BCC). Some additional HEAs can have an amorphous form. HEAs were thought to be extremely promising materials for soft magnetic and outstanding mechanical qualities such as hardness and wear resistance. Even at low temperatures, the entropy dominates the mixing reaction resulting to HEAs in the mechanical alloying process, which significantly reduces the free Gibbs energy ($\Delta G_{mix} = \Delta H_{mix} - T\ \Delta S_{mix)}$. In this chapter, $FeCoNi(B_{0,5}Si_{0,5})$ HEA was synthesized using mechanical alloying (MA) to produce the final milled powder and a combination of MA and SPS (Spark plasma sintering) to produce the bulk alloys. The mechanical alloying method is the same as described in the previous two chapters. Annealing of the final milled powder was performed at 650 °C. The Spark Plasma Sintering process was performed at two different temperatures. To begin with, a consolidation at a high temperature of 1000°C, using a heating rate of 50°C/min, under a pressure of 50 MPa, was applied in the synthesis. In order to preserve the nanostructured powder and the high density of crystallographic flaws provided by the mechanical alloying, consolidation was carried out at a relatively lower temperature of 750°C. Thus, in this work, we discuss the microstructure, morphology, thermal stability, and magnetic behaviors of powders, as well as the microstructure, thermal, magnetic, and mechanical characteristics of bulk specimens. The process that has been followed for the synthesis of the alloy $FeCoNi(B_{0,5}Si_{0,5})$ HEA is summarized in Figure 5.1:

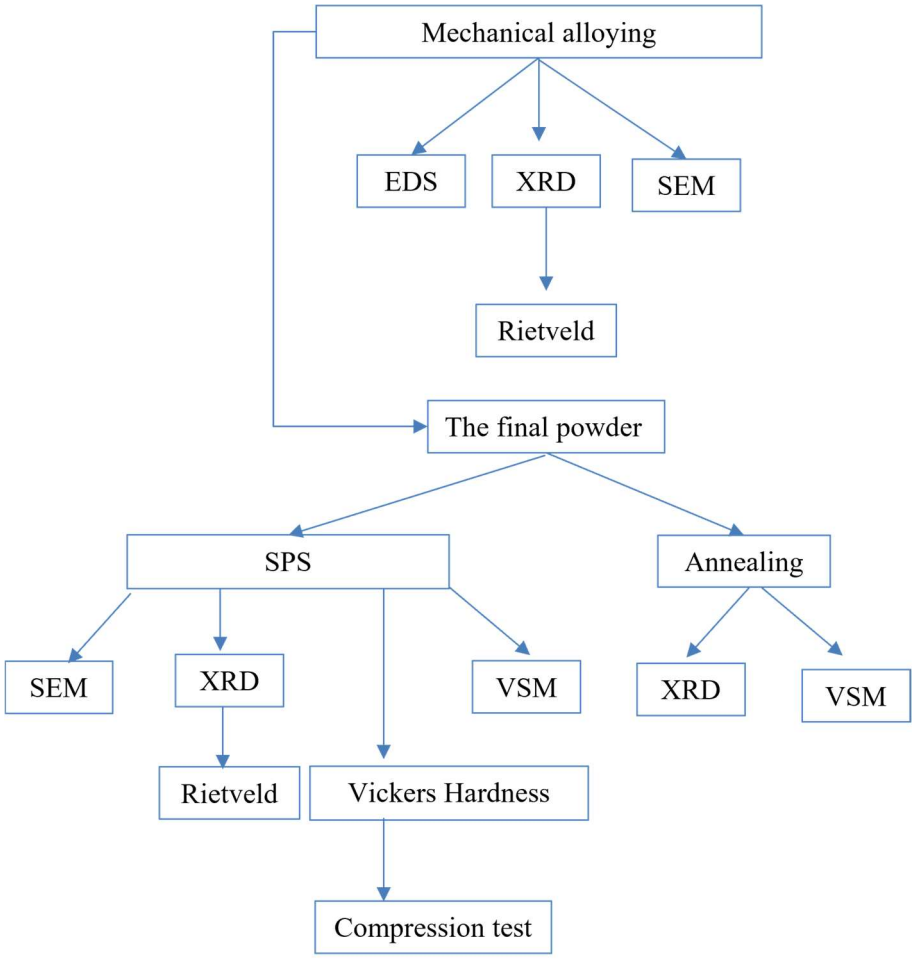

Figure 5.1: Process diagram for synthesis and characterization of FeCoNi($B_{0,5}Si_{0,5}$) HEA alloy.

5.2 Mechanical alloying

5.2.1 XRD Analysis

This section examines the sample composed of powdered iron (25% at.), nickel (25% at.), cobalt (25% at.), silicon (12,5% at.), and boron (12,5% at.). Energy Dispersive X-Ray Spectroscopy (EDS) has confirmed that the contamination from the vial materials is less than 1% atomic. Figure 5.2 illustrates the diffraction peaks of precursors as well as the presence of four pure elements' characteristic peaks: BCC-Fe, FCC-Ni, HCP-Co, FCC-Co, and FCC-Si. In the premixed powder, the HCP and FCC-Co structures coexist. The characteristic peaks for boron are not observed because amorphous boron powder was used in the present work. However, we can only observe the Si's first two reflection peaks. Table 5.1 displays the reflections of each phase.

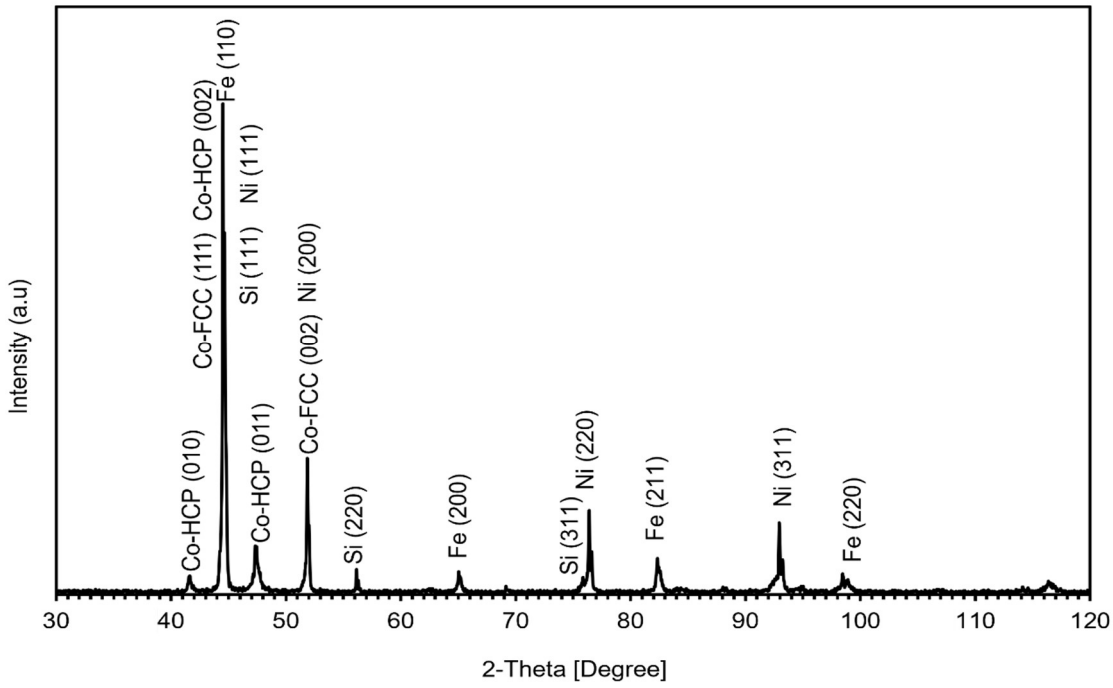

Figure 5.2: FeCoNi($B_{0,5}Si_{0,5}$) powder X-ray diffraction patterns before milling.

Phases	Reflexions			
Fe-BCC	(110)	(200)	(211)	(220)
Co-FCC	(111)	(002)		
Co-HCP	(010)	(002)	(011)	
Ni-FCC	(111)	(200)	(220)	(311)
Si-FCC	(111)	(220)	(311)	

Table 5.1: Reflections present in the diffractogram of the sample FeCoNi($B_{0,5}Si_{0,5}$) and corresponding phases.

5.2.2 Rietveld Analysis

Figure 5.3 depicts the XRD pattern of FeCoNi($B_{0,5}Si_{0,5}$) powder before and after milling at various times. The best refining results are provided in Table 5.2.

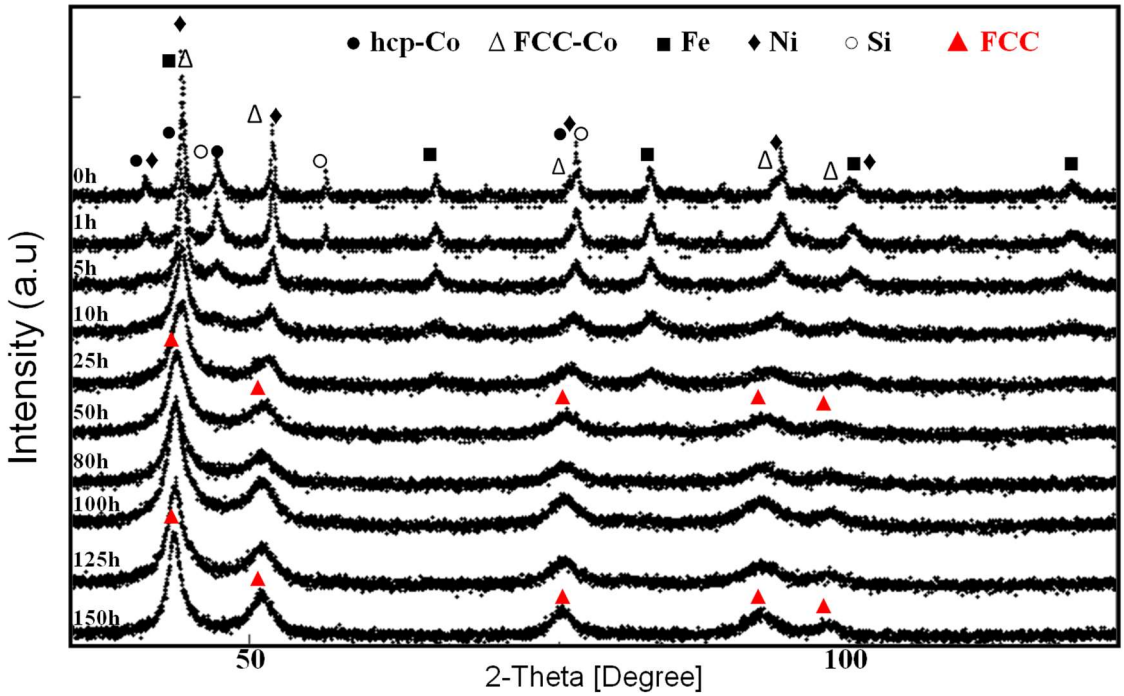

Figure 5.3: X-ray diffraction patterns of $FeCoNiB_{0.5}Si_{0.5}$ powders as a function of mechanical alloying time.

Milling time (h)	R_{wp}	R_{exp}	GoF(R_{wp}/R_{exp})
0	4.01	3.46	1.16
1	3.39	2.95	1.14
5	2.23	2.10	1.06
10	2.15	1.91	1.12
25	2.13	1.96	1.08
50	2.00	1.84	1.08
100	1.52	1.34	1.13
150	2.09	1.94	1.07

Table 5.2: Goodness of fit and Fit parameters during milling.

The Bragg diffraction peaks corresponding to the pure elements are shown in the X-ray diffraction diagram of the initial powder (figure 5.4.a): Fe with structure BCC and crystalline lattice parameter a = 2.866(7) Å; Ni with structure fcc and crystal parameter a = 3.523(0) Å , Co with fcc structure and crystal parameter a = 3.544(2) Å , Co with hcp structure and crystal parameter a= 2.507(1) Å and c = 4.068(5) Å and silicon with fcc structure and crystal parameter a= 5.430(3) Å. . After 5 hours of milling (Figure 5.4.b), the intensity of the peaks diminished substantially. The FCC-Si and FCC-Co diffraction peaks are detected to vanish. During milling, several authors observed an allotropic

change of Co from FCC to HCP structure [100, 101]. Furthermore, when mechanical energy is applied, the FCC-Co becomes unstable [102]. After 25 h the HCP-Co peaks completely vanish and the most intense diffraction peak of the BCC-iron phase became asymmetric. The peak's asymmetry is caused by the progressive disappearance of the BCC phase and the appearance of the FCC solid solution. The shift of the Fe peaks toward smaller angles (compared to the reference unmilled powder - 0h) indicates an increase in the lattice parameter, which can be attributed to the lattice expansion caused by the diffusion of B, Si, Co, and Ni into the Iron matrix, resulting in the cohabitation of BCC and FCC solid solution after 25 h. (see Figure 5.4.c). The FCC phase appears as a result of the diffusion of Ni, Si and Co into the Ni matrix and the interdiffusion between Ni and Fe, with the FCC phase having a higher lattice parameter than the FCC Ni matrix. As the milling time approaches 150 hours (Figure 5.4.d), only the peaks indicating an FCC solid solution phase are visible, while the BCC iron peak disappears. As a result, the solid solution's structure can be described as supersaturated solid solution.

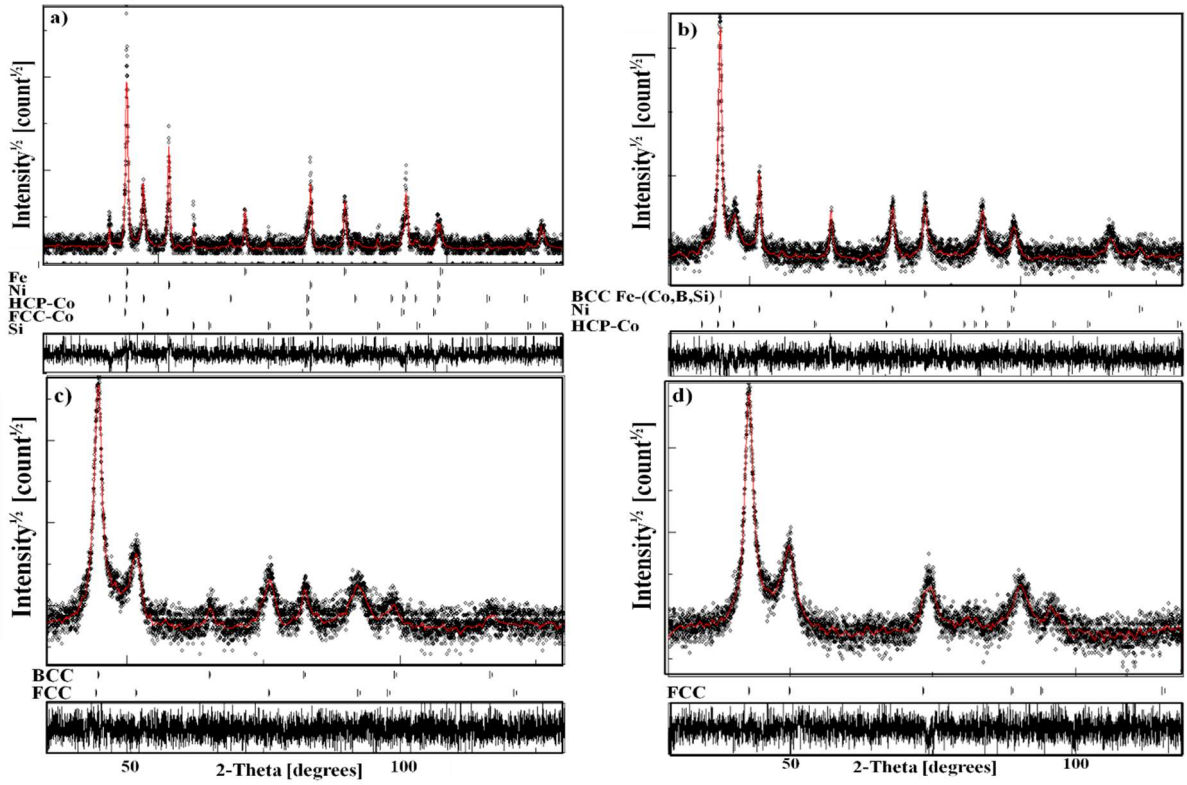

Figure 5.4: Rietveld refinement of the XRD pattern of the FeCoNi($B_{0,5}Si_{0,5}$) powder: (a) before milling (b) 5h, (c) 25h, (d) 150h.

The variation of the lattice parameter as a function of milling time for $FeCoNi(B_{0,5}Si_{0,5})$ alloy is shown in Table 5.3. Because of the inclusion of B (R_B=0.82 Å) atoms in the interstitial sites and the substitution of Fe atoms by Si (R_{Si}=1.15 Å), Co (R_{Co}=1.25 Å), and Ni (R_{Ni}=1.24 Å), the lattice parameter of the BCC phase rises with increasing milling time. The increased FCC lattice parameter is caused by atom substitution in the Ni matrix and inter-diffusion between the Fe and Ni atoms.

Samples	Phases	Lattice parameter (Å)
0h	BCC-Fe	2.866(7)
	FCC-Ni	3.523(0)
	HCP-Co	2.507(1)
		c = 4.068(5)
	FCC-Co	3.544(2)
	FCC-Si	5.430(3)
5h	BCC-Fe(Co,B,Si)	2.868(1)
	FCC-Ni	3.525(3)
	Hcp-Co	2.512(6)
		c = 4.079(6)
25h	BCC Fe-Co-Ni(B,Si)	2.869(2)
	FCC Fe-Co-Ni(B,Si)	3.541(5)
50h	FCC Fe-Co-Ni(B,Si)	3.601(2)
150h	FCC Fe-Co-Ni(B,Si)	3.630(8)

Table 5.3: Lattice parameter during milling.

The variation of the crystallite size and microstrain as a function of milling time for $FeCoNi(B_{0,5}Si_{0,5})$ alloy during the first 10h is shown in Figure 5.5. In the early stages of milling, the crystallite size of all elements, as well as the newly generated BCC-Fe(Co,B,Si) supersaturated solid solution, drops significantly with increasing milling time. Boron atom segregation at grain borders inhibited grain development in the BCC phase [103]. As a result, boron dissolution significantly reduces crystallite size. Figure 5.4.b depicts the evolution of internal microstrains during milling. Internal strain

increases as milling time increases. Micro-stress in crystallites can occur from a multiplicity of factors, including vacancies, dislocation multiplication, and other defects [104]. The BCC phase has a crystal size of 14 nm and a lattice strain of 0.3% after 10 hours. Internal microstrain is growing due to a size mismatch between the starting components, a rise in grain boundary fraction, and a high dislocation density caused by severe plastic deformation.

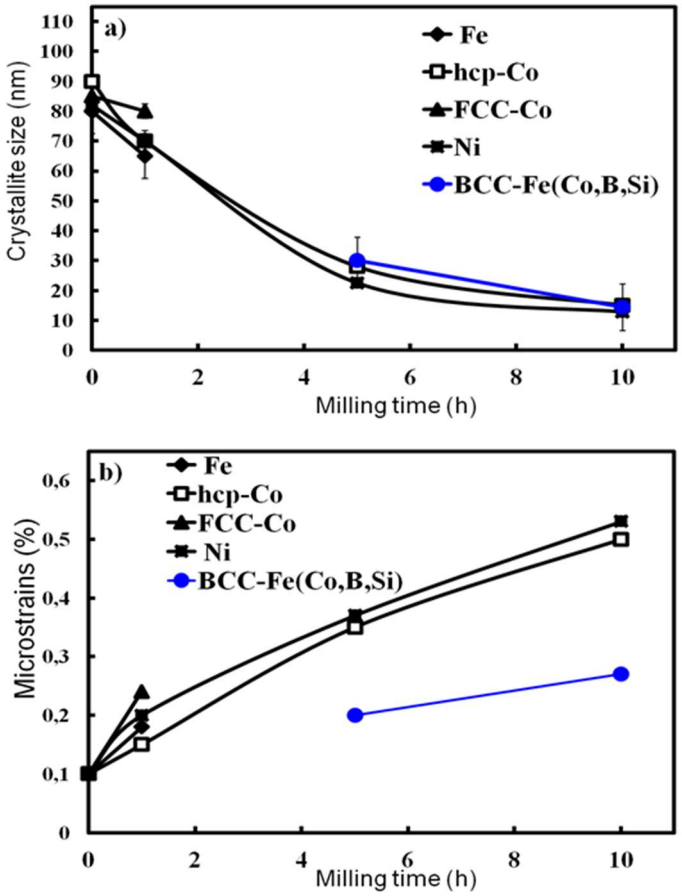

Figure 5.5: Evolution of the microstructure parameters of the Fe, FCC-Co, HCP-Co, Ni and -Fe (Co,B,Si) as a function of milling time.

Figure 5.6 depicts the evolution of crystallite size and lattice strain in the produced FCC Fe-Co-Ni-B-Si supersaturated solid solution as a function of milling time. When the FCC solid solution cohabits with a BCC Fe-Co-Ni-(B,Si) solid solution (after 25 h), the crystallite size is 11 nm with a microstrain of 0.3%. After 50 hours, the FCC solid solution retains a single phase with a crystallite size of about 11 nm and a microstrain of 0.4%. The lattice strain of the FCC phase rises with milling time. The powder has a lattice strain of 0.7% after being milled for 150 hours. The crystallite size appears to drop slowly but steadily with increasing milling time, eventually reaching 10 nm at the end of the milling.

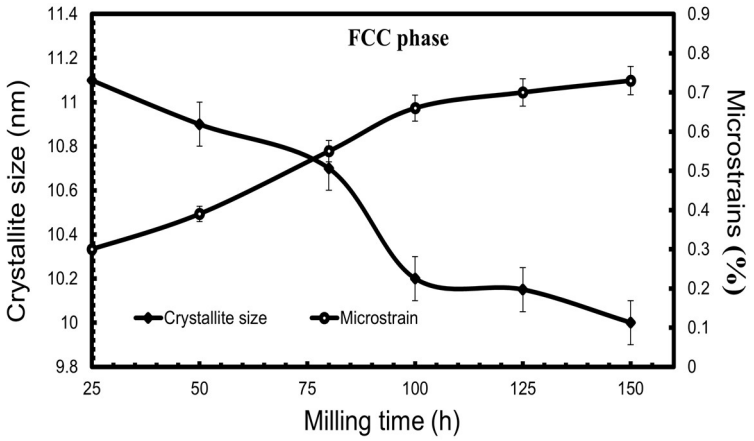

Figure 5.6: Dependence of the microstructure parameters of the FCC Fe-Co-Ni-(B,Si) as a function of the milling time.

The dislocation density is calculated the same as in the chapter 3, taking into consideration the corresponding Burgers vector for the FCC structure. Figure 5.7 displayed the calculated dislocation densities the MA Fe-Co-Ni-(B,Si). With increasing milling time from 25h to 100 h, we can see a significant rise in ρ from around $0.81 \times 10^{16}/m^2$ to $0.96 \times 10^{16}/m^2$. After 125 hours of milling, the ρ slowly increases till the end of the milling, reaching $0.99 \times 10^{16}/m^2$.

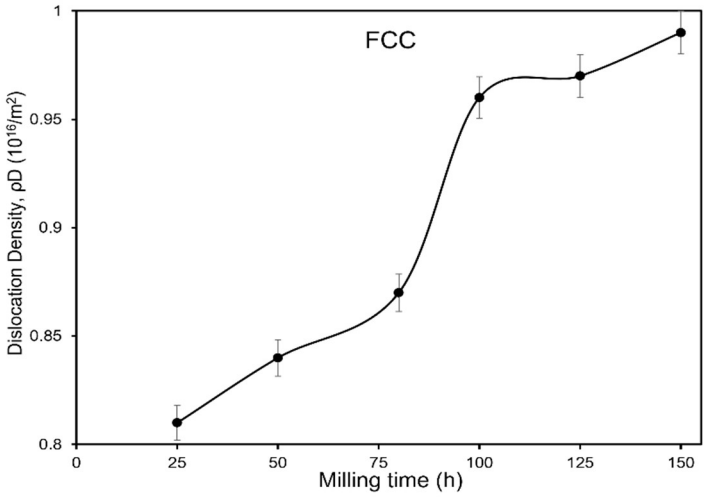

Figure 5.7: Evolution of the dislocation density of the sample's main phase of the MA Fe-Co-Ni-(B,Si) during milling time.

5.2.3 Morphology

Figure 5.6 depicts the morphological development of alloyed powders at various phases of milling. The unmilled particles are simply combined, with no discernible deformation

(Figure 5.8.a). Due to the strong plastic deformation and sequential force of the ball-powder-ball impacts into the particles, milling for 5 hours (Figure 5.8.b) entirely destroys the original shape. As a result, the cold-welding effect is dominating. This promotes atom diffusion, which leads to the alloying process. After up to 25 hours of grinding, fragmented particles with more regular sizes and flattened particles are found [105]. (See Figure 5.8.c). After 50 hours of milling, the most of the particles were rounded, and the powder's homogeneity is noticeable. As a result, a balance between fracture and cold welding is achieved [106] (see figure 5.6.d). The particles got smaller (Figure 5.8.e) and had a finer structure at the end of the milling process as the milling time increased (Figure 5.8.f).

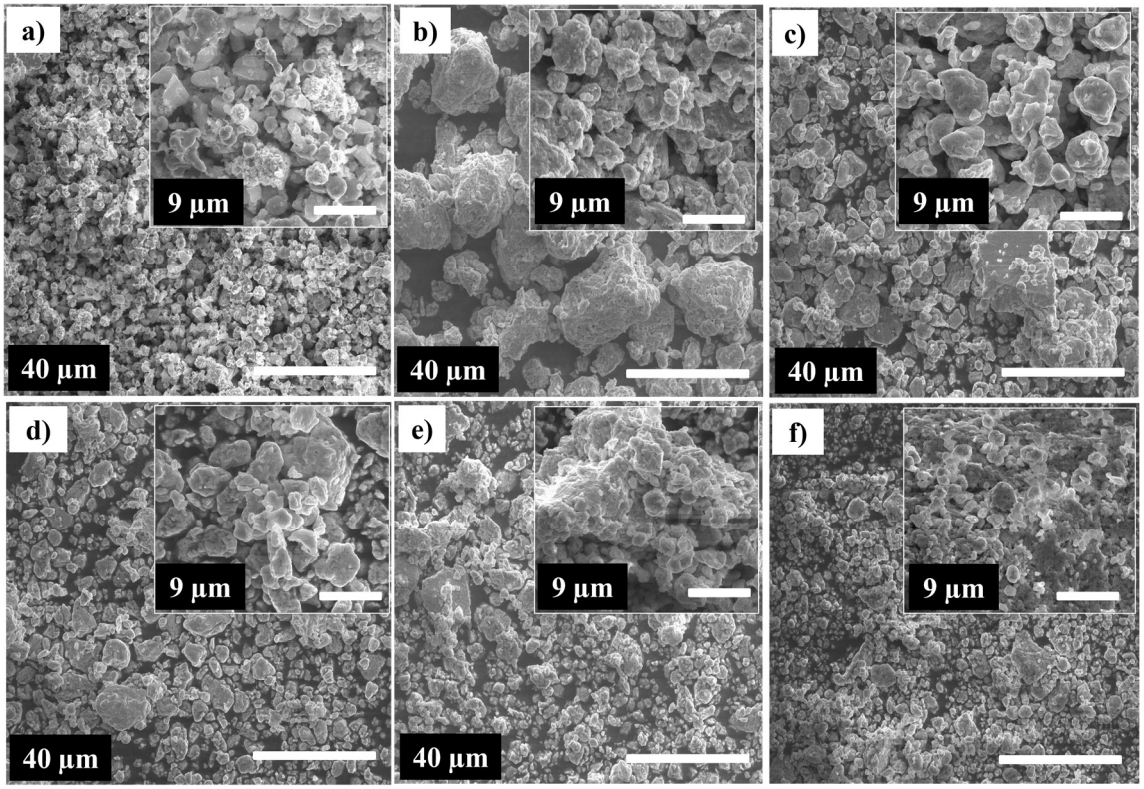

Figure 5.8: Scanning electron micrographs of mechanically milled powders: (a) 0h, (b) 5h, (c) 25h, (d) 50h, (e) 100h and (f) 150h.

5.3 Thermal treatments

To investigate the influence of heating on structural and magnetic characterization, the 150-h milled high-entropy alloy powder $FeCoNiB_{0.5}Si_{0.5}$ was annealed for 1 hour at 650 °C in an argon atmosphere. Figure 5.9 illustrates the XRD patterns before and after annealing. While a fraction of the FCC solid solution is retained, the peak intensity rises owing to crystallite size growth during heating. After annealing, various new crystalline phases appear, including BCC-$(Fe,Ni)_{23}B_6$ (Ref. Code: 04-001-5987), FCC-$Ni_{17}Si_3$ (Ref. Code: 03-065-6491), and BCC-Fe_3Si (Ref. Code: 04-004-6643). The metastable structural transition following annealing results in these stable equilibrium phases.

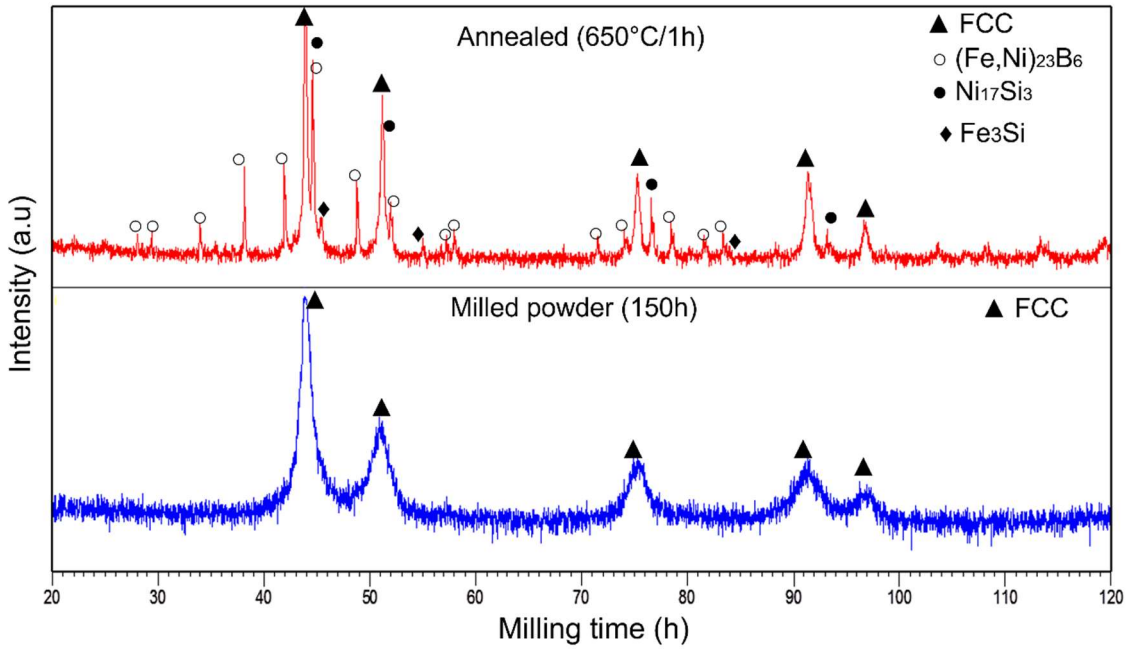

Figure 5.9: X-ray diffraction patterns of MA $FeCoNiB_{0.5}Si_{0.5}$ powders for 150h of milling and after annealing at 650°C for 1 hour.

5.4 Consolidation by SPS

To make the bulk high-entropy alloy $FeCoNiB_{0.5}Si_{0.5}$, the powder was sintered by SPS at two different temperatures, the lower temperature process at 750°C and the higher temperature process at 1000°C. The applied pressure was 50MPa under vacuum. Then the samples were mechanically polished up to a colloidal silica suspension of 50nm. The super-finishing stage was increased to 20 minutes. Figure 5.10 depicts the piston displacement as a function of temperature during powder sintering for both tests. Around 500°C, the powder begins to sinter. Sintering occurs at 850°C. According to Archimedes

procedure, the relative densities of the produced HEA specimens sintered at 750°C and 1000°C are 5806 kg/m^3 and 5938 kg/m^3, respectively. This suggests that densification is not complete at 750°C and that porosities of around 2% are present. The theoretical densities of SPS-750°C -50MPa and SPS-1000°C -50MPa are 5930 kg/m^3 and 5940 kg/m^3, respectively.

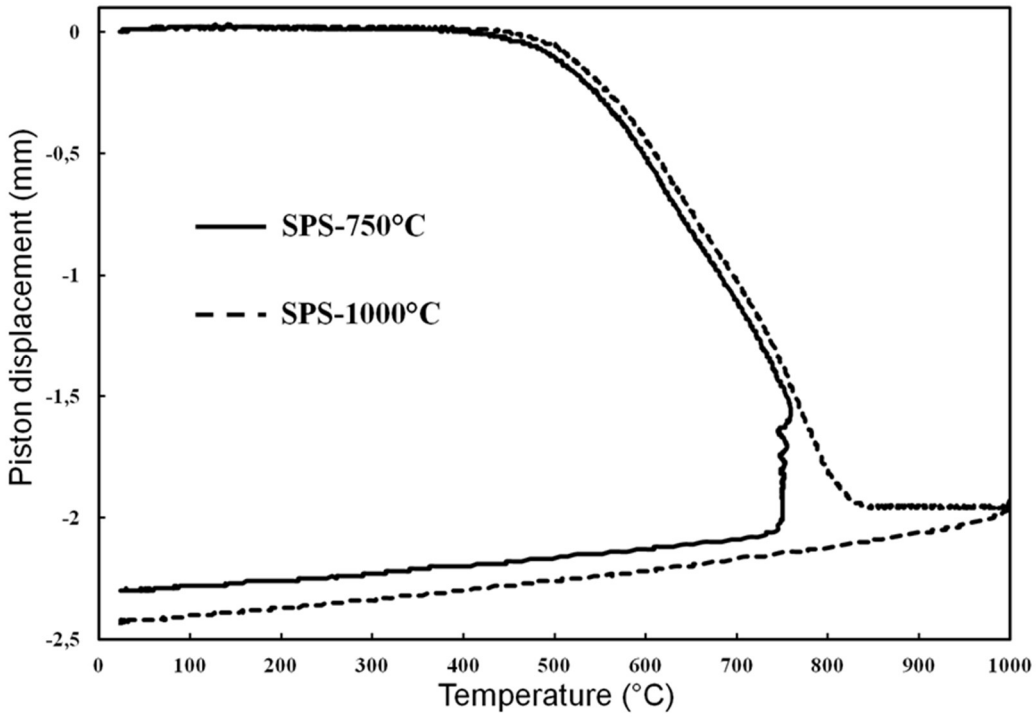

Figure 5.10: Piston displacement as a function of the temperature during the sintering of the powders.

5.4.1 XRD Analysis

The figure 5.11 depicts the XRD pattern of samples sintered by SPS at 750°C and 1000°C at a pressure of 50MPa. Sintered powder at 750°C results in the appearance of the intermetallic phase $(Fe,Ni)_{23}B_6$ (40.9%), this sample has a density of 97.76% and porosity of about 2.32%. Whereas sintered powder at 1000°C results in the appearance of the $FeCo_2B$ (13.2%) and increase in density to 99.33%. The crystallite size of the FCC phase in each sintered sample was calculated by the Rietveld Analysis. The average particle size of the FCC phase in sample sintered at 750°C and 1000°C is found to be equal to 54.5 nm and > 100 nm respectively.

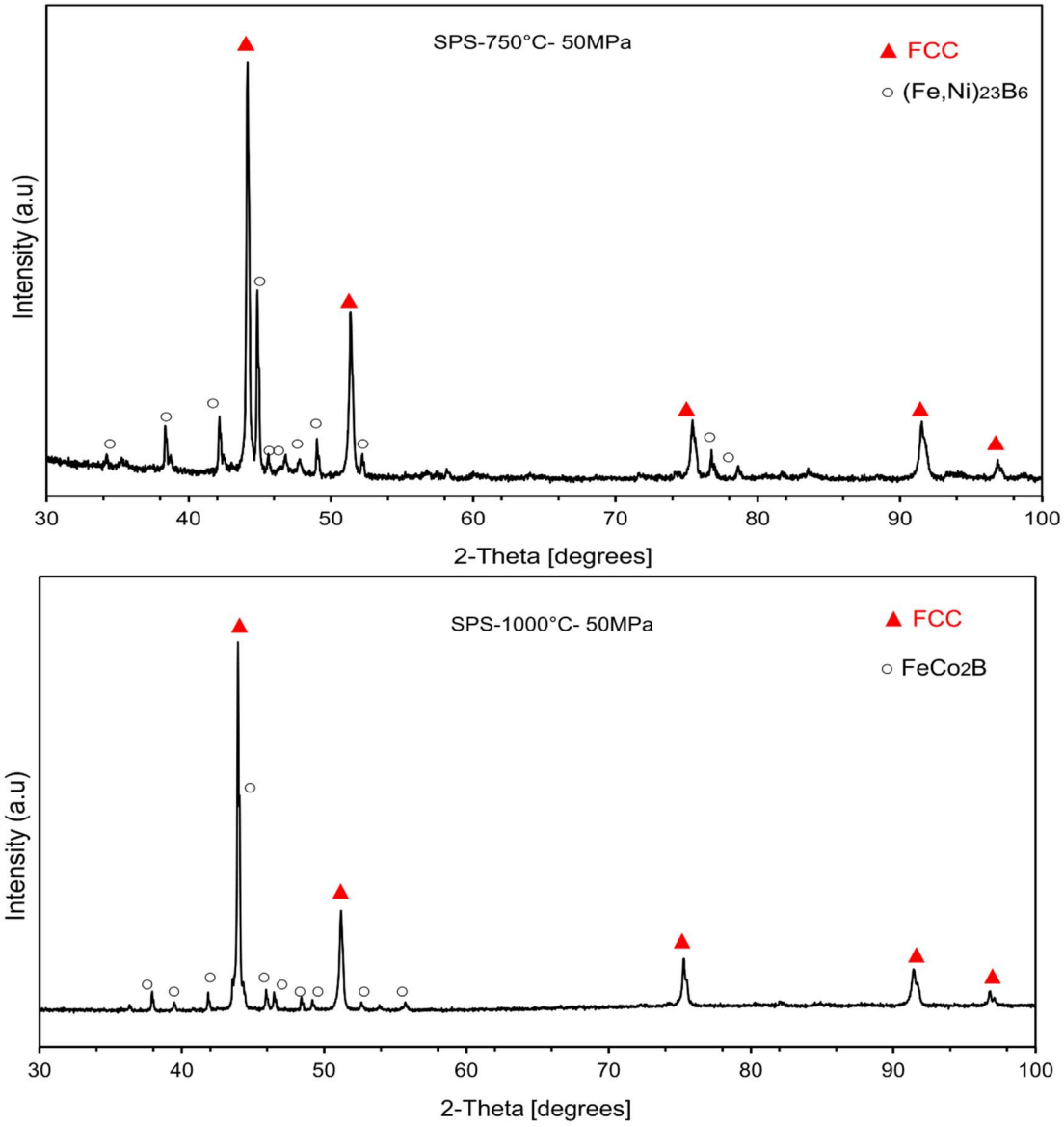

Figure 5.11: X-ray diffraction pattern and the Scanning electron micrographs of the HEA after SPS.

5.4.2 Morphology

SEM microstructural analysis clearly demonstrates the effect of SPS temperatures on the microstructure of sintered samples (Figure 5.12). High temperatures, such as 1000°C, produce a significant increase in grain size. Table 5.4. shows the corresponding energy-dispersive X-ray spectra (EDS) of the two sintered bulks. Because EDS cannot measure boron, it is not included in the table. The sample's topography is shown by the alternate dark/light zones. Given the phase ratios shown by the XRD patterns, the bright zone is most likely the FCC phase.

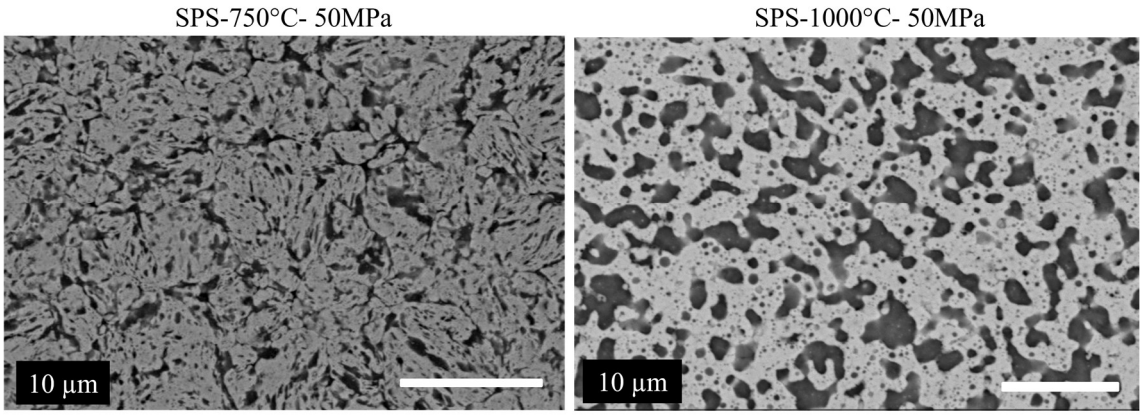

Figure 5.12: Scanning electron micrographs of the $FeCoNiB_{0.5}Si_{0.5}$ alloy after SPS.

Element	Fe	Co	Ni	Si
SPS-1000°C	25.58	25.46	25.11	23.85
SPS-750°C	25.39	25.38	25.23	24.00

Table 5.4: Chemical composition (in at. %) of the specimens given by EDS.

5.5 Magnetic Analysis

The hysteresis curve of the 150h milled $FeCoNiB_{0.5}Si_{0.5}$ powder before annealing, after annealing at 650°C for 1 h, and following Spark plasma sintering at 750°C and 1000°C is shown in Figure 5.13. Table 5.5 shows the values of saturation magnetisation (Ms), remanence to saturation ratio (Mr/Ms), and coercivity (Hc).

The saturation magnetization of the annealed sample is greater and the coercivity is lower than that of the as-milled powder. The structures of the BCC phases generated during annealing can explain the rise in saturation magnetisation. In fact, the saturation magnetisation of the BCC structure is greater than that of the FCC structure [107,108]. The reduction of coercivity following heat treatment is determined by the increase in crystallite size, grain size, and structural strain [109]. The saturation ratio falls from 0.034 after milling to 0.025 following annealing and finally to 0.012 after SPS. This drop might be attributed to the release of microstrains and domain wall energy during temperature elevation. The saturation ratio is also affected by the formation of phases after annealing and SPS sintering. Based on measurements of high saturation magnetisation Ms and low coercivity Hc, it is possible to deduce that the heat treatment at 650°C softens the HEAs magnetically. When compared to conventionally annealed samples, SPS specimens have

higher coercive field values and lower saturation ration values. Furthermore, the consolidated samples exhibit lower coercivity, lower saturation ratio, and grater saturation magnetization values than the as-milled powders from which they are formed.

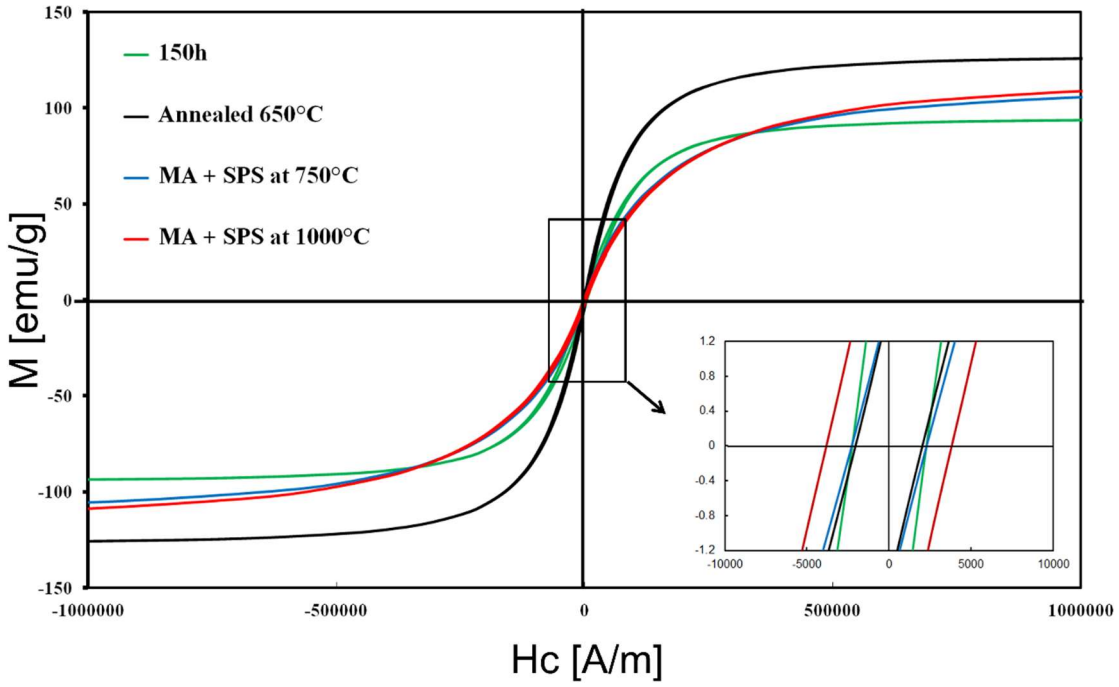

Figure 5.13: Magnetic hysteresis plots of 150h milled $FeCoNiB_{0.5}Si_{0.5}$ powders after annealing, MA+SPS at 750°C and MA+SPS at 1000°C.

Samples	M_s ($emug^{-1}$)	M_r ($emug^{-1}$)	H_c(Oe)	M_r/ M_s
As-milled	94.31	3.27	49.07	0.034
Annealed at 650°C	127.30	3.19	29.57	0.025
MA + SPS at 750°C	110.91	1.41	25.06	0.012
MA + SPS at 1000°C	115.84	1.47	27.90	0.012

Table 5.5: Magnetic properties of the milled $FeCoNiB_{0.5}Si_{0.5}$ HEA powder before and after annealing.

5.6 Mechanical properties

After SPS consolidation, room-temperature compressive testing and hardness measurements were performed. Table 5.6 displays the results. The compressive strength (max) drops by around 12% as the SPS temperature rises, whereas the yield strength (σ_y) decreases by 20%. During the compression test, the sample sintered at 750°C produced crack sounds, this suggests that the final strength of 1062 MPa is overestimated. The

sample sintered at 750°C is much harder (518 HV) than the sample sintered at 1000°C (176 HV). The Vickers hardness indentation method is destructive; it induces sample surface deformation and stress concentration at the indent point, which is frequently referred to as the surface deformation zone. This can cause a change in the sample's mechanical characteristics. Deformation piles up and main shear bands created by compressive forces under the indent cause short increases in hardness surrounding the indented area in most materials. The high hardness value produced after SPS at 750°C is determined by dislocation strengthening and ultrafine grains. As demonstrated by SEM observation of SPS-consolidated specimens, increasing temperature promotes an increase in grain size. According to the Hall-Petch relationship, increasing grain size results in a significant drop in compression yield strength [110].

Alloy	Process	σ_y (MPa)	σ_{max} (MPa)	Hardness (HV)
$FeCoNiB_{0.5}Si_{0.5}$	MA + SPS at 1000°C	722	926	176 (1.27)
$FeCoNiB_{0.5}Si_{0.5}$	MA + SPS at 750°C	913	1062	518 (14.78)

Table 5.6: Mechanical properties: compressive strength (σ_{max}), yield strength (σ_y) and Vickers hardness.

Figure 5.14 illustrates the fractographic pictures obtained after the compressive strength testing alloy was consolidated at two different temperatures. As illustrated in Figure 5.12.a, the samples consolidated by SPS at 750°C reveal fractures, which explain the intergranular fracture found with a dimpled structure all over the surface, indicating that the fracture mechanism is brittle fracture. The plastic-slipping plane seen with the sample sintered by SPS at 1000°C (Figure 5.12.b) revealed that the mode of fracture is a ductile fracture.

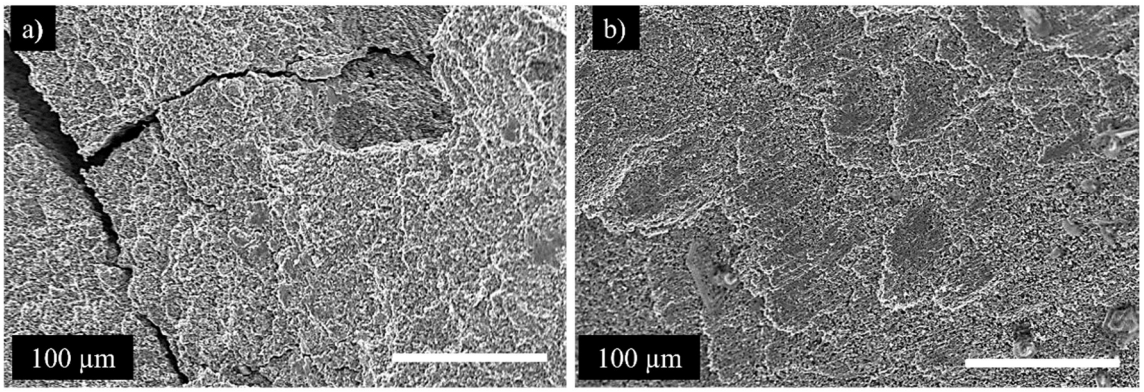

Figure 5.14: Fractography by SEM of the fracture surfaces of the specimens consolidated by SPS, a) SPS at 750°C and b) SPS at 1000°C.

CHAPTER 6

Production and Analysis of $Fe_{65}Ni_{28}Mn_7$

6.1 Introduction

Maraging steels (Fe-Ni-Mn) are a type of low carbon ultra-high strength steel that is made by precisely optimizing the quantities of nickel and manganese in the completed product. Depending on how these two important constituents vary, it is possible to improve a variety of critical qualities of the completed product, including greater hardness properties. The $Fe_{65}Ni_{28}Mn_7$ (at. %) alloy was made in this chapter first by mechanical alloying (MA) in the high-energy planetary ball mill P7. Second by Arc melting from individual elements (99.98% pure Fe, 99.98% pure Ni, and 99.98% pure Mn) using conventional argon arc melting. Third, the final MA powder was consolidated by spark plasma sintering at different temperatures and pressures to produce a bulk material. As discussed in previous chapters, for mechanical alloying, the powder X-ray diffraction patterns at various milling times are displayed with the diffractograms of the indexed precursors to identify all of the phases present prior to milling. Morphological investigations and Rietveld analyses using the Maud program are performed for various milling times. Morphological analyses were also performed on the bulk materials produced by Arc melting and Spark plasma sintering after polishing, and their densities were calculated using the Archimedes' Method. Magnetic investigations were conducted on the final powder acquired by MA as well as the bulk materials obtained by AM and SPS. A mechanical comparison study (compression and Vickers Hardness) was also conducted between the specimen produced by AM and the bulk materials produced by SPS. The process that has been followed for the synthesis of the alloy $Fe_{65}Ni_{28}Mn_7$ (at. %) is summarized in Figure 6.1:

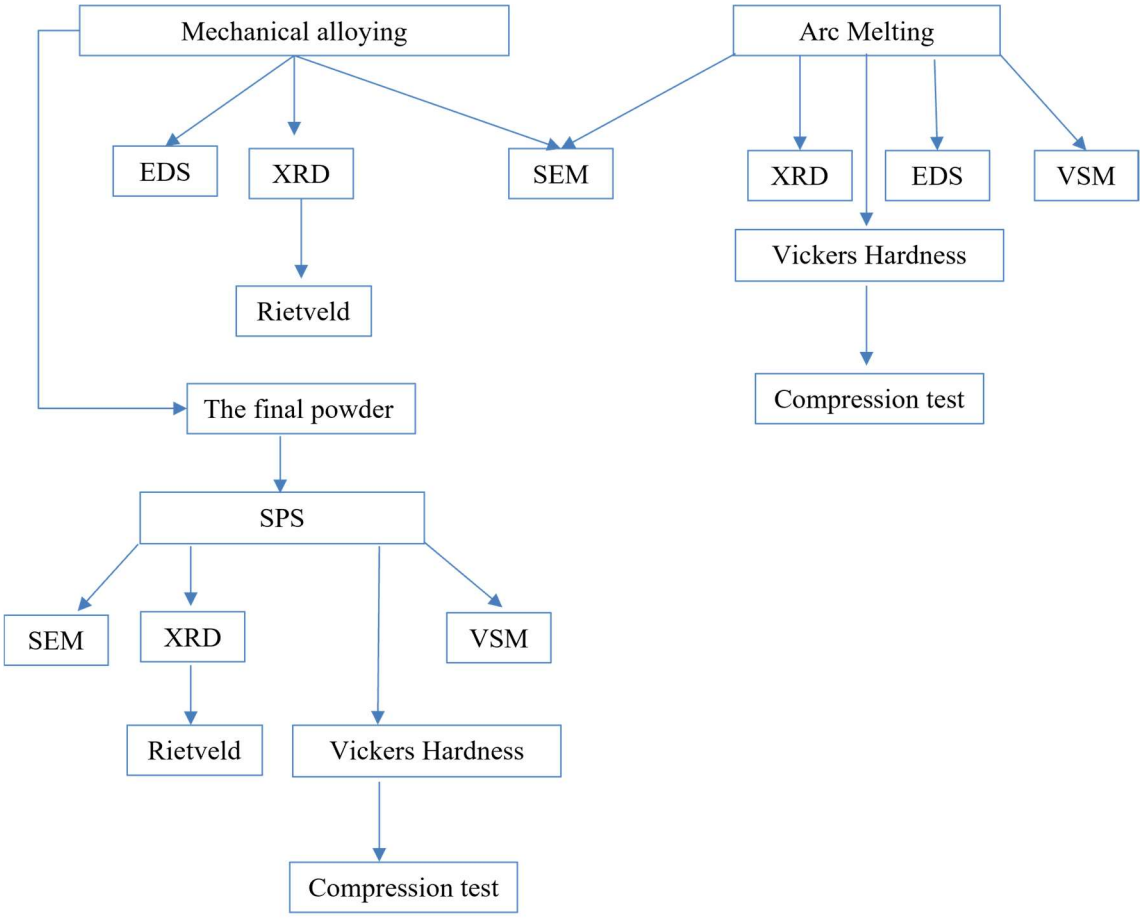

Figure 6.1: Process diagram for synthesis and characterization of $Fe_{65}Ni_{28}Mn_7$ (at. %) alloy.

6.2 Mechanical alloying

6.2.1 XRD Analysis

This section looks at the sample made from powdered iron (65% at.), nickel (28% at.), and manganese (7% at.). Energy Dispersive X-Ray Spectroscopy (EDS) has confirmed that the contamination from the vial materials is less than 1% atomic. Figure 6.2 displays the diffraction peaks of precursors as well as the existence of the characteristic peaks of three pure elements: BCC-Fe, FCC-Ni, and BCC-Mn. The bcc-Fe, which is the majority phase, presents the reflection peaks (110), (200), (211), (220) and (310) corresponding to a body centered cubic (bcc). The reflection peaks (111), (200), (220) and (311) corresponding to a face-centered cubic (fcc) of Ni, which is the second phase with the greatest presence in the diffractogram, can be observed. On the other hand, we can only see the first two reflection peak of the Mn (200) and (211). This is owing to its low atomic

number and lower proportion (7% at.) in relative to Ni and Fe. Table 6.1 shows the reflections of each phase.

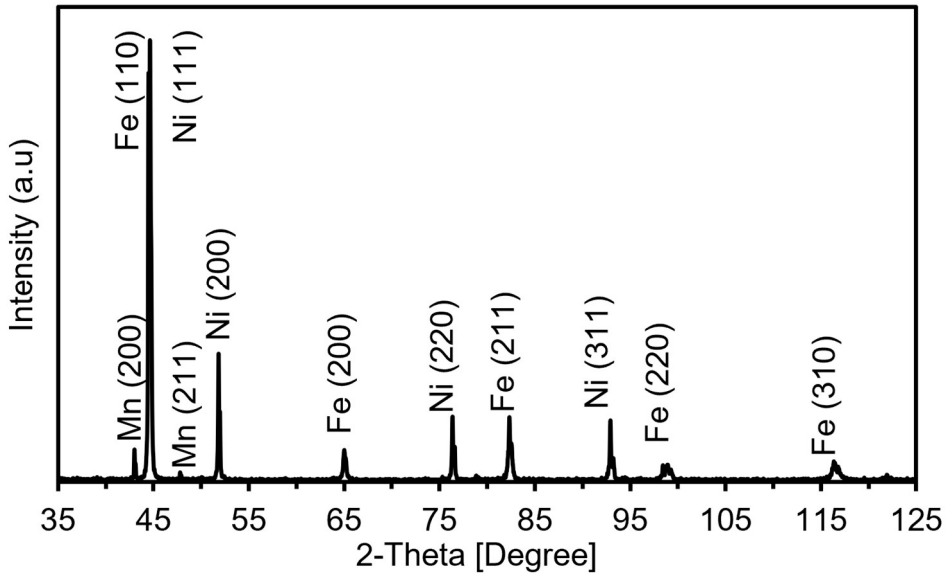

Figure 6.2: $Fe_{65}Ni_{28}Mn_7$ powder X-ray diffraction patterns before milling.

Phases	Reflexions				
BCC-Fe	(110)	(200)	(211)	(220)	(310)
FCC-Ni	(111)	(200)	(220)	(311)	(222)
BCC-Mn	(200)	(211)			

Table 6.1: Reflections present in the diffractogram of the sample $Fe_{65}Ni_{28}Mn_7$ and corresponding phases.

6.2.2 Rietveld Analysis

The XRD pattern of $Fe_{65}Ni_{28}Mn_7$ powder before and after milling at various periods is shown in Figure 6.3. the best refining is achieved and shown in Table 6.2.

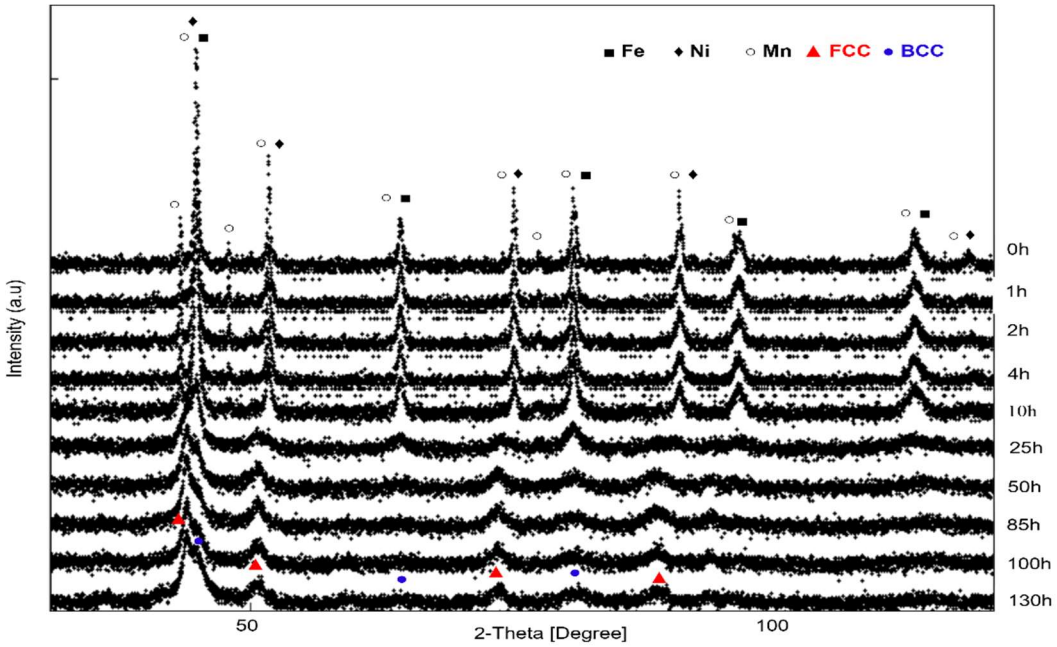

Figure 6.3: $Fe_{65}Ni_{28}Mn_7$ powder X-ray diffraction patterns as a function of milling time.

Milling time (h)	R_{wp}	R_{exp}	GoF(R_{wp}/R_{exp})
0	3.74	3.11	1.20
1	3.65	3.45	1.05
2	3.44	3.29	1.04
4	3.45	3.29	1.04
10	2.80	2.47	1.13
25	2.69	2.52	1.06
50	2.82	2.58	1.09
85	2.85	2.55	1.11
100	2.73	2.55	1.07
130	2.72	2.47	1.09

Table 6.2: The residual parameters and GoF values of the compounds identified using Rietveld analysis.

The Bragg diffraction peaks corresponding to the pure elements are shown in the X-ray diffraction diagram of the initial powder (figure 6.4.a): Fe with structure BCC and crystal parameter a = 2.866(6) Å; Ni with structure FCC and crystal parameter a = 3.525(1) Å and Mn with BCC structure and crystal parameter a = 8.912(5) Å. Milling for up to 10 hours leads in a little broadening of the peaks and a considerable decrease in their

intensity, owing to refined grain and crystallite size as well as increasing lattice strain [111]. As the milling duration increased, the Mn peak decreased. After 25 hours of milling, the Mn peaks seemed to vanish (Figure 6.4.b). The diffraction peak's disappearance might be attributed to the creation of a solid solution, lattice distortion, or crystal refinement. At this stage, interdiffusion of Fe and Ni atoms occurs resulting in the coexisting of FCC phase and BCC phase. The BCC phase is the most prominent. By extending the milling time to 50 hours, part of the metastable BCC phase was changed into the FCC phase (Figure 6.4.c). This might be explained by the diffusion of Fe and Mn into the Ni matrix. A phase percentage of about 65% and 35% was determined for the BCC and FCC, respectively. As a result, at the milling's end, the FCC phase had superseded the BCC phase as the dominant one (Figure 6.4.d).

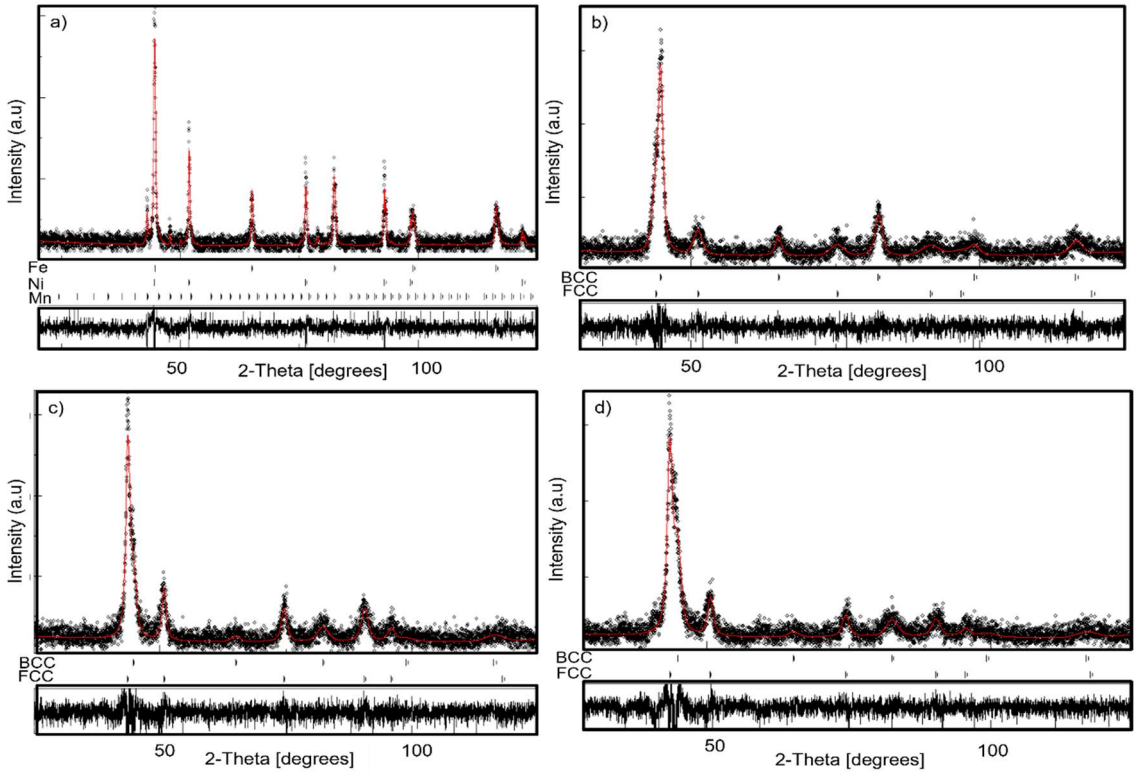

Figure 6.4: Rietveld refinement of the XRD pattern of the $Fe_{65}Ni_{28}Mn_7$ powder: (a) Before milling, (b) 25h, (c) 50h, (d) 130h.

The crystallographic parameters were extracted using the Rietveld refinement method, the evolution of the lattice parameter of the Fe and Ni is shown in the figure 6.5. The introduction of Mn atoms into the vacant sites of pure Fe (R_{Fe} = 1.24 Å), the alloy's primary phase, raises the lattice parameter relatively slightly during the first 10 hours of milling. After 25 hours of milling, the Fe and Ni pics had vanished and BCC and FCC phases were formed with lattice parameters equals to a=2.867(0) Å and a=3.568(0) Å,

respectively. The lattice parameters of the BCC and FCC at the end of milling are a=2.867(5) Å and a=3.591(2) Å, respectively, as a result of the interdiffusion of Fe and Ni atoms.

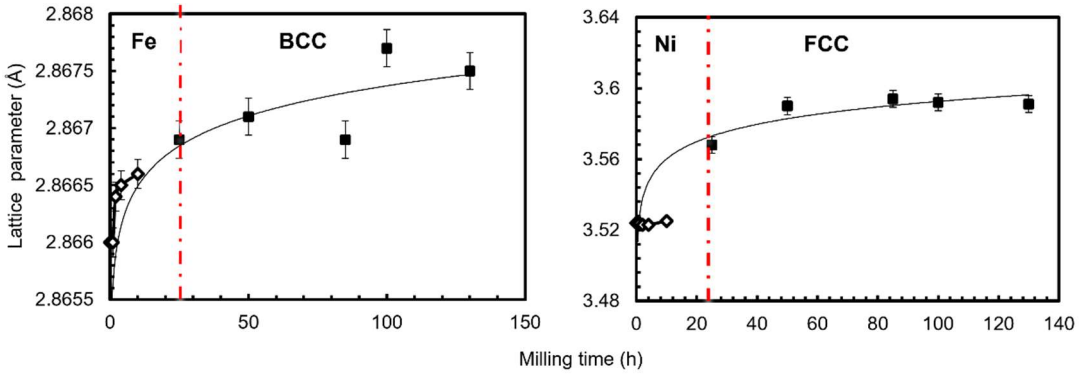

Figure 6.5: The evolution of the principal phases lattice parameters during MA of $Fe_{65}Ni_{28}Mn_7$.

The evolution of the average crystallite size, <L>, and the microstrain rate, $< \sigma^2 >^{\frac{1}{2}}$, of all phases present in the $Fe_{65}Ni_{28}Mn_7$ mixture during mechanical alloying is shown in Figure 6.6, Figure 6.7, Figure 6.8 and Figure 6.9. During the first 10 hours of milling, the average crystallite size of the Fe decreases rapidly from 150 to around 60 nm. The Ni and Mn exhibit the similar behavior, with crystallite sizes of 42 and 38 nm, respectively. After 25 hours of milling, the crystallite of the BCC and FCC phases progressively drops to approximately 11 nm and 10 nm, respectively. In contrast, lattice strain increased inversely with mechanical alloying time. This trend is seen for all elements and phases. After 10 hours of milling, the lattice strain increases by up to 2% for Fe and Ni, and by up to 1% for the BCC phase and 0.9% for the FCC phase.

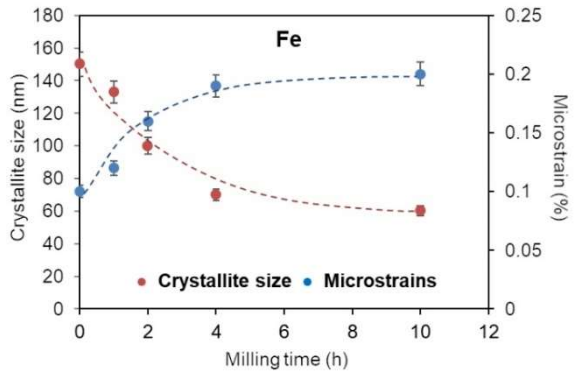

Figure 6.6: Evolution of the microstructure parameters of the BCC-Fe during the milling.

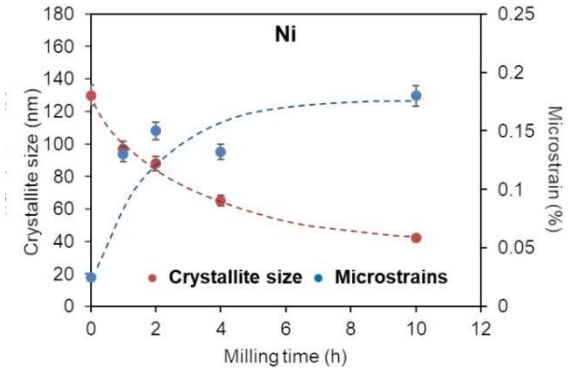

Figure 6.7: Evolution of the microstructure parameters of the FCC-Ni during the milling.

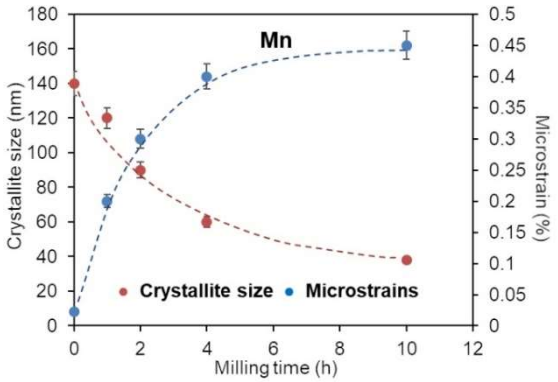

Figure 6.8: Evolution of the microstructure parameters of the BCC-Mn during the milling.

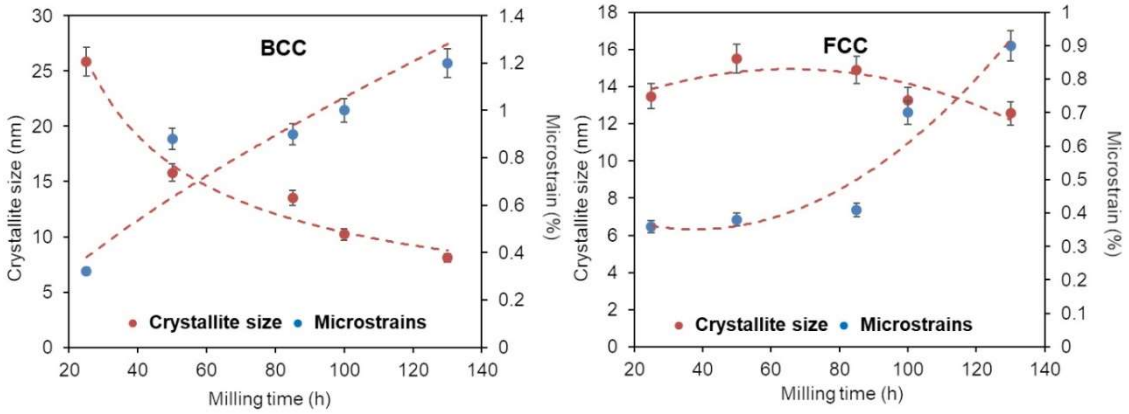

Figure 6.9: Evolution of the microstructure parameters of the BCC and FCC solid solutions during the milling.

The measured BCC and FCC dislocation densities in the mechanical alloy $Fe_{65}Ni_{28}Mn_7$ are shown in Figure 6.10. As the milling time goes from 1 to 85 hours, we can notice a

large increase in ρ_D from roughly 0.004 $10^{16}/m^2$ to 0.534 $10^{16}/m^2$. ρ_D rises considerably with extended milling times, reaching 0.619 $10^{16}/m^2$ after 130 hours of milling. The FCC phase increases significantly from around 0.001 $10^{16}/m^2$ at 1h to 0.55 $10^{16}/m^2$ at 25h. At the end of the milling, the ρ_D slightly increases to 0.80 $10^{16}/m^2$.

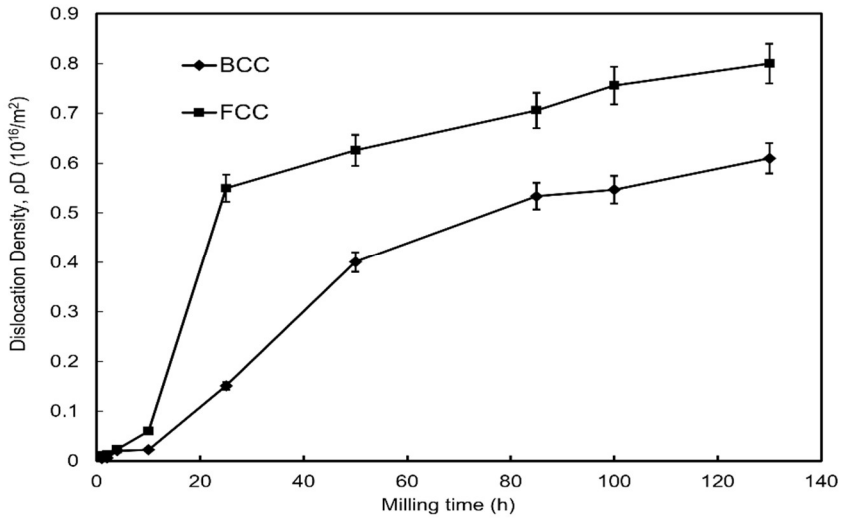

Figure 6.10: Variation of dislocation density as function of the milling time.

The phase proportion of the BCC and FCC solid solutions for more than 25h of MA is shown in Table 6.3. At 25h (where begun the coexistence of the two phases), the FCC phase appears to be a minor phase with a proportion of against the BCC phase. Continuous milling reduces the proportion of the BCC phase. By the end of the milling, only 18% of the BCC and 82% of the main FCC phase were determined.

Milling time (h)	BCC-phase proportion (%)	FCC-phase proportion (%)
25	59	41
50	35	65
85	37	63
100	28	71
130	18	82

Table 6.3: The phase proportions of the BCC and FCC phases during milling.

6.2.3 Morphology

Secondary electron SEM images of $Fe_{65}Ni_{28}Mn_7$ alloy powders after different milling times are shown in Figure 6.11. The un-milled particles just mix together with no obvious distortion (Figure 6.11.a). Because of the strong plastic deformation and repetitive fracture / cold welding processes caused by ball-powder-ball impacts, milling for 4 hours (Figure 6.11.b) modifies the original morphology of the powders [112]. During the early phases of milling, the average size of the powder agglomerates increased by up to 10h. The major impact is cold welding (see Figure 6.11.c). The agglomeration size did not develop any further between 25 and 85h due to the balance between cold-welding and fracture of the milled powder. Large particles became smaller towards the end of the milling operation, with a polyhedral form and rounded corners (Figure 6.11.f).

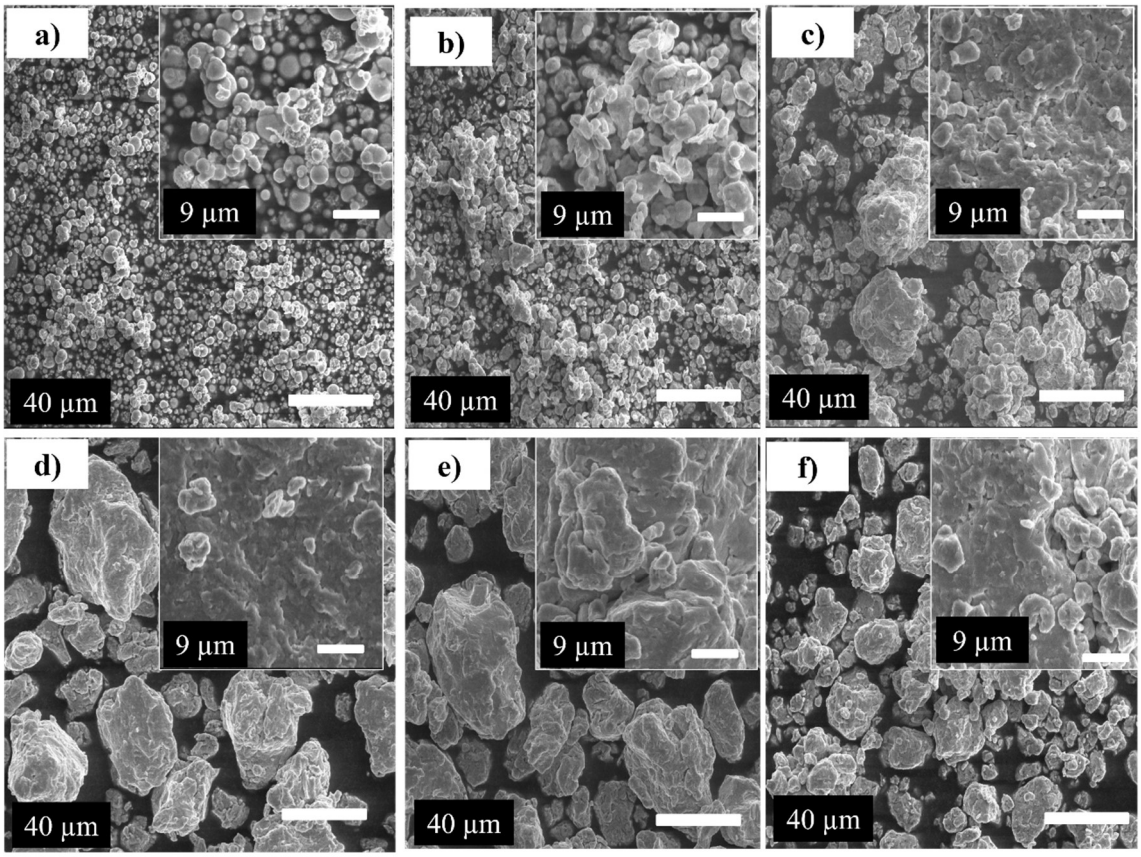

Figure 6.11: Scanning electron micrographs corresponding to mechanically milled powders: (a) 0h, (b) 4h, (c) 10h, (d) 25h, (e) 85h and (f) 130h. The bar scale of the images is 40 µm.

6.3 Arc Melting

6.3.1 XRD Analysis

The XRD diffraction patterns of the material produced by Arc melting is shown in the Figure 6.12. After polishing, the XRD pattern indicates that the alloy contains a single FCC phase. The calculated and the theoretical densities are 7573 kg/m^3 and 7870 kg/m^3, respectively. This suggests that densification is not complete and that porosities of around 3.77% are present

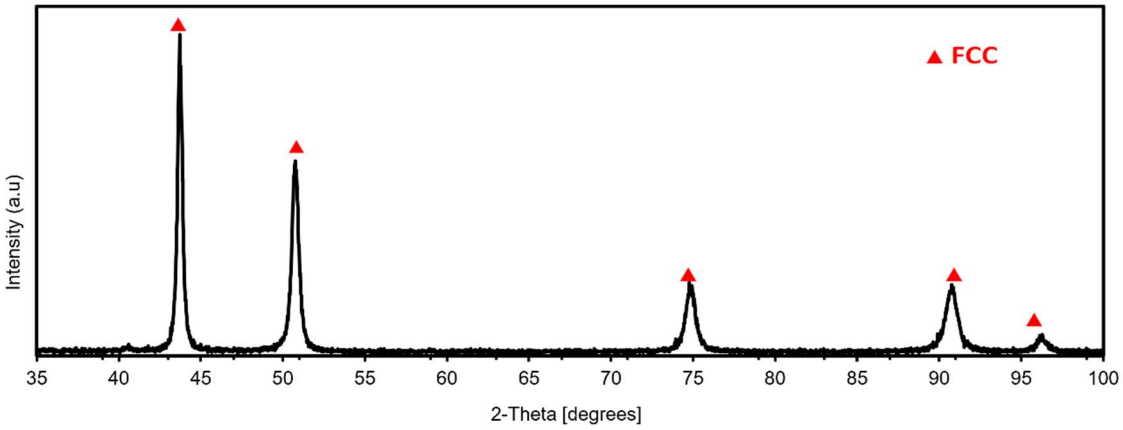

Figure 6.12: XRD patterns of the $Fe_{65}Ni_{28}Mn_7$ alloy after Arc melting process.

6.3.2 Morphology

The SEM micrograph of the core in secondary electron (SE) mode and the EDS of the specimen after Arc melting is shown in the figure 6.13. As demonstrated in the SEM micrographs, the sample has visible pores or cavities in the surface. However, the existence of pores tends to affect composites' mechanical and fatigue properties. The appearance of pores in our investigation can be explained by the sample's relatively fast cooling throughout the peritectic and eutectic processes during melt and remelt. The atomic concentrations of Fe, Ni, and Mn in the sample's corresponding energy-dispersive X-ray spectra (EDS) are 65.9, 28.8, and 5.3 at. %, respectively, which is quite near to the nominal composition of $Fe_{65}Ni_{28}Mn_7$.

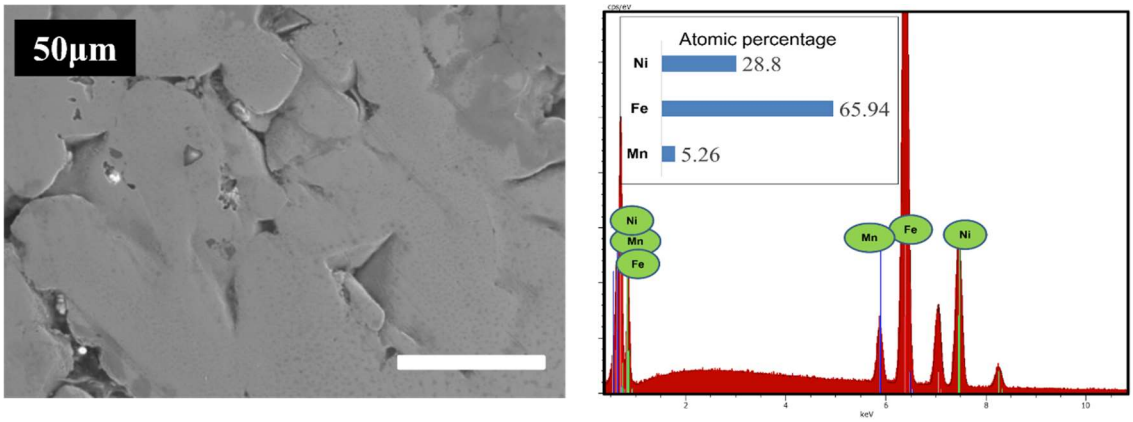

Figure 6.13: SEM image and corresponding EDS analysis of the $Fe_{65}Ni_{28}Mn_7$ alloy after Arc melting process.

6.4 Consolidation by SPS

6.4.1 XRD Analysis

Figure 6.14 illustrates the XRD analysis performed by SPS on the final powder milled at 130h for the $Fe_{65}Ni_{28}Mn_7$ alloy with different sintering temperatures. As shown, sintering the material at 750°C under 50 MPa pressure for 10 minutes nearly removed the BCC phase (1.8%). MnFeO oxide formation was also detected (6.9%). The dominant FCC phase (91.3%) has an average particle size of roughly 50.27 nm. This sample has a density of 97.66% and porosity of about 2.34%. When the pressure is raised to 75 MPa and the temperature is maintained at 750°C, the BCC phase disappears, the density rises slowly to 97.76% and the porosity decrease to about 2.34%. Increase in the average particle size of the FCC phase was calculated to about 50 nm. An increase in the sintering temperature to 1000°C with 50 MPa pressure results in the presence of the same FCC phase (95.9%) with higher average particle size more than 100 nm, a decrease of the amount of the MnFeO oxide (4.1%), with a significant increase in density (98.54%) and decrease in porosity (2.24%).

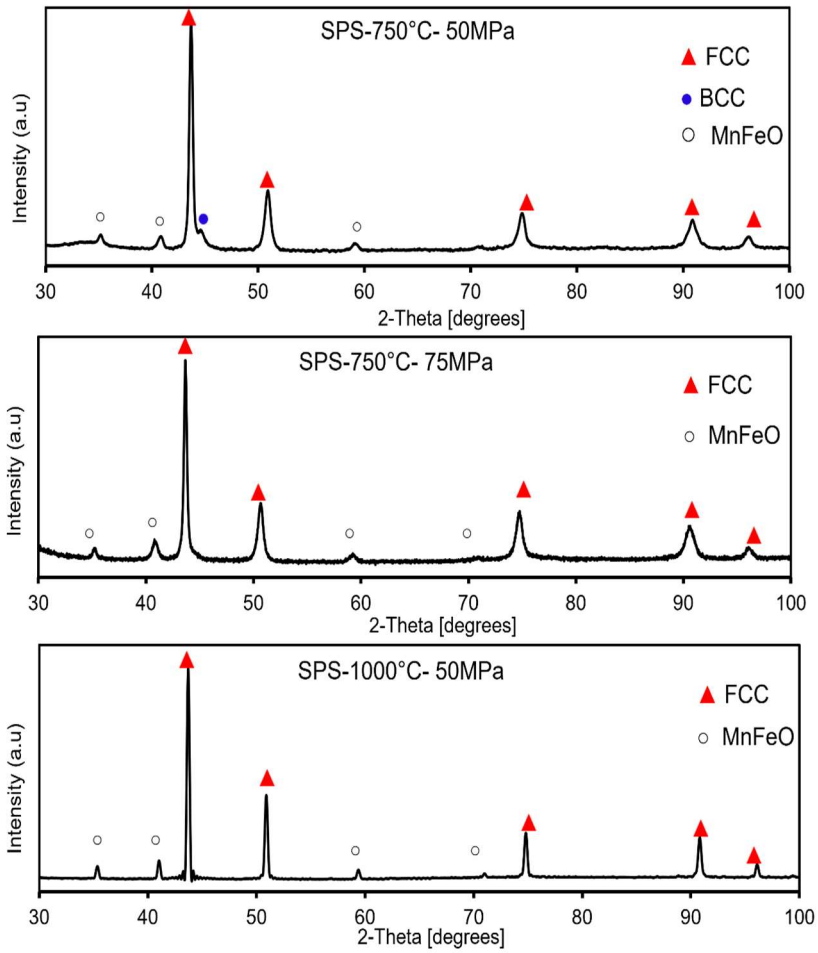

Figure 6.14: XRD patterns of the $Fe_{65}Ni_{28}Mn_7$ alloy after SPS.

6.4.2 Morphology

Figure 6.15 shows the corresponding SEM images of sintered $Fe_{65}Ni_{28}Mn_7$. Sintering the powder at 750°C under 50 MPa and 750°C under 75 MPa reveals 2.34% and 2.24% porosity, respectively. Pores are still visible when the pressure is increased, but their size is reduced. An increase in the sintering temperature to 1000°C with a pressure of 50 MPa results in a significant decrease in porosity of 1.46%. From the SEM images, it is found that some of the oxides were grouped as strings as well as individual particles. The oxides deform during high-temperature sintering to reduce surface energy (getting spherical shape).

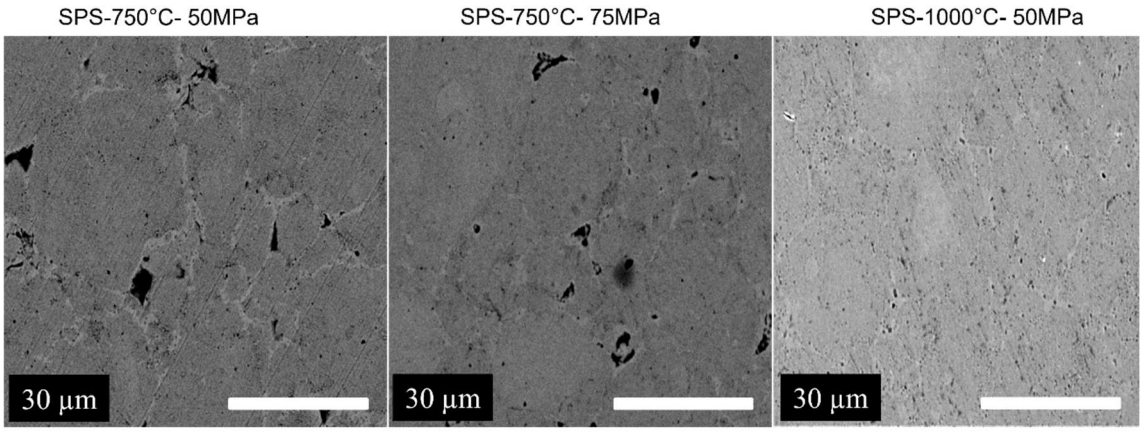

Figure 6.15: Scanning electron micrographs of the $Fe_{65}Ni_{28}Mn_7$ alloy after SPS.

6.5 Magnetic Analysis

Magnetic properties were measured and magnetization hysteresis curves were generated using a vibrating sample magnetometer. Figure 6.16 depicts the hysteresis curves of mechanical alloying powder, arc melting specimens, and spark plasma sintering samples after 750°C and 1000°C. The saturation magnetization (Ms), coercivity (Hc), and remanence to saturation ratio (Mr/Ms) values are shown in Table 6.4. Except for the prealloyed powder which exhibits semi-hard behavior, all of the hysteresis loops provided exhibited typical soft magnetic properties, as illustrated in figure 6.16.a and figure 6.16.b. The magnetic saturation of the semi-hard magnetic as-milled powder was around 122.10 (emu/g) and the coercivity was about 24 Oe. Previous research has found that the FCC phases enhance magnetic saturation [113]. The magnetic saturation of the SPS-produced sample at 750°C/75MPa is lower than that of the SPS-produced sample at 750°C/50MPa. This observation might be explained by the disappearance of the BCC phase as pressure is raised. Sintering the powder at 750° C under pressures of 50 MPa and 75 MPa resulted in coercivity values of 0.60 Oe in both specimens. Sintering at 1000°C under 50 MPa pressure resulted in an improvement (soft behavior) in coercivity to 0.07 Oe and saturation magnetization to 118.10 (emu/g). Similarly, raising the sintering temperature generates an increase in saturation magnetization, according to previous study [114]. The drop in Hc value with increased sintering temperature is due to structural strain released during the MA process. The saturation ratio rose from 0.020 after milling to 0.11 after SPS at 750°C at a pressure of 50 MPa, then decreased to 0.074 after SPS at 1000°C under a pressure of 50 MPa. The release of microstrain and domain wall energy as temperature

rises might explain this reduction. SPS at 1000 °C results in a favorable balance of saturation magnetization, coercivity, and saturation ratio.

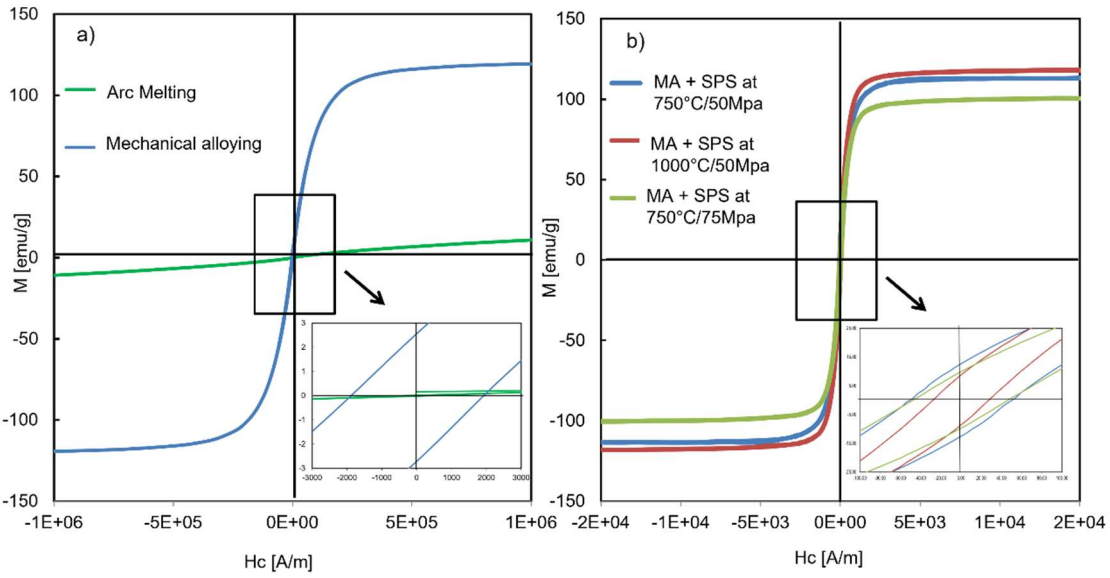

Figure 6.16: Magnetic hysteresis plots of the $Fe_{65}Ni_{28}Mn_7$ alloy after three processes, a) MA and Arc melting and b) SPS at 750°/50MPa ,750°/75MPa and 1000°C/50MPa.

Samples	M_s ($emug^{-1}$)	M_r ($emug^{-1}$)	H_c(Oe)	M_r/ M_s
As-milled	122.10	2.55	24.07	0.0209
Arc Melting	18.81	0.015	2.26	0.0008
MA + SPS at 750°C/50MPa	113.61	12.61	0.60	0.11
MA + SPS at 750°C/75MPa	100.58	9.845	0.60	0.10
MA+ SPS at 1000°C/50MPa	118.15	8.72	0.07	0.074

Table 6.4: Magnetic characteristics of the $Fe_{65}Ni_{28}Mn_7$ alloy After mechanical alloying, arc melting and spark plasma sintering.

6.6 Mechanical properties

The Vickers hardness indentation test using a diamond indenter was used to determine the hardness of the sintered material composites. On polished samples, measurements were taken. The samples' hardness values were determined using a load of 1.96 N (200g) and a dwell duration of 10 s, a standard test approach for hard-metals and ceramic composites that is often documented in the literature [115-117]. The hardness values of the samples are shown in the table 6.5. The sample generated by Arc Melting exhibited

the lowest hardness (97 HV), which might be attributed to the sample's high porosity percentage when compared to the other samples. We can deduce from comparing the samples generated by spark plasma sintering that the sample sintered at 750°C under 75 MPa is substantially harder (425 HV) than the sample sintered at the same temperature under a lower pressure of roughly 50 MPa (328 HV). It is, however, harder than the sample sintered at 1000°C (216 HV), despite having a larger amount of porosity. All SPS samples had considerably higher yield strength and compressive strength, despite Arc melting producing the lowest results. These values are linked to the material's smaller grain size, increased dislocation density, and presence of scattered oxides. Furthermore, the HV, σ_y, and σ_{max} are affected by dislocation strengthening and ultrafine grains. However, like with the AM sample, raising the temperature results in a larger grain size. According to the Hall-Petch relationship, increasing grain size greatly affects compression yield strength. [118,119] The high yield strength is an important feature. It is frequently accompanied with increased wear resistance and decreased ductility. All SPS-consolidated samples showed highly interesting shortening at failure values A% more than 15% and severe noisy breaking during compression testing, however the arc melted sample supported shortening greater than 30% (test ended at 30%, no failure).

Samples	σ_y (MPa)	σ_{max} (MPa)	A%	Hardness (HV)
Arc Melting	123	>500 (no failure)	> 30 %	97 (3.08)
MA+SPSat 750°C/50MPa	1027	1470	15 %	328 (32.61)
MA+SPSat 750°C/75MPa	1350	1700	16 %	425 (18.81)
MA+SPSat1000°C/50MPa	1056	>1440 (no failure)	>15 %	216 (3.38)

Table 6.5: Mechanical properties: compressive strength (σ_{max}), yield strength (σ_y), shortening at failure (A%) and Vickers hardness of the $Fe_{65}Ni_{28}Mn_7$ alloy after arc melting and spark plasma sintering.

Figure 6.17 contrasts SEM images of fracture surfaces of specimens generated by arc melting and spark plasma sintering following compression testing. It is essential to note that the specimen synthesized by SPS at 1000°C/50MPa did not break during the compression test, showing that it is a ductile material (figure 6.17.d). The surface of the Arc melting specimen (not cracked, Figure 6.17.a) is characteristic of a homogenous ductile material. Various slip planes can be seen in varied grains with different orientations, resulting in step-like protrusions at the free surface. Inside, there are large slip lines as well as smaller ones grouped in chevrons. This is typical of a very

homogeneous material that has been subjected to severe deformation. The grains can be visible on the fracture surface of the specimen generated by SPS at 750°C/50MPa (Figure 6.17.b), showing that the rupture was intergranular. Furthermore, the visible dimples show that the rupture was mainly ductile. Increased sintering pressure to 75 MPa (Figure 6.17.c) causes a significant change in fracture mode to transgranular mode due to the strengthening of powder particle bonding, and the lack of dimples indicates that the fracture was brittle. The fracture brittleness may be expected from the Vickers hardness, which demonstrates that the sample sintered at 750°C under 75 MPa is much harder (425 HV).

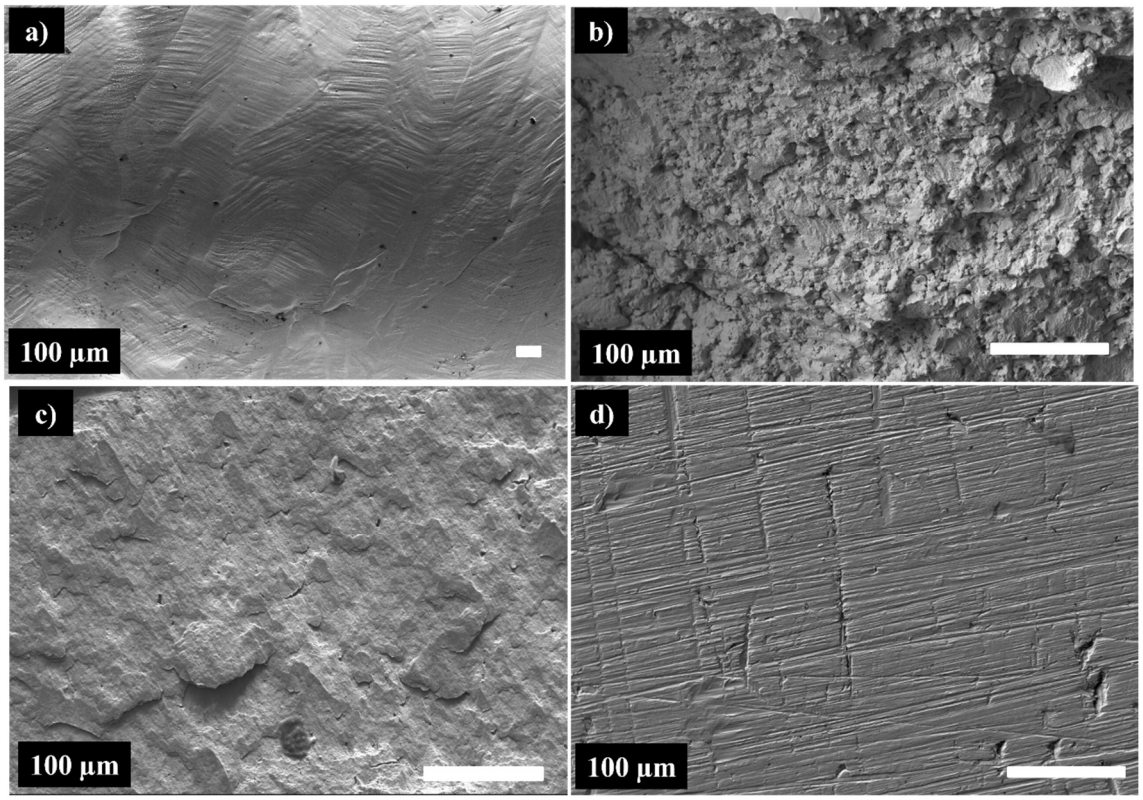

Figure 6.17: SEM image of the deformed surface of the Arc melting sample (a), fractography of the specimens synthesized by SPS at 750°C/50MPa (b), fractography of the specimens synthesized by SPS at 750°C/75MPa (c) and SEM image of the deformed surface after SPS at 1000°C/50MPa (d).

The high-resolution pictures in figure 6.18 depict vastly distinct materials. The fracture in the SPS 750°C / 50 MPa (Figure 6.18.a) is primarily intergranular, whereas the SPS 750°C / 75 MPa (Figure 6.18.b) is obviously transgranular. On the SPS 750°C / 50 MPa picture, interesting characteristics include clusters of grains (likely cold-welded nanograins) encased within a shell. This shell is most likely MnFeO oxide. There is also

some porosity. Both the pore and the shell were visible in cross section SEM images of the unfractured samples (Figure 6.17). There is no oxide shell or pores seen on the fractographic picture of the SPS 750°C / 75 MPa, indicating completely welded grains.

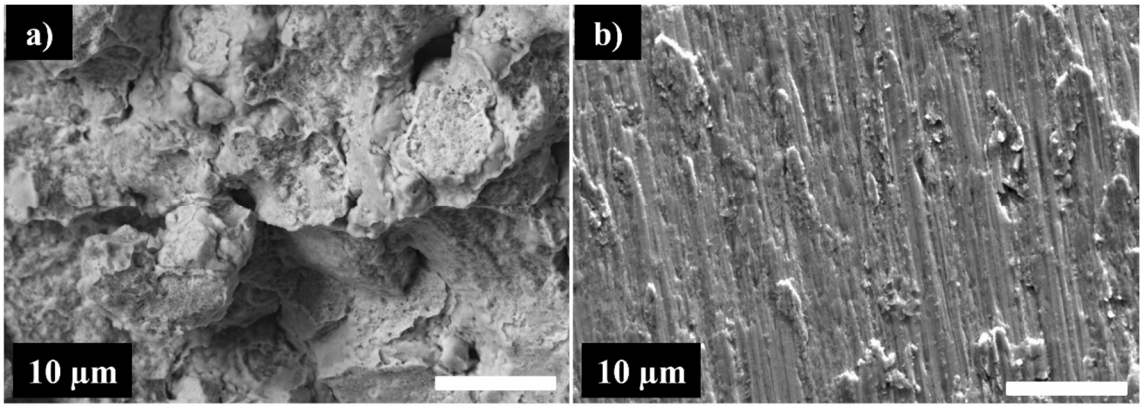

Figure 6.18: High resolution fractographic images of the SPS 750 / 50 MPa (a) and SPS 750 / 75 MPa (b) samples.

CHAPTER 7

Production and Analysis of FeCoMn

7.1 Introduction

As in the previous chapter, three techniques were used to synthesis FeCoMn alloy for comparison. Likewise, ternary equi-atomic alloys are an option as intermediate products to produce HEA alloys (first step the ternary and the addition of the additional two elements in a second step). XRD patterns of unmilled and milled samples at various milling times are shown. The typical peaks for the first mixed powders of Fe (BCC, Im-3m), Co (FCC, Fm-3m), Co (HCP, P63/mmc), and Mn (BCC, I-43m) are all found. Morphological examinations and Rietveld analysis are carried out for varied milling times using the Maud software. Morphological evaluations of the bulk materials were also undertaken, and their densities were determined using the Archimedes' Method. Magnetic experiments were carried out on both the final powder obtained by MA and the bulk materials. A mechanical comparison study (compression and Vickers Hardness) was also carried out between the AM samples and the SPS bulk materials. The process that has been followed for the synthesis of the alloy FeCoMn (at. %) is summarized in Figure 7.1:

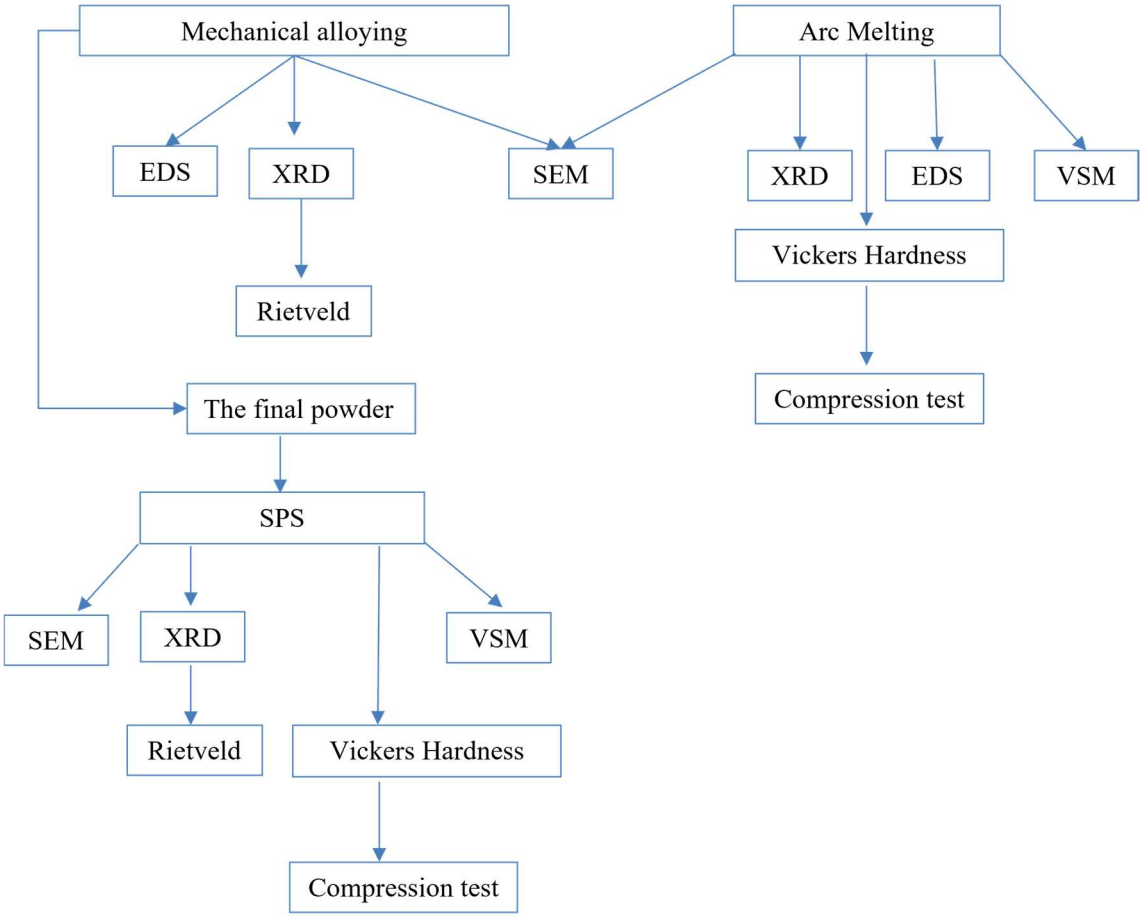

Figure 7.1: Process diagram for synthesis of FeCoMn (at. %) alloy.

7.2 Mechanical alloying

7.2.1 XRD Analysis

The sample prepared from equiatomic powdered iron, cobalt, and manganese is examined in this section. Energy Dispersive X-Ray Spectroscopy (EDS) has confirmed that the contamination from the vial materials is less than 1% atomic. Figure 7.2 shows the diffraction peaks of precursors as well as the presence of four pure elements' characteristic peaks: BCC-Fe, FCC-Co, HCP-Co, and BCC-Mn. All characteristic peaks are identified. Both the HCP and FCC-Co structures coexist in the premixed powder. The reflections of each phase are shown in Table 7.1.

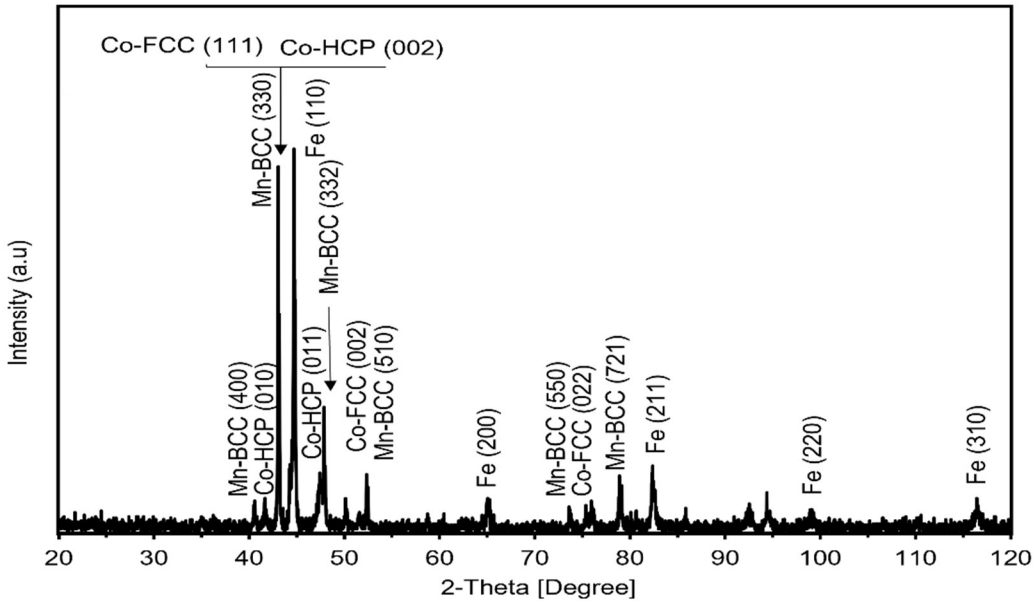

Figure 7.2: FeCoMn powder X-ray diffraction patterns before milling.

Phases	Reflexions					
BCC-Fe	(110)	(200)	(211)	(220)	(310)	
Co-FCC	(111)	(002)	(022)			
Co-HCP	(010)	(002)	(011)			
BCC-Mn	(400)	(330)	(332)	(510)	(550)	(721)

Table 7.1: Reflections present in the diffractogram of the sample $FeCoNi(B_{0,5}Si_{0,5})$ and corresponding phases.

7.2.2 Rietveld Analysis

The XRD pattern of FeCoMn powder before and after milling at various periods is shown in Figure 7.3. the best refining is achieved and shown in Table 7.2.

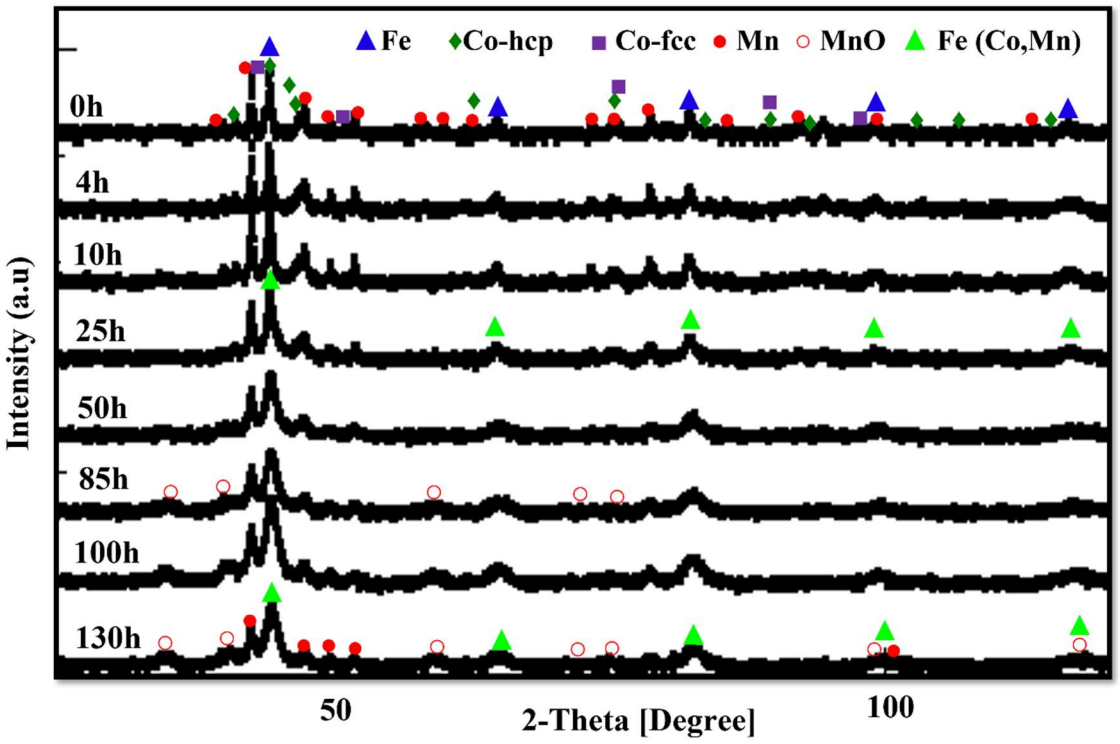

Figure 7.3: FeCoMn powder X-ray diffraction patterns as a function of milling time.

Milling time (h)	R_{wp}	R_{exp}	GoF(R_{wp}/R_{exp})
0	4.20	3.80	1.10
2	4.45	4.37	1.01
4	3.73	3.30	1.13
10	2.70	2.40	1.12
25	2.36	2.68	1.13
50	2.52	2.32	1.11
85	2.38	2.31	1.07
100	1.69	1.59	1.06
130	2.28	2.19	1.03

Table 7.2: The residual parameters and GoF values of the compounds identified using Rietveld analysis of the FeCoMn alloy.

The Bragg diffraction peaks corresponding to the pure elements are shown in the X-ray diffraction diagram of the initial powder (figure 7.4): Fe with structure bcc and crystal parameter a = 2.866(6) Å; Mn with structure fcc and crystal parameter a = 3.525(1) Å, Co with fcc structure and crystal parameter a = 3.544(5) Å and Co with hcp structure and crystal parameter a= 2.507(2) Å and c = 4.068(1) Å.

As milling time increase, the peaks broaden, which can be attributable to both grain size reduction and increasing lattice strain. After 10 hours of milling, in addition to the primary diffraction peaks of BCC-Fe and BCC-Mn, only HCP-Co is visible. This behavior is due to cobalt's allotropic transition from the FCC to the HCP phases. The FCC cobalt phase is metastable at ambient temperature, and this structure becomes unstable when subjected to external mechanical or thermal action. Furthermore, the disordered BCC-Fe (Co) solid solution (Im-3m structure) has begun to appear at this stage. A progressive drop in Mn peaks was seen up to 25 hours, indicating that Mn was beginning to dissolve in the BCC-Fe(Co) solid solution. Further milling to 50h reveals no identifiable cobalt peaks; the manganese peaks get weaker; this indicates the creation of solid solution bcc-Fe (Co,Mn). The major peak of manganese remained after extending the milling process to 85 hours, however it had been broadened and its intensities had already been greatly lowered. Meanwhile, manganese oxide, MnO (Ref. Code: 01-075-0257) phase peaks developed, which can be produced by both recrystallization and oxygen contamination during powder handling at this stage. When the temperature rises during the milling operation, the recrystallization effect may occur. The negative heat produced by mixing between each pair of atoms generates thermodynamic energy, which is used to dissolve the components elements [120]. The heats of mixing in our system for the Fe-Mn and Co-Mn couples are 0 and -5 $kJmol^{-1}$, respectively [121]. Consequently, the existence of manganese diffraction peaks even after 100 h of milling is due to the significantly lower interdiffusion of manganese and other elements. After 130 hours of milling, the solid solution production of bcc-Fe(Co,Mn) alloy appears to be more complete.

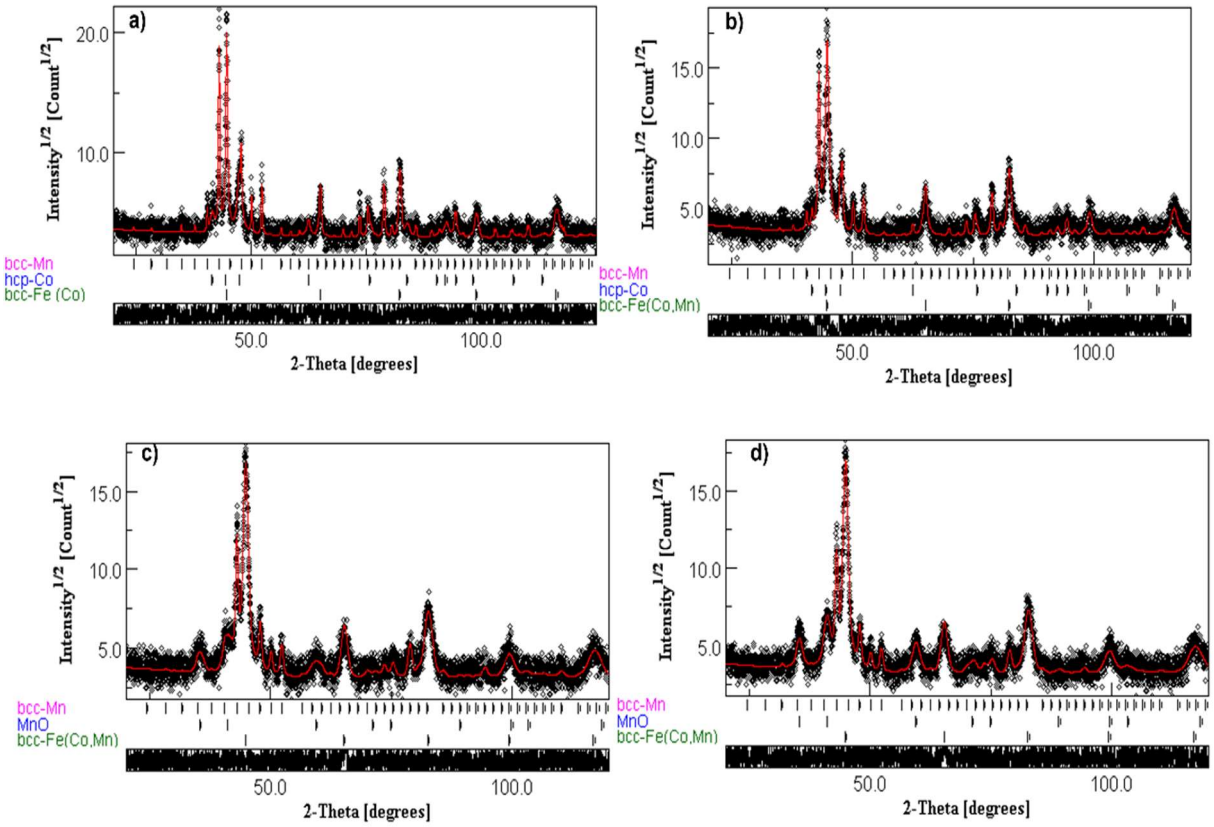

Figure 7.4: Rietveld refinement of the XRD pattern of the FeCoMn powder: (a) after 10h (b) 25h, (c) 85h, (d) 130h.

The variation of the lattice parameter as a function of milling time for FeCoMn alloy is shown in Figure 7.5. After 10 h of milling, the lattice parameter increases very slightly, from 2.867(1) Å for pure Fe to 2.867(4) Å, representing a cell volume expansion of about 0.97 %. This increase is due to the formation of the BCC-Fe (Co) solid solution, which is caused by the incorporation of cobalt atoms into the iron lattice. After 25 hours of milling, the lattice parameter decreases to 2.866(1)Å, indicating that the BCC-Fe (Co,Mn) solid solution has begun to form. This decrease is accompanied by a shift of the main characteristic peak of the Fe to higher 2θ angles, from 44.69° to 44. 71°.The lattice parameter decreases gradually with increasing milling time, reaching a value of 2.855(5) Å after 130h, suggesting the progressive insertion of Mn into the Fe lattice.

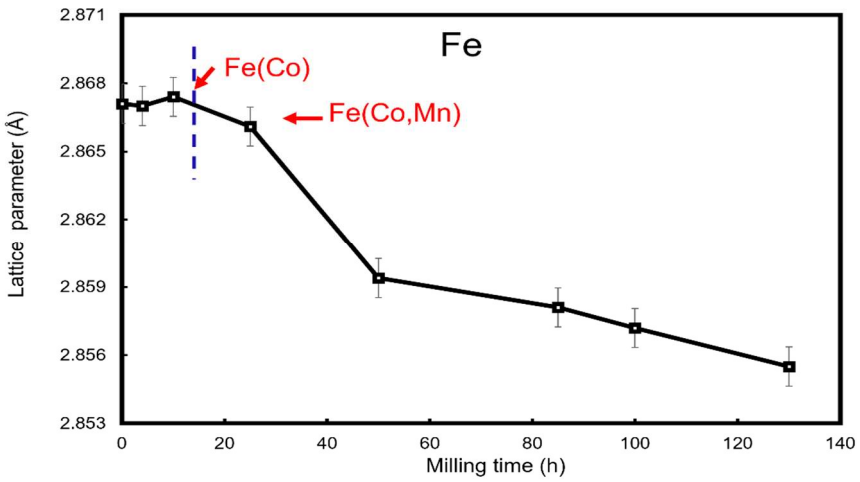

Figure 7.5: The evolution of the principal phases lattice parameter during MA of FeCoMn.

The evolution of the average crystallite size, <L>, and the microstrain rate, $< \sigma^2 >^{\frac{1}{2}}$, of Fe present in the FeCoMn mixture during mechanical alloying is shown in Figure 7.6. As can be observed, increasing the milling time causes a fast drop in crystalline size (less than 20 nm) after 25 hours. The size of the crystallites reduces substantially to roughly 19 nm due to the production of solid solution BCC-Fe (Co,Mn). As the milling duration is increased, more refining happens gradually until around 16 nm (130 h). The crystallite size of mechanical alloyed equiatomic FeCoMn is governed by milling duration rather than composition in this work [122]. Lattice strains, on the other hand, rise fast with increasing milling time at beginning and gradually as milling time increases. The final value was around 0.5% after 85 hours of milling. A size mismatch between the components causes the rise in lattice strain, which has a microstructure origin. Another argument is that strong plastic deformation causes an increase in grain boundary percentage, mechanical deformation, and dislocation density.

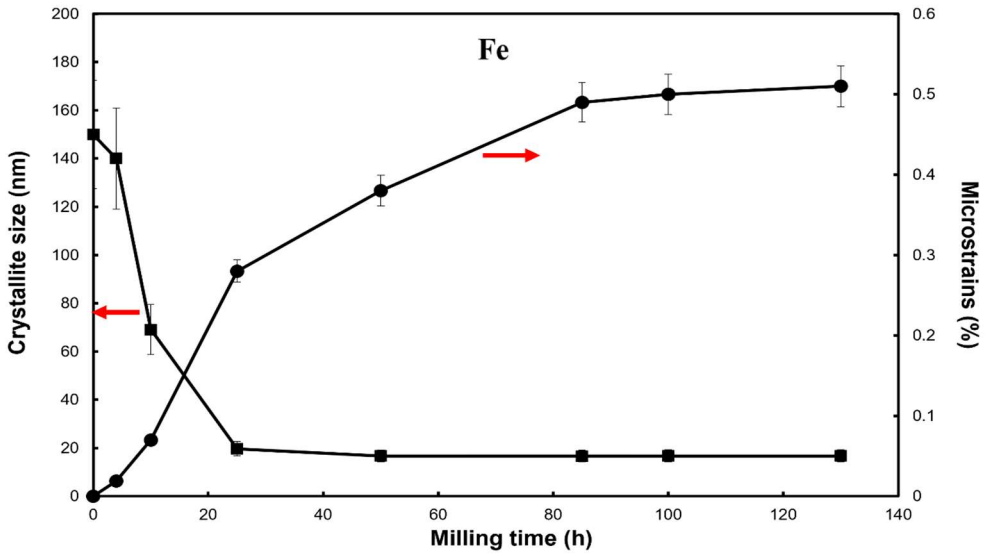

Figure 7.6: Microstructure parameters of the main phase (BCC-Fe) as a function of milling time.

The measured dislocation densities in the mechanical alloy FeCoMn are shown in Figure 7.7. The dislocation density was calculated in the same method as in Chapter 3, using the equivalent Burgers vector of the BCC phase. With increasing milling time from 4 to 50 h, we can see a significant rise in ρ from around $0.051 \times 10^{16}/m^2$ to $0.350 \times 10^{16}/m^2$ and then, the ρ slowly increases till the end of the milling, reaching $0.357 \times 10^{16}/m^2$.

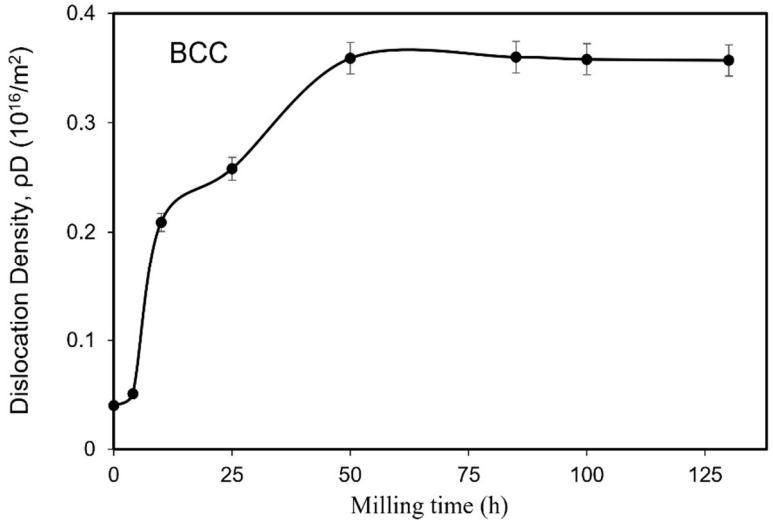

Figure 7.7: Variation of dislocation density as function of the milling time.

The phase proportion of the BCC-Fe (Co,Mn) ,BCC-Mn phase and MnO oxide phases from 25h is shown in Table 7.3. At 50h the cobalt is totally disappeared and the BCC-Fe(Co,Mn) phase registered a maximum proportion of about 69%. Continuous milling reduces the proportion of the BCC phase, the BCC-Mn and rises the formation of the MnO.

Milling time (%)	BCC-Fe (Co,Mn) phase proportion (%)	HCP-Co phase proportion (%)	BCC-Mn phase proportion (%)	MnO phase proportion (%)
25	59	6	35	-
50	69	-	31	-
85	61	-	25	14
100	63	-	22	15
130	61	-	19	20

Table 7.3: The phase proportions of the BCC and FCC phases during milling.

7.2.3 Morphology

Figure 7.8 illustrates the morphological shape change of milled powder at various milling times. The un-milled powders have an irregular form and size, as seen in Figure 7.8.a. As seen in Figure 7.8.b, the particles flattened after 4 hours of milling due to the introduction of compressive forces into the particles caused by ball-powder-ball collisions. As a result of the extreme fracture and cold welding, the particles took on an irregular shape and layered structure after milling for 10 hours or more (see figure 7.8.c). The multilayer structure was created using cold welding and repeated mechanical deformation. After 25h of milling, compressive pressures are exerted on the particles as a result of repeated collisions between balls and particles, causing them to flatten, fracture, and cold weld (see figure 7.8.d). Because of the equilibration of the cold welding and fracturing processes, prolonged milling results in a smaller particle size distribution. (Fig 8.e, f).

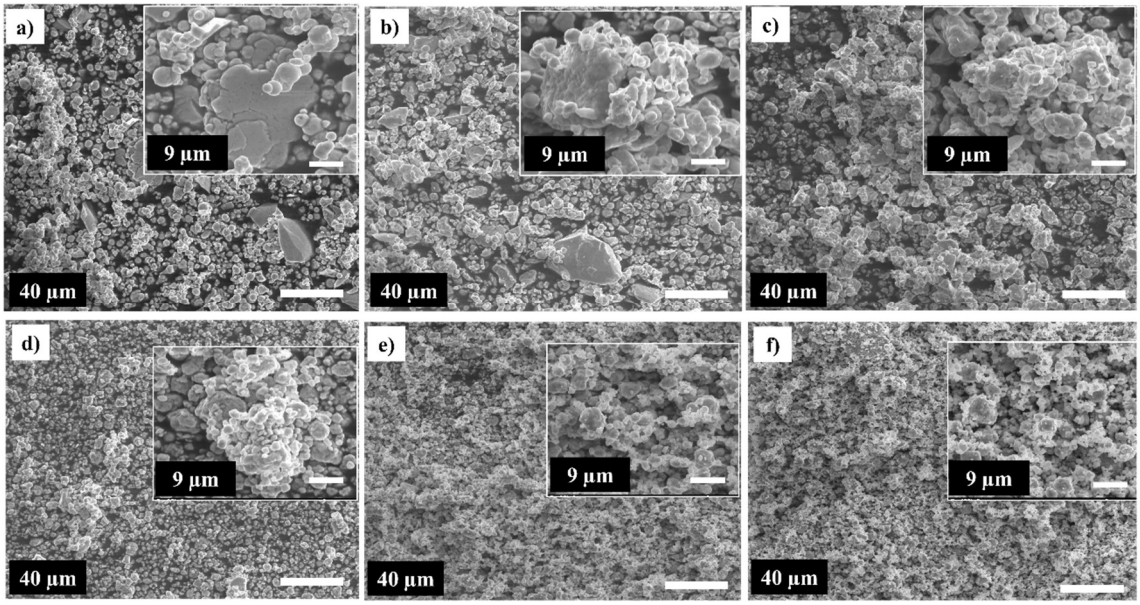

Figure 7.8: Scanning electron micrographs of mechanically milled powders: (a) 0h, (b) 4h, (c) 10h, (d) 25h, (e) 85h and (f) 130h.

7.3 Arc Melting

7.3.1 XRD Analysis

The FeCoMn alloy ingot is cuted and polished after vacuum arc melting. Figure 7.9 shows the results of an XRD investigation on FeCoMn alloy. The resulting alloy may be identified as a cobalt-based alloy with a single HCP-Co (Fe,Mn) phase. The calculated and the theoretical densities are 8363 kg/m^3 and 7891kg/m^3, respectively. This signifies that it is a completely dense sample.

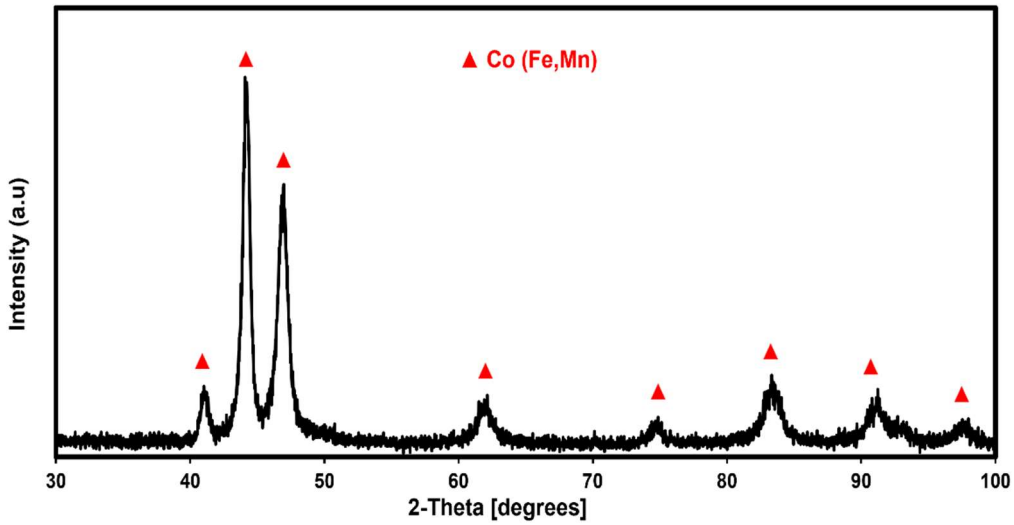

Figure 7.9: XRD patterns of the FeCoMn alloy after Arc melting process.

7.3.2 Morphology

The micrograph shows a SEM micrograph of the core in secondary electron (SE) mode of the specimen generated following Arc melting. The Co (Fe,Mn) phase is proven to be the only phase present in the FeCoMn alloy, as revealed by the XRD pattern in Figure 7.9. The sample shows obvious superficial pores or cavities in the surface of the SEM micrographs. The chemical attack during the MEB analysis can explain the formation of pores in our study.

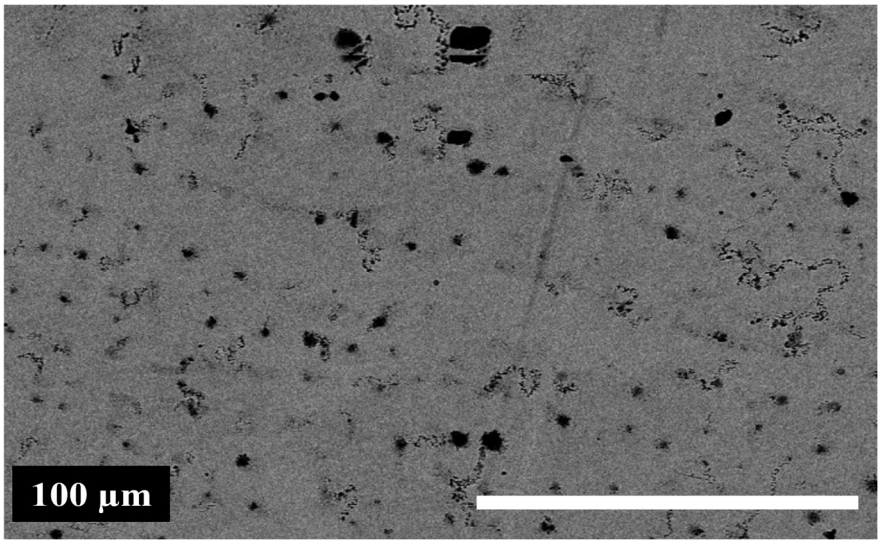

Figure 7.10: SEM image of the FeCoMn alloy after Arc melting process.

7.4 Consolidation by SPS

7.4.1 XRD Analysis

The XRD pattern of the specimens following SPS consolidation is shown in the figure 7.11. The samples were mechanically polished the same way as mentioned in the chapter 5. Compressing the powder at 750 °C for 10 minutes under 50 MPa pressure resulted in the formation of the BCC dominating phase (44.6%), FCC phase (24.4%), and MnO oxide phase (31%), as has been shown. The BCC and FCC phase have an average particle size size of roughly 50 nm and 88 nm, respectively. When sintered to 1000°C, the amount of FCC phase reduces dramatically to 8.5% with an average particle size > 100 nm. While the amount of BCC phase rises to 60.2%. The average particle size of the BCC phase was about 71 nm.

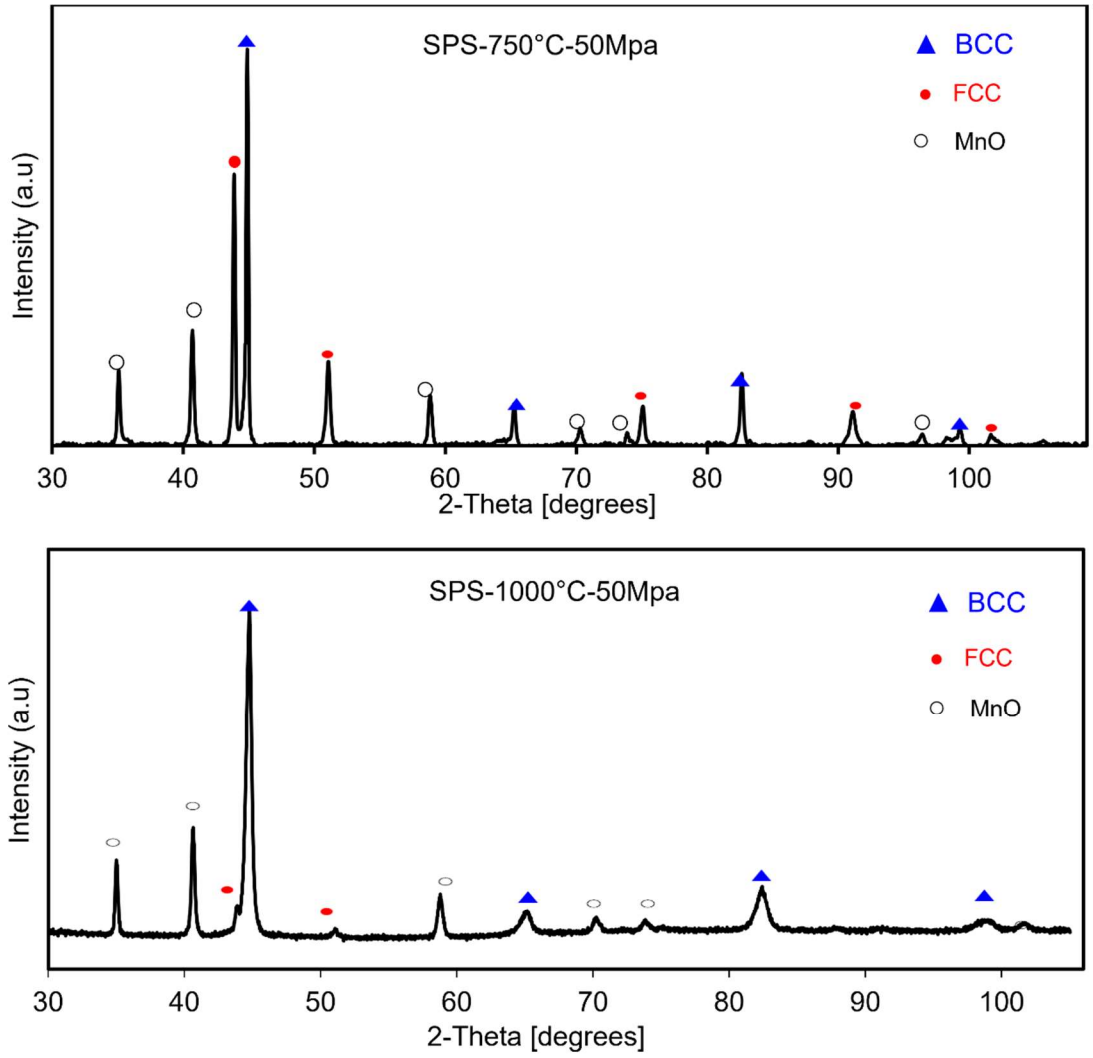

Figure 7.11: XRD patterns of the FeCoMn alloy after SPS.

7.4.2 Morphology

The influence of SPS temperatures on the microstructure of sintered samples is clearly demonstrated by SEM microstructural investigation (Figure 7.12). The sintered sample exhibits fine particles at SPS temperature of 750 °C. The size of the particles grows slightly when the SPS temperature rises to 1000 °C. There was no significant porosity in the two specimens following SPS sintering. The densities of the obtained specimens consolidated at 750 °C and 1000 °C are 6970 kg/m^3 and 6973 kg/m^3, respectively. This indicates that densification has been accomplished and there is low or almost no porosity. The theoretical densities of SPS-750°C -50MPa and SPS-1000°C -50MPa are 6965 kg/m^3 and 6950 kg/m^3, respectively.

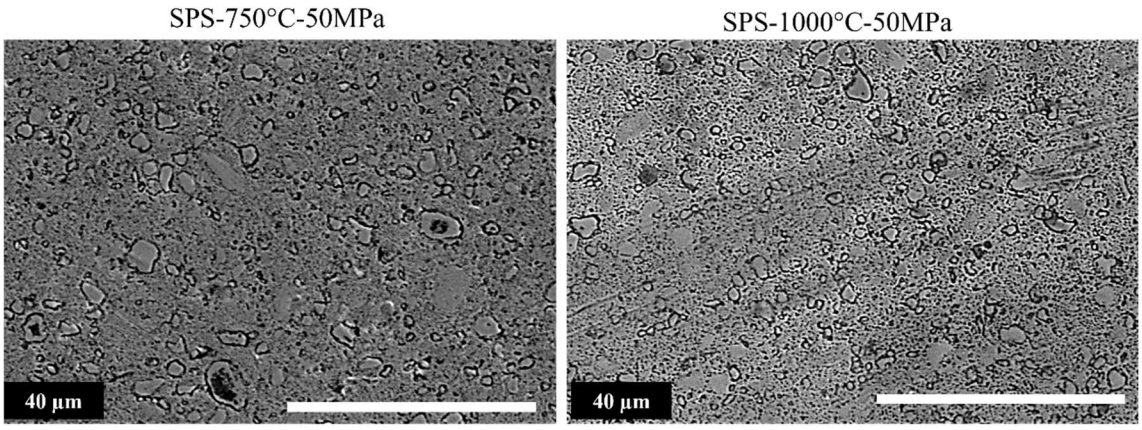

Figure 7.12: Scanning electron micrographs of the FeCoMn alloy after SPS.

7.5 Magnetic Analysis

Figure 7.13 depicts the hysteresis curves of mechanical alloying powder, arc melting specimens, and spark plasma sintering samples after 750°C and 1000°C degrees. Except for the prealloyed powder which exhibits soft magnetic behavior, all of the hysteresis loops demonstrated semi- hard magnetic response. The saturation magnetization (Ms), coercivity (Hc), and remanence to saturation ratio (Mr/Ms) values are shown in Table 7.4. As shown, the as-milled powder had magnetization saturation of about 8.2310^{-5} (emu/g) and a coercivity of around 2.410^{-4} Oe. The reduced value of coercivity is related to grain refinement. In fact, for nanocrystalline materials with grain sizes smaller than the magnetic exchange length and a higher density of grain borders, the presence of more grain boundaries increases the number of broken bonds in the sample and, as a result, the number of unpaired electrons. The presence of unpaired electrons in a material causes it to exhibit ferromagnetic activity. The link between crystallite size and coercive force is founded on Herzer's well-known coercivity-crystalline size relationship [123]. After SPS sintering at 750 °C under 50 MPa pressure, the sample had a saturation magnetization of around 38.36 ($emug^{-1}$) and a coercivity of about 72.68 Oe. Maintaining the same pressure while increasing the temperature to 1000 °C improved the alloy's magnetic softness. The sample had a saturation magnetization of around 56.92 (emu/g) and a coercivity of about 39.85 Oe. The increase in saturation magnetization on the second SPS sintering is explained by the fact that the amount of BCC phase is greater after sintering at 1000°C, according to the XRD data. However, Magnetic Saturation in BCC phase is often higher than magnetic saturation in FCC phase. So, the results indicate that magnetic saturation of compacted FeCoMn alloy by SPS at 1000°C is strongly related to its crystalline

structure. Furthermore, the magnetic interactions of most Fe-Fe, Co-Co, and Fe-Co couples are stronger in the BCC phase than in the FCC phase [124,125]. On the other hand, the local defects such as release of residual stress [126] and grain growth [127] are improved after sintering at 1000°C. This reduces the pinning sites for domain wall movements resulting in a lower coercivity and lower saturation ratio values (0.012 after SPS at 1000°C).

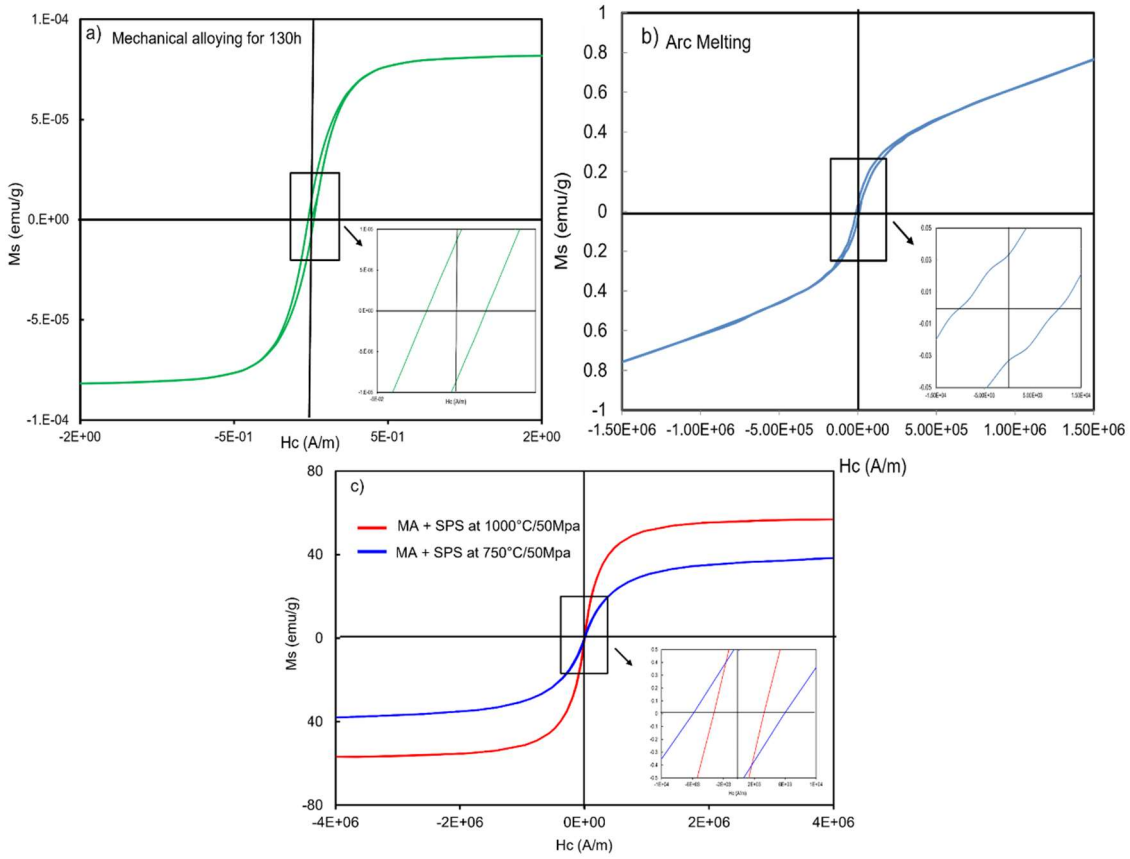

Figure 7.13: Magnetic hysteresis plots of the FeCoMn alloy after three processes, a) MA b) Arc melting and c) SPS at 750°/50MPa and 1000°C/50MPa.

Samples	M_s (emug^{-1})	M_r (emug^{-1})	H_c(Oe)	M_r/ M_s
As-milled	8.2310^{-5}	8.5510^{-6}	2.410^{-4}	1.0410^{-1}
Arc Melting	1.01	0.03	124.28	0.033
MA + SPS at 750°C/50MPa	38.36	0.5	72.68	1.3010^{-2}
MA + SPS at 1000°C/50MPa	56.92	0.73	39.85	1.2810^{-2}

Table 7.4: Magnetic characteristics of the FeCoMn alloy After mechanical alloying, arc melting and spark plasma sintering.

7.6 Mechanical properties

Table 7.5 illustrates the Vickers hardness (HV), compressive strength (σ_{max}), yield strength (σ_y), and shortening at break values. Small parallelepiped indenters were used for the compression experiment. The Vickers hardness indentation testes were investigated similarly as it was previously described in the chapter 6. SPS samples exhibit considerably greater HV, yield strength, and compressive strength than AM samples, which is due to smaller grain size, larger dislocation density, and the presence of scattered oxides throughout the material. On the other hand, processing technology has a significant impact on the HV, σ_y, and σ_{max}. They are hence dependent on ultrafine grains and dislocation strengthening. Increasing the temperature results in an increase in grain size in the AM sample. Based on the Hall-Petch relationship, increasing grain size greatly affects compression yield strength [128]. By analyzing the samples produced by spark plasma sintering, we can deduce that the sample sintered at 750°C is substantially harder (647 HV) than the sample sintered at 1000°C. the sample produced by SPS at 1000°C showed higher shortening at failure values A% more than 22%. The obtained sample following SPS at 750 °C, on the other hand, exhibited a reduced shortening at failure values A% of around 3% and cracks noise during compression test, indicating that it is a hard and brittle material.

Samples	σ_y (MPa)	σ_{max} (MPa)	A%	Hardness (HV)
Arc Melting	120	1090 (no failure)	> 30%	193 (23.40)
MA + SPS at 750°C/50Mpa	1031	1120	3 %	647 (23.61)
MA + SPS at 1000°C/50Mpa	1960	2290	22%	308 (5.92)

Table 7.5: Mechanical properties: compressive strength (σ_{max}), yield strength (σ_y), shortening at failure (A%) and Vickers hardness of the FeCoMn alloy after arc melting and spark plasma sintering.

Figure 7.14 shows a comparison of SEM images of fracture surfaces obtained by arc melting and spark plasma sintering after compression testing. The surface of the Arc melting specimen (which is not broken, see Figure 7.14.a) is typical of a homogeneous ductile material. There are sliding planes that are aligned at about 45 degrees with the compression direction (shear stresses are maximum at 45 degrees). Inside the grains, we can find sliding planes that are oriented differently from one grain to the next, depending

on the crystallographic orientations of the planes most likely to slide, which is the plane family for FCCs. These are the planes {1,1,1} with the closest angle to 45° to the loading direction. Figure 7.14.b shows a fracture plane oriented at around 45 degrees to the load direction. The grains are visible on the fracture surface of the specimen formed by SPS at 750°C/50MPa indicating an intergranular rupture. In figure7.14.c, the grain size appears to be larger than for SPS 750°C, indicating that SPS 1000°C was subjected to recrystallisation and maybe growth grain. This recrystallisation explains why grain size is more uniform at SPS 1000°C than at SPS 750°C, the rupture is also intergranular.

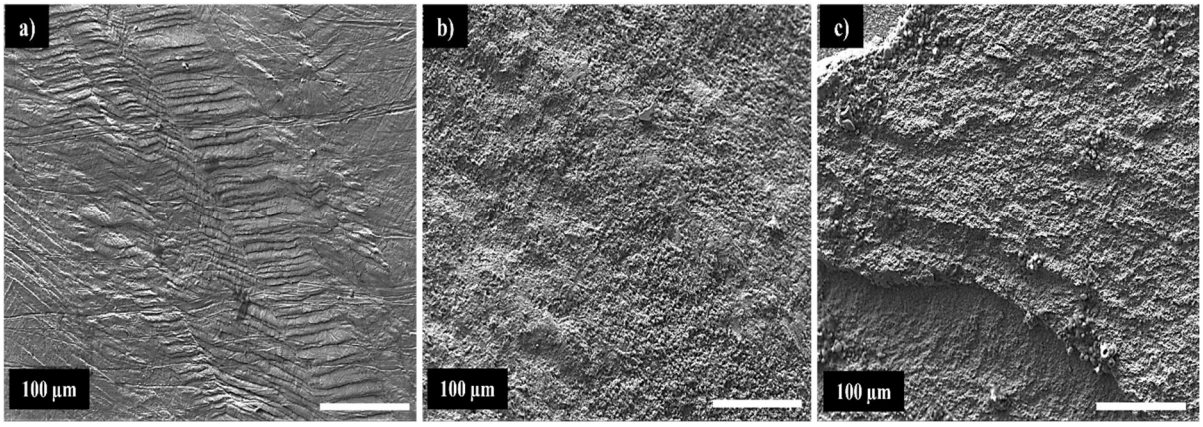

Figure 7.14: SEM image of the deformed surface of the Arc melting sample (a), fractography of the specimens synthesized by SPS at 750°C/50MPa (b), and SEM image of the deformed surface after SPS at 1000°C/50MPa (c).

CHAPTER 8

Comparison of results

8.1 Mechanical alloying (MA)

8.1.1 Structural and microstructural properties

Mechanical alloying	Structure	Crystallite size (nm)	Microstrain %	Lattice parameter Å	Dislocation density
$Fe_{70}Ni_{12}B_{16}Si_2$ (150h)	BCC(Main)	13	0.63	2.869(5)	1.7510^{16}
	FCC(Minor)	10	0.73	3.588(1)	0.9510^{16}
$Fe_{80}(NiZr)_8B_{12}$ (80h)	BCC	14	0.55	2.870(1)	0.4710^{16}
$Fe_{80}Nb_8B_{12}$ (80h)	BCC	11	0.48	2.876(1)	0.7210^{16}
$FeCoNiB_{0.5}Si_{0.5}$ (150h)	FCC	10	0.70	3.630(8)	0.9910^{16}
$Fe_{65}Ni_{28}Mn_7$ (130h)	BCC(Minor)	11	1.2	2.867(5)	0.61910^{16}
	FCC(Main)	10	0.9	3.591(2)	0.8010^{16}
FeCoMn (130h)	BCC	16	0.52	2.855(5)	0.35710^{16}

Table 8.1: Structural and microstructural properties of alloys produced by MA.

For $Fe_{80}(NiZr)_8B_{12}$, $Fe_{80}Nb_8B_{12}$, $FeCoNiB_{0.5}Si_{0.5}$ and FeCoMn, the milled result in each alloy was clearly a single-phase face centered cubic (FCC) or body centered cubic (BCC) solid solution, demonstrating that the various chemical elements entirely dissolve in Fe during high-energy ball milling. The two alloys $Fe_{70}Ni_{12}B_{16}Si_2$ and $Fe_{65}Ni_{28}Mn_7$ demonstrating a biphasic final alloy (BCC +FCC). Except for the FeCoMn alloy, all of the alloys had crystallite sizes less than 14 nm.

8.1.2 Magnetic Analysis

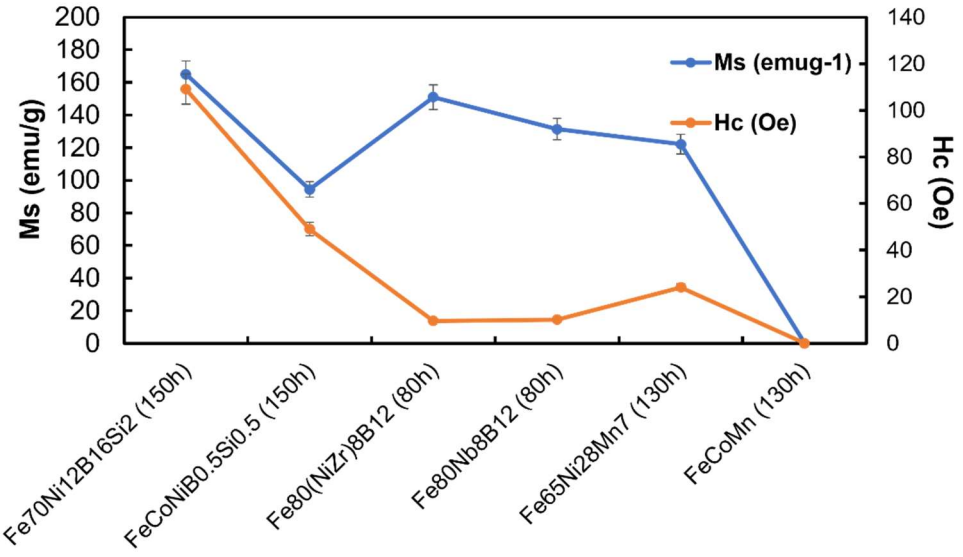

Figure 8.1: Magnetic saturation and Coercivity of alloys produced by MA.

All alloys after milling have a soft magnetic behavior/response, except of the $Fe_{70}Ni_{12}B_{16}Si_2$, FeCoNi(B,Si) and Fe65Ni28Mn7 wich exhibit semi-hard behavior. The $Fe_{70}Ni_{12}B_{16}Si_2$ alloy had the highest saturation magnetization (165 $emug^{-1}$) while the FeCoMn alloy had the lowest coercivity (2.410^{-4} Oe).

8.2 Arc Melting (AM)

8.2.1 Magnetic behaviors

Arc Melting	Structure	Relative density (%)	M_s ($emug^{-1}$)	H_c(Oe)	M_r/ M_s
$Fe_{65}Ni_{28}Mn_7$	FCC	96.23	18.81	2.26	0.0008
FeCoMn	HCP	100	1.01	124.28	0.033

Table 8.2: Relative densities and Magnetic characteristics of alloys produced by AM.

The structure of the $Fe_{65}Ni_{28}Mn_7$ alloy formed by Arc melting is an FCC, which is also the predominant phase structure found in the same alloy made by mechanical alloying.

whereas the structure of the FeCoMn is HCP, which is completely different from the structure of the same alloy produced through mechanical alloying. In comparison to the $Fe_{65}Ni_{28}Mn_7$ alloy, the FeCoMn formed by Arc melting is a totally dense material. The $Fe_{65}Ni_{28}Mn_7$ had the greater saturation magnetization and the lower coercivity as it is a soft magnetic sample. While FeCoMn formed by Arc melting is a semi-hard alloy.

8.2.2 Mechanical properties

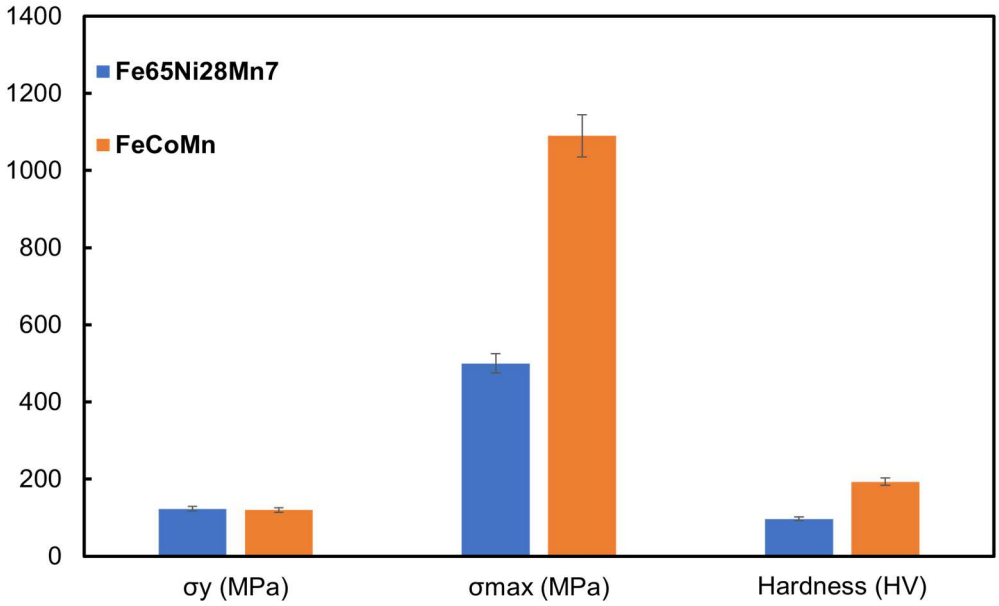

Figure 8.2: Mechanical properties of alloys produced by AM.

Yield strength was nearly the same for both alloys. It indicates the maximum amount of stress that may be developed in a material without generating plastic deformation. The maximal compressive strength (σ_{max}) and hardness (H_V) of the FeCoMn alloy are two times as great as those of the $Fe_{65}Ni_{28}Mn_7$ alloy.

8.3 Spark plasma sintering (MA)

8.3.1 Relative density

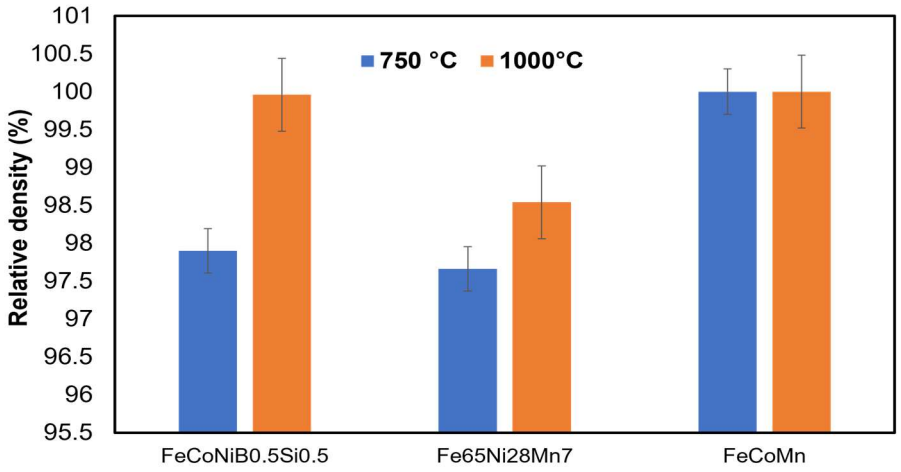

Figure 8.3: Relative densities of alloys produced by SPS at 750°C and 1000°C.

The relative density of the alloy produced by SPS at 750°C and 1000°C are shown in the picture. All alloys formed at 1000°C have a higher relative density than alloys made at 750°C. At both temperatures, the FeCoMn registers greater relative densities (Full density).

8.3.2 Magnetic Analysis

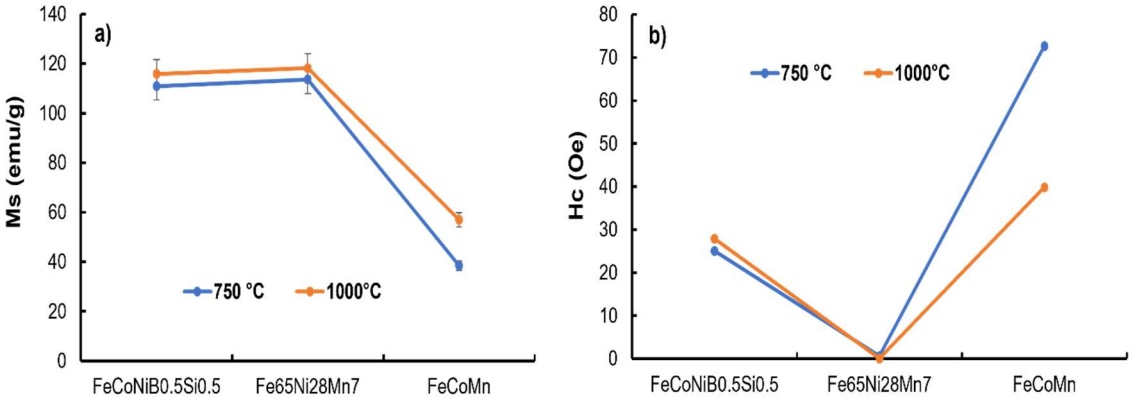

Figure 8.4: Magnetic behaviors of alloys produced by SPS, a) Saturation magnetization and b) Coercivity.

Figure 8.4 displays the saturation magnetization and coercivity of SPS alloys at 750°C and 1000°C. $Fe_{65}Ni_{28}Mn_7$ demonstrated grater saturation magnetization and lesser coercivity at both sintering temperatures. Thus, the $Fe_{65}Ni_{28}Mn_7$ represents the soft magnetic behavior at both sintered temperatures.

8.3.3 Mechanical properties

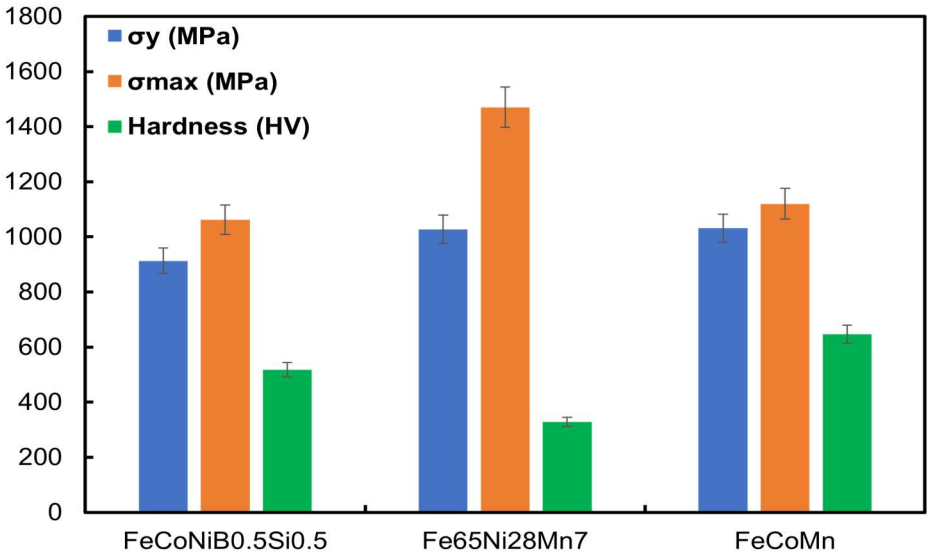

Figure 8.5: Mechanical properties of alloys produced by SPS at 750°C.

Figure 8.5 depicts the mechanical characteristics of $FeCoNiB_{0.5}Si_{0.5}$, $Fe_{65}Ni_{28}Mn_7$, and FeCoMn alloys sintered at 750°C. The yield strength (σ_y) of the three alloys is approximately identical. The compressive strength (σ_{max}) of $FeCoNiB_{0.5}Si_{0.5}$ and FeCoMn alloys is close (1062 and 1120MPa, respectively). The $Fe_{65}Ni_{28}Mn_7$ achieved a maximum value of around 1470 MPa. According to the Vickers hardness (H_V), the FeCoMn is harder than the $FeCoNiB_{0.5}Si_{0.5}$ and twice as hard as the $Fe_{65}Ni_{28}Mn_7$.

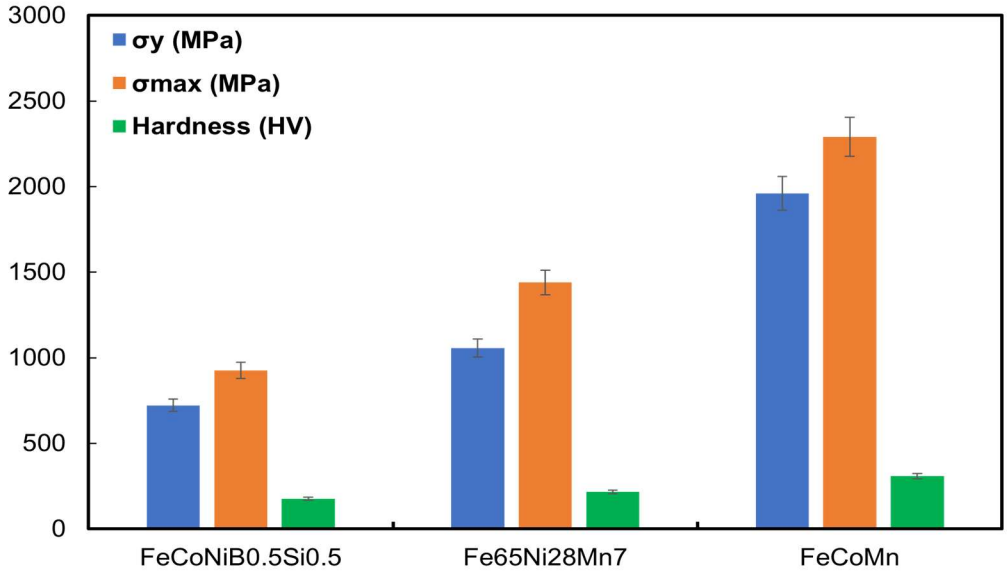

Figure 8.6: Mechanical properties of alloys produced by SPS at 1000°C.

All alloys lost hardness (H_V) when the sintering temperature was raised to 1000 °C. The yield (σ_y) and compression strength (σ_{max}) of $FeCoNiB_{0.5}Si_{0.5}$ have both reduced. The yield strength (σ_y) of the $Fe_{65}Ni_{28}Mn_7$ has increased by approximately 29MPa, whereas the compression strength (σ_{max}) has dropped by approximately 30MPa. In comparison to the other alloys, the yield strength (σ_y) and compression strength (σ_{max}) of the FeCoMn alloy were higher. The yield strength (σ_y) of the FeCoMn alloy is double that of the $Fe_{65}Ni_{28}Mn_7$ alloy.

8.3.4 Correlation of magnetic and mechanical properties after SPS

- $FeCoNiB_{0.5}Si_{0.5}$

By raising the sintering temperature from 750 °C to 1000 °C, coercivity increased slightly however mechanical properties (hardness (Hv) and yield strength (y) decreased. The alloy exhibits a semi-hard behavior with an FCC main structure at both temperatures.

- $Fe_{65}Ni_{28}Mn_7$

Certain correlations may be drawn between the impact of sintering temperature on coercivity and hardness. As with coercivity, hardness Hv decreases with increasing temperature, although yield strength rises. Following sintering, the two bulk samples exhibit soft magnetic behavior with the primary FCC structure.

- FeCoMn

An additional correlation was discovered between coercivity and hardness, as the sintering temperature increased. Coercivity and hardness reduced but yield strength rose. Both bulk samples of this alloy exhibit semi-hard behavior with a BCC main structure.

CHAPTER 9

Conclusions

This thesis' findings are organized into three sections that correlate to the procedure used to produce the iron-based alloy. The first section contains the results reached after the alloys were synthesized using only the Mechanical alloying technique. The second is concerned with the findings gained when mechanical alloying and spark plasma sintering were used to produce the HEA. The last part extracted the findings obtained from the two Fe-based alloys produced by mechanical alloying followed by spark plasma sintering and then produced by arc melting for comparison.

By Mechanical alloying process:

- Formation of biphasic MA Fe-Ni-Si-B alloy: The final powder of the $Fe_{70}Ni_{12}B_{16}Si_2$ milled for 150 hours was biphasic, with a main BCC phase and a minor FCC phase, and had a semi-hard characteristic. A hard magnetic characteristic is observed after annealing the final powder at 450 °C. Annealing at 650 °C, on the other hand, results in softening the final powder. The phase transformation during annealing has a considerable influence on the magnetic response.
- Different behavior in powdered and agglomerated MA samples: Mechanical alloying of $Fe_{80}NiZr_8B_{12}$ and $Fe_{80}Nb_8B_{12}$ produced the same primary BCC phase. The microstrain and dislocation densities of the agglomerated particles formed throughout the mechanical alloying of both alloys were higher than those of the powders. In terms of magnetic properties, both agglomerated and powder samples of both alloys exhibited soft magnetic behavior. We discovered that agglomerated particles have greater magnetic saturation and coercivity than powders. Regarding the thermal stability, the agglomerated particles outperformed the powder, except for the alloy $Fe_{80}Nb_8B_{12}$, where the powder exceeded the agglomerated particles due to the high Nb(B) content of the agglomerated particles.

By Mechanical alloying followed by spark plasma sintering:

- MA followed by SPS provides the best mechanical response at low temperatures (750°C) and the best magnetic behavior at high temperatures (1000°C): Mechanical alloying was employed to successfully produce the $FeCoNiB_{0.5}Si_{0.5}$ HEA alloy, and a single FCC solid solution with a grain size of approximately 10 nm was achieved. Annealing the final powder resulted in softer magnetic behavior, with saturation magnetization increasing from 94 $emug^{-1}$ to 127 $emug^{-1}$ and coercivity falling from 49 Oe to 29 Oe. This is due to the supersaturated FCC phase decomposing during annealing. After sintering the final powder by SPS at 750°C and 1000°C, two bulk samples were successfully made. Both bulk samples improve the magnetic properties of the final milled powder (reduced coercivity registered after 1000°C sintering), while the sample sintered at 750°C demonstrate the best mechanical behavior. (Vickers hardness equivalent to 518 HV and compressive strength close to 1062 MPa).

By Arc melting and Mechanical alloying followed by spark plasma sintering process:

- For comparison, a $Fe_{65}Ni_{28}Mn_7$ alloy was synthesized by mechanical alloying and consolidated by spark plasma sintering, and the same composition was created by arc melting.

  - Arc melting favors single phase formation, whereas mechanical alloying promotes biphasic formation: After 130 hours of milling, mechanical alloying produces two supersaturated solid solutions: a BCC phase with a crystallite size of 11 nm and a main FCC phase with a crystallite size of 10 nm. The creation of a single FCC phase results from arc melting process. Mechanical alloying followed by spark plasma sintering (MA+SPS) indicated the removal of the BCC phase in sintered alloys. The sintered alloys at 750 °C also showed an FCC phase with a crystallites size in the nanometer scale.

  - Magnetic behavior is influenced by the manufacturing process: The powder formed after MA had semi-hard magnetic behavior, the magnetic softness was achieved after Arc melting and SPS sintering. All sintered alloys exhibit soft magnetic behavior. The alloy sintered at 1000°C under 50 MPa displayed soft magnetic characteristics, with saturation magnetization (Ms) of 118.10 $emug^{-1}$ and

coercivity (Hc) of 0.07 Oe, naming it as a promising option for soft magnetic applications.

- The manufacturing method has an impact on the mechanical properties: The alloy sintered at 750 °C under 75 MPa displayed the best mechanical combination, with Vickers hardness, yield strength, and shortening values of 425HV, 1700MPa, and 16%, respectively. The alloy formed via AM has reduced hardness and yield strength values but good ductility with a strain to failure value of approximately 30%.

- A FeCoMn alloy was synthesized using mechanical alloying followed by spark plasma sintering for comparison with an identical alloy produced through arc melting (AM).

  - Arc melting favors a single phase forming: After 130 hours of milling, mechanical alloying yields a BCC Fe(Co,Mn) solid solution with a crystallite size of 11 nm and traces of Mn and MnO. Arc melting resulted in the formation of a single HCP-Co (Fe,Mn) phase. Mechanical alloying followed by spark plasma sintering at 750°C revealed the presence of the BCC, FCC and MnO phases. After sintering at 1000°C, the amount of FCC phase and MnO decreases.

  - Production process influences magnetic behavior: All sintered alloys, as well as the sample produced by Arc melting have a semi-hard magnetic behavior. The powder produced following MA, have soft magnetic behavior. Comparing the sintered alloys, the magnetic behavior was enhanced by increasing the sintered temperature to 1000°C which shows a saturation magnetization (Ms) of 56 $emug^{-1}$ and a coercivity (Hc) of 39 Oe.

  - The manufacturing procedure influences the mechanical features: The alloy sintered at 750 °C had the best Vickers hardness value of 647 HV, however, the sample sintered at 1000 °C had a greater shortening at failure value A% (greater than 22%), a higher compressive strength of 2290 MPa, and a higher yield strength of 1990 MPa. The alloy created through AM has low hardness and yield strength values but high ductility, with a strain to failure value greater than 30%.

Future perspectives

A range of potential opportunities is forthcoming to continue working in this field of advanced materials research.

1. Complete the sample analysis with a more in-depth thermal and magnetic characterization.
2. Sintering of samples of the three initial iron-based alloys. Investigate the processes involved. Once a low porosity bulk material has been obtained, examine its microstructure, thermal stability, magnetic characteristics, and mechanical properties.
3. Expanding the range of compositions produced, while adding other elements such as Ni or Cu for some alloys, trying to improve the magnetic response of Fe-based alloys.
4. Optimization of the SPS consolidation conditions to provide excellent magnetic behavior and mechanical performance.
5. Computer simulations might also be beneficial in predicting the microstructure and other properties of the milled and sintered samples, respectively.

BIBLIOGRAPHY

BIBLIOGRAPHY

[1] Holden, Norman E. History of the origin of the chemical elements and their discoverers. No. BNL-211891-2019-COPA. Brookhaven National Lab. (BNL), Upton, NY (United States), 2019.

[2] Domashenkov, Alexey, et al. "Microstructure and physical properties of a Ni/Fe-based superalloy processed by Selective Laser Melting." Additive Manufacturing 15 (2017): 66-77.

[3] Cladera, Antoni, et al. "Iron-based shape memory alloys for civil engineering structures: An overview." Construction and building materials 63 (2014): 281-293.

[4] Ding, J., et al. "High-coercivity ferrite magnets prepared by mechanical alloying." Journal of Alloys and Compounds 281.1 (1998): 32-36.

[5] He, Kai, et al. "Vortex formation during magnetization reversal of Co slotted nanorings." IEEE Transactions on Magnetics 45.10 (2009): 3885-3888.

[6] Jeż, Bartłomiej, et al. "The Process of Magnetizing FeNbYHfB Bulk Amorphous Alloys in Strong Magnetic Fields." Materials 13.6 (2020): 1367.

[7] Cullity, Bernard Dennis, and Chad D. Graham. Introduction to magnetic materials. John Wiley & Sons, 2011.

[8] Jiles, D. C. "Recent advances and future directions in magnetic materials." Acta materialia 51.19 (2003): 5907-5939.

[9] Yeh, J-W., et al. "Nanostructured high-entropy alloys with multiple principal elements: novel alloy design concepts and outcomes." Advanced engineering materials 6.5 (2004): 299-303.

[10] Cantor, Brain, et al. "Microstructural development in equiatomic multicomponent alloys." Materials Science and Engineering: A 375 (2004): 213-218.

[11] Zhang, Chuan, and Michael C. Gao. "CALPHAD modeling of high-entropy alloys." High-Entropy Alloys: Fundamentals and Applications (2016): 399-444.

[12] Jien-Wei, Y. E. H. "Recent progress in high entropy alloys." Ann. Chim. Sci. Mat 31.6 (2006): 633-648.

[13] Yeh, J-W., et al. "Nanostructured high-entropy alloys with multiple principal elements: novel alloy design concepts and outcomes." Advanced engineering materials 6.5 (2004): 299-303.

[14] Yeh, Jien-Wei. "Alloy design strategies and future trends in high-entropy alloys." Jom 65 (2013): 1759-1771.

[15] Wei, Ran, et al. "Formation of soft magnetic high entropy amorphous alloys composites containing in situ solid solution phase." Journal of Magnetism and Magnetic Materials 449 (2018): 63-67.

[16] Tong, Chung-Jin, et al. "Microstructure characterization of Al x CoCrCuFeNi high-entropy alloy system with multiprincipal elements." Metallurgical and Materials Transactions A 36 (2005): 881-893.

[17] Miracle, Daniel B., and Oleg N. Senkov. "A critical review of high entropy alloys and related concepts." Acta Materialia 122 (2017): 448-511.

[18] Zhang, Yong, et al. "High-entropy alloys with high saturation magnetization, electrical resistivity and malleability." Scientific reports 3.1 (2013): 1455.

[19] Fujieda, Tadashi, et al. "CoCrFeNiTi-based high-entropy alloy with superior tensile strength and corrosion resistance achieved by a combination of additive manufacturing using selective electron beam melting and solution treatment." Materials Letters 189 (2017): 148-151.

[20] Hsu, Chin-You, et al. "Effect of iron content on wear behavior of AlCoCrFexMo0. 5Ni high-entropy alloys." Wear 268.5-6 (2010): 653-659

[21] Huang, Can, et al. "Dry sliding wear behavior of laser clad TiVCrAlSi high entropy alloy coatings on Ti–6Al–4V substrate." Materials & Design 41 (2012): 338-343.

[22] Chuang, Ming-Hao, et al. "Microstructure and wear behavior of AlxCo1. 5CrFeNi1. 5Tiy high-entropy alloys." Acta Materialia 59.16 (2011): 6308-6317.

[23] Wu, Jien-Min, et al. "Adhesive wear behavior of AlxCoCrCuFeNi high-entropy alloys as a function of aluminum content." Wear 261.5-6 (2006): 513-519.

[24] Gludovatz, Bernd, et al. "A fracture-resistant high-entropy alloy for cryogenic applications." Science 345.6201 (2014): 1153-1158.

[25] Alaneme, Kenneth Kanayo, Michael Oluwatosin Bodunrin, and Samuel Ranti Oke. "Processing, alloy composition and phase transition effect on the mechanical and corrosion properties of high entropy alloys: a review." *Journal of Materials Research and Technology* 5.4 (2016): 384-393.

[26] Gorr, B., et al. "Phase equilibria, microstructure, and high temperature oxidation resistance of novel refractory high-entropy alloys." Journal of Alloys and Compounds 624 (2015): 270-278.

[27] B. Gorr, F. Mueller, H.J. Christ, T. Mueller, H. Chen, A. Kauffmann, M. Heilmaier, High temperature oxidation behavior of an equimolar refractory metal-based alloy 20Nb 20Mo 20Cr 20Ti 20Al with and without Si addition, Journal of Alloys and Compounds 688 (2016) 468-477

[28] Yao, Haili, et al. "High strength and ductility AlCrFeNiV high entropy alloy with hierarchically heterogeneous microstructure prepared by selective laser melting." Journal of Alloys and Compounds 813 (2020): 152196.

[29] Wu, Zhenggang, and Hongbin Bei. "Microstructures and mechanical properties of compositionally complex Co-free FeNiMnCr18 FCC solid solution alloy." *Materials Science and Engineering: A* 640 (2015): 217-224.

[30] Li, Jinshan, et al. "Enhanced mechanical properties of a CoCrFeNi high entropy alloy by supercooling method." Materials & Design 95 (2016): 183-187.

[31] Ng, Chun, et al. "Phase stability and tensile properties of Co-free Al0. 5CrCuFeNi2 high-entropy alloys." *Journal of alloys and compounds* 584 (2014): 530-537.

[32] Lei, Zhifeng, et al. "Enhanced strength and ductility in a high-entropy alloy via ordered oxygen complexes." Nature 563.7732 (2018): 546-550.

[33] Yang, T., et al. "Multicomponent intermetallic nanoparticles and superb mechanical behaviors of complex alloys." Science 362.6417 (2018): 933-937.]

[34] Xu, S. S., et al. "Mechanical properties and deformation mechanisms of a novel austenite-martensite dual phase steel." International Journal of Plasticity 128 (2020): 102677.

[35] Liu, L., et al. "Making ultrastrong steel tough by grain-boundary delamination." Science 368.6497 (2020): 1347-1352

[36] He, B. B., et al. "High dislocation density–induced large ductility in deformed and partitioned steels." *Science* 357.6355 (2017): 1029-1032.

[37] Guo, Sheng, et al. "Effect of valence electron concentration on stability of fcc or bcc phase in high entropy alloys." Journal of applied physics 109.10 (2011): 103505.

[38] Suryanarayana, Cury. "Mechanical alloying and milling." Progress in materials science 46.1-2 (2001): 1-184.

[39] Scudino, Sergio, et al. "Mechanical alloying and milling of Al–Mg alloys." Journal of Alloys and Compounds 483.1-2 (2009): 2-7.

[40] Zhang, D. L. "Processing of advanced materials using high-energy mechanical milling." Progress in Materials Science 49.3-4 (2004): 537-560.

[41] Calka, A., and A. P. Radlinski. "Universal high performance ball-milling device and its application for mechanical alloying." Materials Science and Engineering: A 134 (1991): 1350-1353.

[42] Benjamin, John S. "Dispersion strengthened superalloys by mechanical alloying." Metallurgical transactions 1 (1970): 2943-2951.

[43] El-Eskandarany, M. Sherif. Mechanical alloying: For fabrication of advanced engineering materials. William Andrew, 2001.

[44] Campbell, S. J., and W. A. Kaczmarek. "Mössbauer effect studies of materials prepared by mechanochemical methods." Mössbauer spectroscopy applied to magnetism and materials science (1996): 273-330.

[45] Maurice, David R., and T. H. Courtney. "The physics of mechanical alloying: a first report." Metallurgical Transactions A 21 (1990): 289-303.

[46] Tokita, Masao. "Progress of spark plasma sintering (SPS) method, systems, ceramics applications and industrialization." Ceramics 4.2 (2021): 160-198.

[47] Lenel, Fritz V. "Resistance sintering under pressure." Jom 7 (1955): 158-167.

[48] Inoue K 1966 US Patent No. 3,241,956

[49] https://www.fdc.co.jp/sps/aboutus/e_aboutus_milestone.html [Accessed: 24-Feb 2023].

[50] http://www.fct-systeme.de/ [Accessed: 24-Feb-2023].

[51] http://www.thermaltechnology.com/ [Accessed: 24-Feb-2023].

[52]https://www.haoyuefurnace.com/news/spark-plasma-sintering-sps-system.html [Accessed: 24-Feb-2023].

[53] Nygren, Mats, and Zhijian Shen. "On the preparation of bio-, nano-and structural ceramics and composites by spark plasma sintering." Solid state sciences 5.1 (2003): 125-131.

[54] Nygren, Mats, and Z. Shen. "Spark plasma sintering: possibilities and limitations." Key Engineering Materials. Vol. 264. Trans Tech Publications Ltd, 2004.

[55] Angerer, P., et al. "Spark-plasma-sintering (SPS) of nanostructured titanium carbonitride powders." Journal of the European Ceramic Society 25.11 (2005): 1919-1927.

[56] Zhan, Guo-Dong, et al. "A novel processing route to develop a dense nanocrystalline alumina matrix (< 100 nm) nanocomposite material." Journal of the American Ceramic Society 86.1 (2003): 200-2002.

[57] Anselmi-Tamburini, U., et al. "Fundamental investigations on the spark plasma sintering/synthesis process: II. Modeling of current and temperature distributions." Materials Science and Engineering: A 394.1-2 (2005): 139-148.

[58] Omori, Mamoru. "Sintering, consolidation, reaction and crystal growth by the spark plasma system (SPS)." Materials Science and Engineering: A 287.2 (2000): 183-188.

[59] Frage, Naum, et al. "Spark plasma sintering (SPS) of transparent magnesium-aluminate spinel." Journal of Materials Science 42 (2007): 3273-3275.

[60] Masao, T. O. K. I. T. A. "Trends in advanced SPS spark plasma sintering systems and technology." J. Soc. Powder Tech., Japan 30 (1993): 11.

[61] Chen, W., et al. "Fundamental investigations on the spark plasma sintering/synthesis process: I. Effect of dc pulsing on reactivity." Materials Science and Engineering: A 394.1-2 (2005): 132-138.

[62] Hulbert, Dustin M., et al. "The absence of plasma in “spark plasma sintering”." Journal of Applied Physics 104.3 (2008): 033305.

[63] Grasso, Salvatore, Yoshio Sakka, and Giovanni Maizza. "Electric current activated/assisted sintering (ECAS): a review of patents 1906–2008." Science and Technology of Advanced Materials 10.5 (2009): 053001.

[64] Serrano-Sánchez, Federico, et al. "Nanostructured state-of-the-art thermoelectric materials prepared by straight-forward arc-melting method." Thermoelectrics for Power Generation-A Look at Trends in the Technology (2016).

[65] Lutterotti, Luca, Siegfried Matthies, and Hans Rudlolf Wenk. "MAUD: a friendly Java program for material analysis using diffraction." IUCr: Newsletter of the CPD 21.14-15 (1999).

[66] Bragg, W. L., and J. J. Thomson. "Mr Bragg, Diffraction of Short Electromagnetic Waves, etc. 43." Proceedings of the Cambridge Philosophical Society: Mathematical and physical sciences. Vol. 17. Cambridge Philosophical Society, 1914.

[67] X-Ray Diffraction (XRD) | Open Energy Information.” [Online]. Available: http://en.openei.org/wiki/X-Ray_Diffraction_(XRD). [Accessed: 24-Feb-2023].

[68] Rietveld, H. M. "Line profiles of neutron powder-diffraction peaks for structure refinement." Acta Crystallographica 22.1 (1967): 151-152.

[69] Goodsell, David S. Bionanotechnology: lessons from nature. John Wiley & Sons, 2004.

[70] Petty, Michael C. Molecular electronics: from principles to practice. John Wiley & Sons, 2008.

[71] Zhou, Weilie, et al. "Fundamentals of scanning electron microscopy (SEM)." Scanning Microscopy for Nanotechnology: Techniques and Applications (2007): 1-40.

[72] Hodoroaba, Vasile-Dan. "Energy-dispersive X-ray spectroscopy (EDS)." Characterization of Nanoparticles. Elsevier, 2020. 397-417.

[73] Becker, Sabine. Inorganic mass spectrometry: principles and applications. John Wiley & Sons, 2008.

[74] Skoog, Douglas A., F. James Holler, and Stanley R. Crouch. Principles of instrumental analysis. Cengage learning, 2017.

[75] Wang, Huan-Rong, et al. "Crystallization kinetics of an amorphous Zr–Cu–Ni alloy: calculation of the activation energy." Journal of Alloys and Compounds 353.1-2 (2003): 200-206.

[76] https://nabis.fisi.polimi.it/equipments/vibrating-sample-magnetometer/ [Accessed: 05-Abril-2023]

[77] Rafique, Mohsin. Study of the Magnetoelectric Properties of Multiferroic Thin Films and Composites for Device Applications. Diss. COMSATS Institute of Information Technology Lahore Campus-Pakistan, 2015.

[78] Clarke, John, and Alex I. Braginski. The SQUID handbook. Vol. 1. Weinheim: Wiley-Vch, 2004.

[79] Josephson, B. D. "The discovery of tunnelling supercurrents Rev." (1974): 251.

[80] Buchner, M., et al. "Tutorial: Basic principles, limits of detection, and pitfalls of highly sensitive SQUID magnetometry for nanomagnetism and spintronics." Journal of Applied Physics 124.16 (2018): 161101.

[81] Sekri, Abderrahmène, et al. "Synthesis and structural characterization of nanocrystalline Fe-Ni-Zr-B alloy prepared by powder metallurgy." Journal of the Tunisian Chemical Society 17 (2015): 49-56.

[82] Gharsallah, H. Ibn, et al. "Magnetic and microstructural properties of nanocrystalline Fe-25 at% Al and Fe-25 at% Al+ 0.2 at% B alloys prepared by mechanical alloying process." The European Physical Journal Plus 4.131 (2016): 1-9.

[83] Abbasi, S., H. Eslamizadeh, and H. Raanaei. "Study of synthesis, structural and magnetic properties of nanostructured (Fe67 Ni33) 70 Ti10 B20 alloy." Journal of Magnetism and Magnetic Materials 451 (2018): 780-786.

[84] Raanaei, Hossein, Hossein Eskandari, and Vahid Mohammad-Hosseini. "Structural and magnetic properties of nanocrystalline Fe–Co–Ni alloy processed by mechanical alloying." Journal of Magnetism and Magnetic Materials 398 (2016): 190-195.

[85] Luo, Hongzhi, et al. "FCC Fe2NiSi prepared by mechanical alloying and stabilization effect of L21B disorder on BCC Heusler structure." Journal of Magnetism and Magnetic Materials 419 (2016): 485-489.

[86] Rahm, Martin, Roald Hoffmann, and N. W. Ashcroft. "Atomic and ionic radii of elements 1–96." Chemistry–A European Journal 22.41 (2016): 14625-14632.

[87] Tebib, W., et al. "Structural characterization of nanostructured Fe-8P powder mixture." Journal of Nanoscience and Nanotechnology 8.4 (2008): 2029-2036.

[88] Mhadhbi, M., et al. "Characterization of mechanically alloyed nanocrystalline Fe (Al) crystallite size and dislocation density." Journal of Nanomaterials 2010 (2010): 1-8.

[89] Kalita, M. P. C., A. Perumal, and A. Srinivasan. "Structure and magnetic properties of nanocrystalline Fe75Si25 powders prepared by mechanical alloying." Journal of Magnetism and Magnetic Materials 320.21 (2008): 2780-2783.

[90] Karimi, L., et al. "Improvement of magnetic properties of nanostructured Ni79Fe16Mo5 alloyed powders by a suitable heat treatment." Advanced Powder Technology 24.3 (2013): 653-658.

[91] Amini, R., et al. "Microstructural, thermal and magnetic properties of amorphous/nanocrystalline FeCrMnN alloys prepared by mechanical alloying and subsequent heat treatment." Journal of alloys and compounds 480.2 (2009): 617-624.

[92] Yuting, Dong, and Ma Guofeng. "Research progress of Fe-based amorphous/nanocrystalline alloys." IOP Conference Series: Earth and Environmental Science. Vol. 565. No. 1. IOP Publishing, 2020

[93] Yapici, Guney Guven. "Simultaneous improvement in strength and ductility of severely deformed niobium alloy." Materials Letters 279 (2020): 128443.

[94] Cotai, Ana, et al. "A Comparative Study of Nanocrystalline Fe 38.5 Co 38.5 Nb 7 P 15Cu 1 Alloys Obtained by Mechanical Alloying and Rapid Quenching." Archives of Metallurgy and Materials (2022): 555-561.

[95] Conde Amiano, Alejandro, et al. "The use of amorphous boron powder enhances mechanical alloying in soft magnetic FeNbB alloy: A magnetic study." Journal of Applied Physics, 113 (17A330), 1-3 (2013).

[96] Silveyra, Josefina M., et al. "Soft magnetic materials for a sustainable and electrified world." Science 362.6413 (2018): eaao0195.

[97] Sun, Y., W. Yu, and Z. Hua. "Effect of the Thermal Treatment on the Microstructure and Magnetic Property of Fe_68Zr_20B_12 Alloy Prepared by Mechanical Alloying." Acta Physica Polonica A 119.3 (2011): 374-377.

[98] Ul'yanov, A. L., et al. "Structural and phase transformations during heat treatment of the Fe (71.4) Si (14.3) C (14.3) amorphous alloy prepared by mechanical alloying." The Physics of Metals and Metallography 110 (2010): 542-552.

[99] Carrillo, Albert, et al. "Structural, thermal and magnetic analysis of Fe75Co10Nb6B9 and Fe65Co20Nb6B9 nanostructured alloys." Materials 14.16 (2021): 4542.

[100] Huang, J. Y., et al. "Allotropic transformation of cobalt induced by ball milling." Nanostructured Materials 6.5-8 (1995): 723-726.

[101] Cardellini, F., and G. Mazzone. "Thermal and structural study of the hcp-to-fcc transformation in cobalt." Philosophical Magazine A 67.6 (1993): 1289-1300.

[102] Alleg, S., et al. "Magnetic and structural studies of mechanically alloyed (Fe50Co50) 62Nb8B30 powder mixtures." Journal of alloys and compounds 482.1-2 (2009): 86-89.

[103] Gharsallah, H. Ibn, et al. "The magnetic and structural properties of nanostructured (Fe75Al25) 100-xBx alloys prepared by mechanical alloying." Journal of Alloys and Compounds 729 (2017): 776-786.

[104] Sharifati, A., and S. Sharafi. "Structural and magnetic properties of nanostructured (Fe70Co30) 100− xCux alloy prepared by high energy ball milling." Materials & Design 41 (2012): 8-15.

[105] Louidi, S., et al. "Formation study of the ball-milled Cr20Co80 alloy." Journal of alloys and compounds 493.1-2 (2010): 110-115.

[106] Zerniz, N., et al. "Magnetic and structural properties of nanostructured Fe–20Al–2Cr powder mixtures." Materials Characterization 100 (2015): 21-30.

[107] Zhang, Q., et al. "The effects of phase constitution on magnetic and mechanical properties of FeCoNi (CuAl) x (x= 0–1.2) high-entropy alloys." Journal of Alloys and Compounds 693 (2017): 1061-1067.

[108] Huang, Shuo, et al. "Mechanism of magnetic transition in FeCrCoNi-based high entropy alloys." Materials & design 103 (2016): 71-74.

[109] Mishra, Rajesh K., and Rohit R. Shahi. "Phase evolution and magnetic characteristics of TiFeNiCr and TiFeNiCrM (M= Mn, Co) high entropy alloys." Journal of Magnetism and Magnetic Materials 442 (2017): 218-223.

[110] Fadeeva, V. I., et al. "Structural defects and thermal stability of Ti (Al) solid solution obtained by mechanical alloying." Materials Science and Engineering: A 242.1-2 (1998): 230-234.

[111] Fu, Zhiqiang, et al. "Microstructure and strengthening mechanisms in an FCC structured single-phase nanocrystalline Co25Ni25Fe25Al7. 5Cu17. 5 high-entropy alloy." Acta Materialia 107 (2016): 59-71.

[112] Canakci, A. Y. K. U. T., et al. "Effects of a new pre-milling coating process on the formation and properties of an Fe–Al intermetallic coating." Powder technology 268 (2014): 110-117.

[113] Zhang, Xue-Song, et al. "Mass production of chemicals from biomass-derived oil by directly atmospheric distillation coupled with co-pyrolysis." Scientific Reports 3.1 (2013): 1-7.

[114] Nie, Xiaowu, Mingqiang Sheng, and Awei Mabi. "Effect of SPS Sintering Process on Compressive Strength and Magnetic Properties of CoCuFeMnNi Bulk Alloy." JOM 74.7 (2022): 2665-2675.

[115] Jaafar, Mira, et al. "Highly creep-resistant alumina–SiC nanocomposites processed by spark plasma sintering." Scripta Materialia 68.2 (2013): 134-137.

[116] Oungkulsolmongkol, Theeranee, Pantip Salee-Art, and Wantanee Buggakupta. "Hardness and fracture toughness of alumina-based particulate composites with zirconia and strontia additives." Journal of Metals, Materials and Minerals 20.2 (2010).

[117] Nabbouh, Mayssam Hussein, et al. "Processing and properties of Ni dispersed zirconia toughened alumina." J. Ceram. Process. Res 18.9 (2017): 621-627.

[118] Wang, Zhangwei, et al. "The effect of carbon on the microstructures, mechanical properties, and deformation mechanisms of thermo-mechanically treated Fe40. 4Ni11. 3Mn34. 8Al7. 5Cr6 high entropy alloys." Acta Materialia 126 (2017): 346-360.

[119] Liu, Wei, et al. "High performance DLC/BP and ZnS/YbF3 double-layer protective and antireflective coatings." Journal of alloys and compounds 581 (2013): 526-529.

[120] Liu, Y. J., and I. T. H. Chang. "The correlation of microstructural development and thermal stability of mechanically alloyed multicomponent Fe-Co-Ni-Zr-B alloys." Acta materialia 50.10 (2002): 2747-2760.

[121] Takeuchi, Akira, and Akihisa Inoue. "Classification of bulk metallic glasses by atomic size difference, heat of mixing and period of constituent elements and its application to characterization of the main alloying element." Materials transactions 46.12 (2005): 2817-2829.

[122] Chermahini, M. Delshad, et al. "The effect of milling time and composition on microstructural and magnetic properties of nanostructured Fe–Co alloys." Journal of Alloys and Compounds 477.1-2 (2009): 45-50.

[123] Herzer, G. "Grain size dependence of coercivity and permeability in nanocrystalline ferromagnets." IEEE Transactions on magnetics 26.5 (1990): 1397-1402.

[124] Liu, Cong, et al. "Composition and phase structure dependence of mechanical and magnetic properties for AlCoCuFeNix high entropy alloys." Journal of Materials Science & Technology 35.6 (2019): 1175-1183.

[125] Zhang, K. B., et al. "Annealing on the structure and properties evolution of the CoCrFeNiCuAl high-entropy alloy." Journal of Alloys and Compounds 502.2 (2010): 295-299.

[126] Wu, Chen, et al. "Interplay of crystallization, stress relaxation and magnetic properties for FeCuNbSiB soft magnetic composites." Journal of Alloys and Compounds 673 (2016): 278-282.

[127] Geng, Kaijie, et al. "Fe-Si/ZrO2 composites with core-shell structure and excellent magnetic properties prepared by mechanical milling and spark plasma sintering." Journal of Alloys and Compounds 718 (2017): 53-62.

[128] Wang, Zhangwei, et al. "The effect of carbon on the microstructures, mechanical properties, and deformation mechanisms of thermo-mechanically treated Fe40. 4Ni11. 3Mn34. 8Al7. 5Cr6 high entropy alloys." Acta Materialia 126 (2017): 346-360.